ISTANBUL TECHNICAL UNIVERSITY ★ GRADUATE SCHOOL

COMPUTATIONAL AERODYNAMIC ANALYSIS OF FLOW AROUND APOLLO REENTRY CAPSULE WITH ANISOTROPIC MESH ADAPTATION

M.Sc. THESIS

Badamasi BABAJI

Department of Aeronautical and Astronautical Engineering

Aeronautical and Astronautical Engineering Program

JULY 2021

ISTANBUL TECHNICAL UNIVERSITY ★ GRADUATE SCHOOL

COMPUTATIONAL AERODYNAMIC ANALYSIS OF FLOW AROUND APOLLO REENTRY CAPSULE WITH ANISOTROPIC MESH ADAPTATION

M.Sc. THESIS

Badamasi BABAJI
(511181108)

Department of Aeronautical and Astronautical Engineering

Aeronautical and Astronautical Engineering Program

Thesis Advisor: Prof. Dr. Mehmet ŞAHİN

JULY 2021

ISTANBUL TEKNİK ÜNİVERSİTESİ ★ LİSANSÜSTÜ EĞİTİM ENSTİTÜSÜ

ANISOTROPİK MESH ADAPTASYONU İLE APOLLO YENİDEN GİRİŞ KAPSÜL ÇEVRESİNDEKİ AKIŞIN HESAPLAMALI AERODİNAMİK ANALİZİ

YÜKSEK LİSANS TEZİ

Badamasi BABAJI
(511181108)

Uçak ve Uzay Mühendisliği Anabilim Dalı

Uçak ve Uzay Mühendisliği Programı

Tez Danışmanı: Prof. Dr. Mehmet ŞAHİN

TEMMUZ 2021

Badamasi Babaji, a M.Sc. student of İTU Graduate School student ID 511181108, successfully defended the thesis entitled “COMPUTATIONAL AERODYNAMIC ANALYSIS OF FLOW AROUND APOLLO REENTRY CAPSULE WITH ANISOTROPIC MESH ADAPTATION”, which he prepared after fulfilling the requirements specified in the associated legislations, before the jury whose signatures are below.

Thesis Advisor : **Prof. Dr. Mehmet ŞAHİN** ....
İstanbul Technical University

Jury Members : **Assoc. Prof. Dr. Bayram ÇELİK** ....
Istanbul Technical University

Prof. Dr. Sinan EYİ ....
Middle East Technical University

Date of Submission : 16 June 2021
Date of Defense : 10 July 2021

To my family,

FOREWORD

I would like to begin by expressing my deepest gratitude and appreciation to my thesis advisor in person of **Prof. Dr. Mehmet ŞAHİN** for his opportune contributions, guidance and words of advice towards the successful completion of this master's thesis. His timely advices and scientific approach have helped me to a great extent to accomplish this millstone in my academic journey. I would also like to extend my appreciation to all the student and staff members of our computational laboratory, ITU HEMLAB for their kind support and words of encouragement.

Furthermore, I would like to acknowledge the computational resources provided by the National Center for High Performance Computing of Turkey (UheM). The Stanford University Aero lab for their Open-source CFD suite SU2 which was used immensely in this project and the GAMMA team at Inria for their PyAMG mesh adaptation software. Finally, to my father, Baba Abubakar Babaji, my mother Halima Badamasi, brother Nafiu Abubakar Babaji and my fiancé, Aisha T Yusuf for their boundless and continues support both financially and emotionally.

July 2021

Badamasi BABAJI
Aeronautical Engineer

TABLE OF CONTENTS

Page

ABBREVIATIONS

2-D **:** Two-dimensional
3-D **:** Three-dimensional
NASA **:** National Aeronautics and Space Administration
CESE **:** The Space–Time Conservation Element And Solution Element
CFL **:** Courant–Friedrichs–Lewy

SYMBOLS

$\mathbf{Q}$: Conservative variables vector

$\mathbf{W}$: Primitive variables vector

$\mathbf{U}$: Velocity vector

u,v,w : Velocity components

Re : Reynolds Number

P_r : Prandtl Number

μ : Dynamic Viscosity

ρ : Density

T : Temperature

$\mathbf{F_i}$: Inviscid Flux

$\mathbf{F_v}$: Viscous Flux

τ : Shear stress tensor

$\mathbf{n}$: Surface normal

nx, ny, nz : Shell internal stresses

α : Angle of attack

γ : Specific heat ratio

LIST OF TABLES

Page

LIST OF FIGURES

COMPUTATIONAL AERODYNAMIC ANALYSIS OF FLOW AROUND APOLLO REENTRY CAPSULE WITH ANISOTROPIC MESH ADAPTATION

SUMMARY

Atmospheric reentry is the movement of space vehicle from the cold environment of outer space into the atmospheric envelope of a planet. During the reentry phase, earth atmosphere represents a relatively dense fluid medium and a reentry vehicle has to follow a very narrow re-entry corridor in order to have a safe landing. If the vehicle strays above the corridor, it may skip out and back to the cold space environment. If it strays below the corridor, it may burn up and/or experience excessive g-force. The Astronauts most attempt to enter the atmosphere at a precise angle and speed in order to avoid fatal accident. Reentry capsules are designed with a blunt body to survive the extreme aerodynamic conditions. Understanding the flow field around the capsule is very important to engineer and designers for the design of such vehicles. Recently, astronomical missions are gaining global importance and recognition as mankind continues its mission of moving to outer space. The results from the numerical and experimental analysis are vital in designing the thermal protections system (TPS), including material selection and integration which considerably affect the total mass of the reentry capsule. While wind tunnel is generally considered as the undisputed tool for obtaining the necessary aerodynamic data to predict the performance and the motion path of the spacecraft, it is highly expensive and utilizing computational fluid dynamics in simulating reentry conditions would provide economical supplement, if the results are validated to be reliable. During the Apollo program (1963-1972), a large sum of money was spent in analyzing the flow characteristics around a reentry capsule at different possible conditions including supersonic, hypersonic, low-density, and shock tunnel testing facilities.

Apollo AS-202 first successful flight was recorded on 25th August 1966. It was the first space flight to include navigation and guidance system. It was the success of the AS-202 mission that allowed the continuation Apollo program which resulted to the first manned Saturn IB and the Block I space vehicle orbital flight, AS-204. The Apollo CM capsule reentered the atmosphere at an approximate speed of 8,690 m/s. The inclusion of the inertial measurement unit and pressure transducers enabled the reconstruction flight trajectory point and computation of the aerodynamic lift and drag force and coefficient of pitching moment around the center of gravity.

The free flight recorded data indicated some anomalies of the aerodynamic efficiency in comparison to the preflight wind tunnel analysis of the Apollo AS-202 capsule. To resolve these anomalies, several experiments were carried in wind tunnel by ARO inc, under a contract by Arnold Engineering Development Center (AEDC). The goal of these experiment was to reconcile these multiple anomalies and harmonized the aerodynamic data of the postflight analysis and flight (AS-202) recorded data. Attention was particular given in simulating the capsule as flown and obtaining consistent pitch plane force measurement in the angle of attack range 150 to 180 degrees.

The central goal of this thesis is to use computational fluid dynamics to re-simulate some of these experimental efforts in obtaining the aerodynamic data of AS-202

command module, and thus demonstrating the capability of CFD as a research tool for future analysis and design of space vehicles.

An open-source computational fluid dynamic solver, is used in this thesis for the analysis of flow around the Apollo AS-202 reentry capsule. SU2 is multi-physics CFD solver developed mainly for aerospace application in design, analysis and optimization of engineering problems primarily on unstructured computational domain. The main area of applications of this software are non-reacting aerospace computational fluid dynamics, two dimensional and 3D dimensional aerodynamic shape optimization. It is developed and maintained centrally by the Aerospace Design Lab (ADL) at Stanford University.

Reynold's Averaged Navier Stokes Equations (RANS) is solved around the Apollo AS-202 reentry capsule with Spalart Allmaras one-equation turbulence model which is based on linear eddy viscosity with the Boussinesq assumption for a constitutive relation. Ideal gas is used for all simulation as the fluid model and all simulation are normalized based on freestream velocity equals to Mach number and the freestream temperature equals one. Green-Gauss method is the numerical method used for the computation of spatial gradients. The Green-Gauss method is found to be more stable and thus is used largely than the weighted least square. A constant CFL number of one is used for all simulation due to the fine resolution of the mesh at the capsule boundary layer region. FGMRES is the linear solver used for implicit formulation with ILU preconditioner. For the convective numerical computation of the flow; Roe, AUSM, HLLC methods were all tested. The AUSM method is found to give good results however it is unstable compared to the ROE method. MUSCL method is used for the flux splitting of the second-order upwind schemes with a Venkatakrishnan slope limiter and Euler implicit is used for time discretization. The convergence criteria for all simulations is based on the residual of the continuity equation.

The computational domain (mesh) used for all simulations in this thesis is purely unstructured triangular element in 2-D and tetrahedrons in 3-D. To improve the accuracy of the simulation the solver is coupled with an open-source solution-based anisotropic mesh adaptation software (pyAMG) developed by the GAMMA team at French national institute for research in computer science and Automation (Inria).

In order to validate the solver's capability in obtaining accurate results for a hypersonic flow, Euler equations were solved for a flow at Mach 6 over a cylinder. These results are compared with a benchmark obtained using shock fitting code, which is a well-known baseline for the validation of accurate shock location in hypersonic flow. The result was also compared with that of space-time conservation element solution element (CESE). An excellent agreement between shock fitting, CESE and inviscid Euler equations (present) was obtained in accurately predicting the hypersonic flow field around a blunt body.

Furthermore, the flow condition of the of the Apollo wind tunnel experiments in tunnels A, B, C and L were re-simulated computationally to demonstrate the capability of CFD as a research tool for reentry analysis. The aerodynamic forces were analyzed in terms of lift-to-drag ration (Cl/Cd) through a wide range of attack from 150 to 180 degrees. The analysis shows good agreement between the experimental data and present CFD analysis. Further analysis was done to study the local flow separation and re-attachment. Experiment have shown there is a local flow separation and reattachment on the afterbody near the windward meridian at some selected angles of attacks. The results of the simulations in present study have demonstrated the same

phenomenon. Finally, convergence study is carried out to understand the effect of the solution-based anisotropic mesh adaptation on solution accuracy.

ANISOTROPİK MESH ADAPTASYONU İLE APOLLO YENİDEN GİRİŞ KAPSÜL ÇEVRESİNDEKİ AKIŞIN HESAPLAMALI AERODİNAMİK ANALİZİ

ÖZET

Atmosfere yeniden giriş, uzay aracının dış uzayın soğuk ortamından bir gezegenin atmosferine doğru hareketidir. Gezegen atmosferi uzaya kıyasla daha yoğun bir ortamdan meydana geldiğinden uzay aracı güvenli bir iniş yapabilmek için giriş esnasında daha dar bir dönüş koridoru (re-entry corridor) izlemek zorundadır. Eğer uzay aracı dönüş koridorunun irtifasından daha daha yükseğe saparsa yeniden uzay ortamına itilme tehlikesiyle karşı karşıya kalabilir. Diğer taraftan, dönüş koridorundan daha alçak bir irtifaya yöneliş gerçekleştirirse uzay aracı aşırı ısınmalara ve yüksek g-kuvvetlerine maruz kalabilir. Astronotlar ölümcül kazalardan kaçınmak için çoğu kez atmosfere doğru açılı bir hızla girmeye çalışırlar. Atmosfere yeniden giriş kapsülleri, kötü aerodinamik koşullardan kaçınmak amacıyla küt bir burundan oluşan bir gövdeyle tasarlanmıştır. Kapsülün etrafındaki akış alanını anlamak, bu tür bir kapsülün tasarımı için mühendis ve tasarımcılar için son derece önemlidir. Günümüzde, astronomik görevler, insanlığın uzaya gitme misyonu devam ettikçe küresel bir önem kazanmıştır. Sayısal ve deneysel analizlerden elde edilen sonuçlar, yeniden giriş kapsülünün toplam kütlesini önemli ölçüde etkileyen malzeme seçimi ve entegrasyonu dahil olmak üzere termal koruma sisteminin (TPS) tasarımında hayati öneme sahiptirler. Rüzgâr tünelleri genellikle bir uzay aracının performansını ve hareketini tahmin etmek için gerekli aerodinamik verileri elde etmek için tartışmasız bir araç olarak kabul edilse de, bu tünelleri çalıştırmak oldukça yüksek maliyetler içermektedir Bu yüzden, sonuçlar doğrulandığı takdirde, hesaplamalı akışkanlar dinamiği. Simülasyonları atmosfere yeniden giriş yapan uzay araçlarının tasarımında çok daha ekonomik bir çözüm sağlamaktadırlar. Apollo programı sırasında (1963-1972), süpersonik, hipersonik, düşük yoğunluklu ve şok tüneli test tesislerinde giriş kapsülünün etrafındaki akıştan veriler elde edebilmek için çok yüksek maliyetli testler yapılmıştır. Apollo AS-202'nin ilk başarılı uçuşu 25 Ağustos 1966'da kaydedildi. Bu navigasyon ve yönlendirme sistemini içeren ilk uzay uçuşuydu. İlk insanlı Satürn IB ve Blok I uzay aracı yörünge uçuşu AS-204 ile sonuçlanan Apollo programının devamına izin veren AS-202 misyonunun başarısıydı. Apollo CM kapsülü, atmosfere yaklaşık 8,690 m/s'lik bir hızla yeniden girdi. Atalet ölçüm biriminin ve basınç transdüserlerinin dahil edilmesi, uçuş yörünge noktasının yeniden yapılandırılmasına, aerodinamik taşıma, sürükleme kuvvetlerinin ve ağırlık merkezi etrafındaki yunuslama momenti katsayısının hesaplanmasına olanak sağlamıştır.

Serbest uçuşla kaydedilen veriler, apollo AS-202 kapsülünün ön kontrol analizine kıyasla aerodinamik verimlilik açısından bazı anormalliklere işaret etti. Bu anormalliklerin üstesinden gelebilmek adına, Arnold Engineering Development Center (AEDC) tarafından yapılan bir sözleşme kapsamında ARO INC. tarafından rüzgar tüneli testleri gerçekleştirilmiştir. Bu deneylerin amacı, bu anormallikleri çözmek ve uçuş sonrası analiz ile uçuşta (AS-202) kaydedilen verilerin uyumlu hale getirilmesiydi. Bu deneyler kapsamında, kapsülün uçarken simüle edilmesine ve 150 ila 180 derece hücum açısı aralığında yunuslama düzleminde kuvvet ölçümünün yapılabilmesine özellikle dikkat edildi.

Bu tezin temel amacı, AS-202 komut modülünün aerodinamik verilerini hesaplamalı akışkanlar dinamiği yöntemiyle doğrulayabilmek ve gelecekteki benzer çalışmalarda da hesaplamalı akışkanlar dinamiği yönteminin kabiliyetini göstermektir. Bu tezde, AS-202 modülü etrafındaki akışın analizi için açık kaynaklı bir hesaplamalı akışkanlar dinamiği çözücüsü, SU2 kullanılmıştır. SU2 temel olarak yapısal olmayan hesaplama alanındaki mühendislik problemlerinin tasarımı, analizi ve optimizasyonunda havacılık ve uzay uygulamaları için geliştirilmiş bir multi-physics CFD çözücüsüdür. Bu yazılımın ana uygulama alanı, hava-uzay problemlerinde karşılaşılan reaksiyonsuz akışlar, iki boyutlu ve 3 boyutlu boyutlu aerodinamik şekil optimizasyonudur. SU2 çözücüsü Stanford Üniversitesi'ndeki Havacılık ve Uzay Tasarım Laboratuvarı (ADL) tarafından geliştirilmiştir.

Reynolds Ortalamalı Navier Stokes Denklemleri (RANS), Boussinesq varsayımyla lineer viskozitesine dayanan Spalart Allmaras tek denklemli türbülans modeli ile AS-202 etrafında çözülmüştür. Akışkan modeli olarak tüm simülasyonlar için ideal gaz kullanılmıştır ve tüm simülasyonlar serbest akış hızının Mach sayısına ve serbest akış sıcaklığının bire eşit olması temelinde normalize edilmiştir. Ağırlıklı Green-Gauss yöntemleri, uzaysal gradyanların hesaplanmasında kullanılan sayısal yöntemlerdir. Green-Gauss yönteminin daha kararlı olduğu bulunmuştur ve bu nedenle ağırlıklı olarak en küçük kareler yönteminden daha çok kullanılmaktadır. Kapsül sınır tabakası bölgesindeki ağın ince çözünürlüğü nedeniyle tüm simülasyonlar için sabit bir CFL sayısı kullanılmıştır. FGMRES, ILU ön koşullandırıcılı kapalı formülasyon için kullanılan doğrusal çözücüdür. Akışın konvektif sayısal hesabı için; Roe, AUSM, HLLC yöntemlerinin tümü test edilmiştir. AUSM yönteminin daha doğru sonuçlar verdiği ancak ROE yöntemine göre çok kararsız olduğu bulunmuştur. Akıların ayrıklaştırılması için ikinci dereceden MUSCL şeması Venkatakrishnan eğim sınırlayıcısı ile birlikte kullanılmıştır. Zaman ayrıklaştırması için Euler implicit kullanılmıştır. Tüm simülasyonlar için yakınsama kriteri, süreklilik denkleminin kalıntısına dayanmaktadır.

Hem standart Navier-Stokes denkleminin hem de Reynolds Ortalamalı Navier Stokes denkleminin (RANS) uzaysal ayrıklaştırılması için SU2 ortamında sonlu hacimler yöntemi kullanılmıştır. Çözücü, verileri çift bölmeye dayalı uç tabanlı veri yapısıyla etki alanının köşelerinde depolar. Belirli bir kenarın orta noktası, viskoz ve konvektif akıların değerlendirildiği konumdur. Köşe tabanlı ve hücre merkezli ayrıklaştırma şemaları arasındaki temel fark şu şekilde özetlenebilir; Tüm akış değişkenleri, öncelikle köşe tabanlı şemalarda hesaplama alanının köşelerinde depolanır. Bu, şablon denkleminin en yakın komşuların düğüm bilgileri cinsinden olmasını sağlar. Diğer yandan, tüm akış ilkel değişkenleri, hesaplama alanındaki elemanların hücre merkezinde depolanır. Bu teknikte ayrıklaştırma şablonu genellikle komşuların eleman bilgilerinin kullanılmasını içerir. Köşe tabanlı ve hücre merkezli bu iki ayrıklaştırma yöntemi, aynı hesaplama alanına uygulanır, hem 2-D hem de 3-D'de basit olmayan elemanlar için büyük ölçüde özdeş olmayan bir ayrıklaştırma ile sonuçlanır.

Bu tezdeki tüm simülasyonlar için kullanılan hesaplama ağı, 2B'de tamamen yapısal olmayan üçgen elemanlar ve 3B'de dörtyüzlülerden meydana gelmektedir. Yapısal olmayan hücreler, değişken elemanların şekline izin vermedeki esneklikleri ve hesaplama alanını yaklaşık olarak tahmin etmek için düzensiz yerleştirilmiş noktalar nedeniyle yaygın olarak kullanılmaktadır. Yapısal olmayan hücreler, çoğunlukla 2-B'de üçgen ve 3-B'de dört yüzlü elemanlar olarak kullanır, ancak bazen dörtlü, altıgen ve prizma gibi diğer elemanların bir kombinasyonunu da içerebilir. Yapısal olmayan hücreler, karmaşık bir hesaplama ağının oluşturulmasında büyük bir esneklik sağlamanın yanı sıra hücre uyarlamalarına da olanak tanır. Başlangıçta noktalar düzensiz yerleştirildiğinden, çözüm tabanlı uyarlamalar ile noktaların silinmesine, eklenmesine veya taşınmasına izin verir. Çözüm doğruluğunu artırmak için yerel bağlantı matrisi güncellenir. Hücre uyarlamalarının ana amacı, belirli bir sayısal simülasyonda hatanın minimum değerini üretecek bir hesaplamalı sistemde optimal nokta dağılımını elde etmektir. Simülasyonun doğruluğunu artırmak için çözücü, Fransız ulusal bilgisayar bilimi ve Otomasyon araştırma enstitüsünde (Inria) GAMMA ekibi tarafından geliştirilen açık kaynaklı gradyan tabanlı anizotropik hücre uyarlama yazılımı (pyAMG) ile birleştirilmiştir.

Çözücünün hipersonik bir akış için doğru sonuçlar elde etme yeteneğini doğrulamak için, bir silindir üzerinde Mach 6 akışı için Euler denklemleri çözülmüştür. Çözücüden elde edilen sonuçlar hipersonik akışlarda şok konumunu şok uydurma yöntemi ile tahmin eden bir çözücü ile karşılaştırılmıştır. Şok uydurmada Euler denklemi, cismin önünde fakat şok dalgasının arkasında olan hesaplama bölgesinde şok uydurma yaklaşımı ile çözülür. Bu tekniğin amacı, sayısal kararsızlık ve doğruluk bağımlılığı ile ilgili problemlerin, şok dalgasının kesin konumunu yakalamadaki sonuçları önemli ölçüde etkilememesini sağlamaktır. Elde edilen sonuçlar, uzay-zaman koruma elemanı çözüm elemanı (CESE) ile de karşılaştırılmıştır. Küt bir cisim etrafındaki hipersonik akış alanını doğru bir şekilde tahmin etmede şok uydurma, CESE ve viskoz olmayan Euler denklemleri (mevcut) arasında mükemmel bir uyum elde edilmiştir.

Ayrıca, A, B, C ve L tünellerindeki Apollo rüzgâr tüneli deneylerinin koşulları, yeniden giriş analizi için bir araştırma aracı olarak CFD'nin güvenilirliğini göstermek adına simüle edilmiştir. 150 ila 180 derece hücum açısı aralığında kaldırma-sürükleme oranı (Cl/Cd) açısından analiz edilen aerodinamik kuvvetler, deneysel veriler ile mevcut HAD analizi arasında iyi bir uyum olduğunu göstermektedir. Yerel akış ayrılmasını ve yeniden bağlanmasını incelemek için daha fazla analiz yapılmıştır. Deney, seçilen bazı hücum açılarında rüzgâr üstü meridyen yakınında arka gövdede yerel bir akış ayrımı ve yeniden bağlanma olduğunu göstermiştir. Mevcut çalışmadaki simülasyonlar da aynı değerleri göstermiştir. Son olarak, gradyan tabanlı anizotropik mesh adaptasyonunun çözüm doğruluğu üzerindeki etkisini anlamak için yakınsama çalışması yapılmıştır.

1. INTRODUCTION

The term atmospheric reentry can be defined as the motion of space vehicle as it enters the atmospheric environment of a given plant (earth in most cases) from the cold space environment. As astronauts returns from space at a very high speed, the atmosphere behaves like a dense fluid wall that represent and obstacle. Astronauts must attempt to enter the atmosphere with great precision and at the desired speed and angle of attack to avoid fatal accidents. This narrow path that the space vehicle must flow is known as the reentry corridor. If their approach is too narrow, they risk skipping off and back to the cold space environment and if their approach is too head-on it could result in a fatal accident and the destruction of the space capsule due to tremendous heating or experience excessive g-loads. For these reasons understanding the flow characteristics during atmospheric reentry is crucial for the successful continuation of human space exploration. Atmospheric reentry capsules are usually blunt bodies designed to survive the tremendous aerodynamic heating during the reentry phase. Astronomical missions are gaining global importance as mankind continues its mission of moving outer space. A vital example of such missions is the transportation of payload and people especially the entry and re-entry into interstellar atmosphere at a favorable condition. Re-entry capsules are generally used in re-entry missions and sometimes can even be used for interplanetary missions. Hence, the study and design of a capsule is to be done with utmost concern over the life of astronauts and success of the mission [1]. In this thesis, the flow around Apollo AS-202 capsule is to be analyzed by solving compressible Reynold's Averaged Navier-Stokes (RANS) equation with Spalart Allmaras turbulence model. Flow simulations were done at various trajectory points corresponding to a various Mach number angles of attack under different atmospheric freestream conditions by using open source CFD code (SU2) coupled with an anisotropic mesh adaptation library (pyAMG).

1.1 Literature Review

For over 20 years, computational fluid dynamics CFD has gained popularity as an aerodynamic research and analysis tool. One of the areas where is CFD is greatly applied is the simulation of hypersonic flows of an atmospheric reentry vehicle. This is because such flows are characterized with a tremendous amount of heat generation due to excessive aerodynamic heating (to be explained in section 1.3), turbulence and thermal non equilibrium. Thus, CFD is widely used as a simulation tool to study supersonic and hypersonic flows as the flow characteristics such as rarefied conditions with low density and high enthalpy are difficult and expensive to be simulated in wind and shock tunnels [2]. Experimental investigations in wind and shock tunnels are extremely costly and challenging to conduct at high enthalpy conditions. This is the reason for the popularity of CFD as an analysis tool as it is a much more economical approach for analyzing and understanding the characteristics of such flows.

Even though the use of computational fluid dynamics as an acknowledged tool for design, analysis, and optimization is getting more attention, its accuracy is dependent on using an appropriate physical model like, governing equations, turbulence-transition and boundary layer, and fluid model for the computational analysis [3]. Because of the uncertainty of the accuracy of the CFD models, the solvers need to be validated with experimental data. There are few supersonic and hypersonic wind tunnels available for experimentation who provides data that could be used to validate the CFD solvers. These facilities design for aerothermodynamics analysis usually operates below Mach 10. [3]. Aerothermodynamics is a term used to describe a method of analysis where aerodynamics is coupled with thermodynamics to study a high enthalpy flows like the flow past a reentry vehicle. Some of the high enthalpy facilities and wind tunnels in existence for hypersonic and supersonic analysis include; F4 at ONERA Le Fauga, (the ‘hot shot’ facility) and the piston-driven ‘shock tube’ HEG at DLR Gottingen, DLR Cologne, Scirocco facility at CIRA Capua, AEDC VKI hypersonic wind tunnels and recently commissioned plasmatron facility at VKI Brussels [3]. The operating Mach number of these facilities is below 10, above that CFD is relied upon for the analysis of such flow. However, to do these with a high level of confidence the CFD codes need to be verified. The validation of CFD codes can be achieved by comparing the results at below Mach 10 with the results of the recorded from experimental techniques, such as the data recorded from the above-mentioned facilities. The use of CFD is dependent on the definition of test cases, post processing of results and good interpretation of the data. In order to achieve CFD validation, ESA, DLR and many other institutes organize several workshops and provides the data that could be used for the validation. Above Mach 10 where these facilities do not operate, a verified CFD code is relied upon to provide insight on the characteristics of these regime. This extrapolation technique is based on the assumption that since the code gives reliable and varied results below Mach 10, the same could be hold true for flow above Mach 10. Nonetheless, free flight data is required to verify the extrapolation methodology and correct any misgiving regarding the extrapolated results. The free flight and wind tunnel experiment data for the Apollo AS-202 command module is freely available [4] and would be used for comparison and verification of the CFD code used in this thesis. Verification and validation of CFD extrapolation methodology is particularly important for man related missions as an important step towards the continuation of space exploration as mankind continues its quest of sending astronauts to space environment and other planets to collect data, samples and return to earth atmosphere safely for further investigation.

1.2 Flow Field

At the reentry phase, a strong detached shockwave is observed in front of the reentry capsule. The region afterward the shockwave, a shock layer characterized with an enormous enthalpy and temperature is observed once again, resulting in a severe heating environment around the capsule. The characteristics of the flow filed around reentry capsule include earth’s orbital re-entry speed nearly twenty-five Mach number, temperature of the flow typically high to the extent where the covalent chemical bonds of the air and diatomic molecules are broken. The broken molecules particles produced electrically charged plasma around the space vehicles, reentry occurs at many kilometers above sea level and thus the air density is very low. A bow shock formed ahead of the vehicle slows down the hypersonic flow. In re-entry phase, the thermal loads play a major part [5]. An image description of some salient features of the flow field around Apollo AS-202 capsule during hypersonic reentry is shown in Figure 1.1.

In literature, hypersonic flow is used to refer to flow regions in which the associated Mach number is above 5 magnitude [6]. As capsules fly from subsonic (Mach < 1) to hypersonic, remarkable physical changes take place in the flow: a shock wave is generated by the surface of the object and physical properties are altered instantly across the shock because of intense compressibility. Hypersonic flow field is different from those of subsonic and supersonic flow field, in a hypersonic regime, nondimensional variables such as lift, drag and pressure coefficient, and flow field structure become Mach number independent. This is the idea behind the Mach number independence hypothesis for hypersonic flow [6]. To distinguish and characterize a flow from supersonic, the hypersonic regime can also be suitably defined by certain physical and chemical changes which are prominent. These changes could be because of chemical and thermal non-equilibrium, real gas effects, and aerodynamic heating [7]. However, in this thesis only the aerodynamic heating effects is considered, an ideal gas assumption would be maintained and no chemical reaction would be simulated.

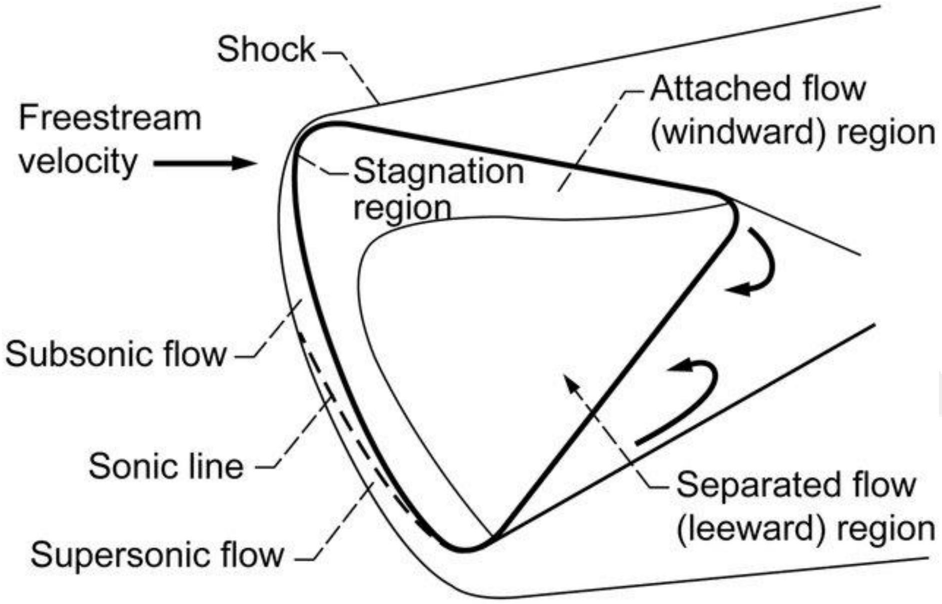

Figure 1.1 : Description of flow field around Apollo AS-202 reentry capsule [8].

1.3 Aerodynamic Heating

Aerodynamic heating refers to the heat generation on a solid body due to extreme aerodynamic conditions on the body. When a solid body passes through air at a very high speed, its kinetic energy is adiabatically transformed into heat energy by skin friction generation on the surface and by means of heat transfer. The energy conversation depends on the speed and viscosity of the air, and the conductive properties of the solid [9]. A major consideration in the design of reentry capsule is aerodynamic heating, as it is one of the dominating factors in hypersonic flow [6]. Space vehicles and designed with a blunt nose rather than sharp nose as the former creates a shock wave detachment in front of the vehicle which reduces the magnitude of the aerodynamic heating, which if left uncheck would lead to destruction of the space vehicle and endangered the life of the astronauts. An example of such a tragic accident due to aerodynamic heating is the February 2003 incident when the Columbia space shuttle crumbled during atmospheric reentry over Texas airspace. During the lunch of the space shuttle, debris damaged the integrity of the thermal protection tiles at the left wing’s leading edge. As a result, hot air was able to make its way into the internal structure of the wing and destroy it. Radiation and thermal conduction are the two dominant physical mechanisms that create atmospheric heating. Understanding aerodynamic heating properties is a broad subject which in its own right, and for further reading reference [10] is suggested. It provides a satisfactory discussion on aerodynamic heating as applied to hypersonic flows. A design rule for reentry vehicles mentioned by Raymer is as follows; *“To minimize aerodynamic heating, the vehicle must be a blunt body, i.e., have a blunt nose”* [6]

Due to this reason, all known successful reentry vehicles are characterized with a blunt nose and rounded leading-edge wings. The Apollo AS-202 CM to be analyzed in this project has a blunt nose as all the apollo mission capsules. Other example includes the space shuttle, and the intercontinental ballistic missiles. However, there is a design restriction on the radius of curvature of the blunt nose in order to minimize the drag and in turn increase the lift to drag ratio.

1.3.1 Thermal protection systems

As described in previous section, during re-entry mission, the flow environment gets very hot. So, how does this massive heat accumulation get dealt with in manner that capsule surface materials do not burnt up? The answer is; engineers use a specially designed material to protect the surface, a technique known as Thermal Protection System (TPS). The TPS serves as a protection layer that absorbs heat and protect the reentry capsule’s surface during the extreme conditions of atmospheric reentry. Another important objective of the TPS is the protection of the vehicle surface from the cold of space while in orbit [11]. The energy generated during atmospheric reentry could either be deposited, rejected or absorbed. This is underlaying design principle of the Thermal Protection System. There are three popular approaches to TPS design as follows:

1.3.2 Heat sinks

This is the early concept developed by engineers in the 1950s to deal with excessive heat of atmospheric reentry. Initially, the heat could not be gotten rid up, so a system is designed to store the energy inside the space vehicle, this is called a heat sink. An additional material is used to absorb the heat, this heat absorption ensures lower peak temperature [12]. The idea behind the heat sink is simple, in order to protect the capsule integrity more material should be added to the surface. It is based on a principle that a space vehicle with more material on the surface, would absorb more heat than a space capsule with less material. Hence whenever a space capsule experiences a specific amount of heat at a particular reentry conditions, designers and engineer could reduce the peak temperature by adding more material to the surface to absorb extra heat. Although the underlaying principle behind the heat sink is simple and effective it comes at a cost which is increasing the weight of the space vehicle. The additional weight would require more powerful propulsion system which would cost more money or sometimes even beyond the available technology. A proposed compromise was reducing the mass of the payload to account for the addition heat sink weight. But acknowledging that the payload is the target of the missions, engineers and designers had no option but to explore other options to the simple and effective but heavy heat sinks.

1.3.3 Ablations

This concept takes the advantage latent heat of fusion. This is done by covering the vehicle's surface with a specifically formulated material with a very high latent heat of fusion. Some of the used materials are carbon and ceramics. While this material melts or vaporizes, it absorbs up in the process a significant quantity of the heat energy and shields the capsule in return. The melting and absorption process is referred to as ablation [12]. This particular design approach was utilized by many engineers and designers on the warheads of ICBM, space exploitation capsules and other manned re-entry vehicles. The Apollo AS-202 reentry capsule to be analyzed in this thesis also uses the same thermal protection. Russia's manned vehicles still practices this technique for protection of their cosmonauts during atmospheric reentry. However, ablation technique has one paramount disadvantage. At the moment the capsule lands, a portion of it has melted. This implies that a brand-new vehicle must either be built for the upcoming mission or a complete overhaul is required. In the process of finding the solution to tackle this problem, engineer developed the world's first reusable space vehicle. Thanks to an innovative solution, radiative cooling.

1.3.4 Radioactive cooling

Radioactive cooling is the process of emitting most of the heat energy around space vehicle at equilibrium temperature before the space vehicles surface absorbs it [13]. This is done by maintain a thermal equilibrium. However, this is not as easy as it sounds. Even materials with considerably high emissivity, equilibrium temperature attained during reentry may exceed their melting point. The high temperatures of reentry present two challenges to designers in obtaining materials for radiative cooling. The first problem is that a selection must be made such that a surface-coating material must have a high melting point and at the same time with high emissivity. The second problem is the effect of the radiative material on the aluminum surface of the capsule. If the coating material is directly placed against the surface aluminum with considerable low melting point will melt quickly. To avoid this an insulation material with high emissivity must be placed between the hot surface coating and the capsule surface. This crafty arrangement of insolation material between the hot coating and the aluminum surface describes the, now famous, Shuttle tiles [13]. Figure 1.2 shows the schematic of the Apollo AS-202 reentry capsule. It is designed to carry two astronauts to outer space and back to earth.

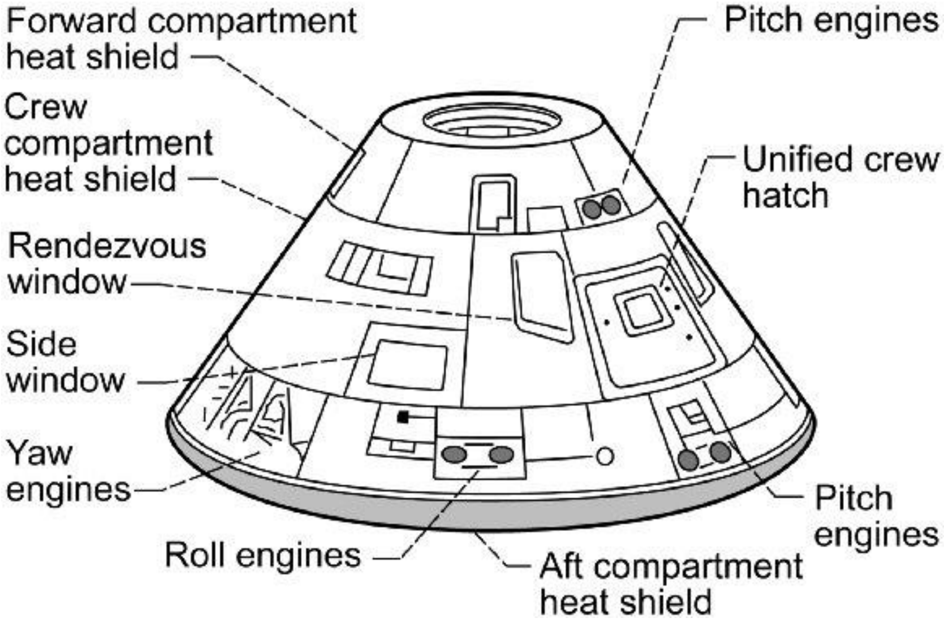

Figure 1.2 : Apollo AS-202 command module [8].

1.4 Stanford University Unstructured Solver (SU2)

SU2 is a multiphysics CFD solver developed mainly for aerospace application in design, analysis and optimization of engineering problems primarily unstructured mesh computational domain. [14]. The main area of applications of this software are non-reacting aerospace computational fluid dynamics, two dimensional and 3D dimensional aerodynamic shape optimization. However, recently the scope has been widened to solve other physical problems like electrodynamics, structural deformations and high enthalpy chemically reacting flows. The main developers of this open-source solver are the ADL lab group at Stanford University. C++ and Python are the two-dominant language in which the program is written in. Vertex-based discretization technique used in SU2 than the more general centered based discretization. This means the flow variables are stored on the vertices in contrast to centered base discretization. SU2 can work with mixed elements in 3-D including tetrahedral, pyramids, wedges and hexahedral. The software support both discrete and continuous adjoint method in computing the gradients and sensitivities of a scalar field. As of recent, fluid-structure interaction is integrated into the solver. For turbulence modelling, available models include one equation Spalart-Allmaras and two equation SST [15].

As a research open-source solver, the SU2 package would be used in the present work to solve the supersonic and hypersonic flow around the reentry capsule. It is a well-known program around the globe and is being used by many academician and research engineers. As of 2017 there were more than 12,000 thousand downloads with website visit from about 182 countries [15].

Solving Aerospace and mechanical engineering computational is the main goal of the solver and hence the backbone of the package is a Reynolds-averaged Navier–Stokes (RANS) equations. But, more recently, with the implementation of an adjoint method, SU2 which can provide gradient information that can be used for optimal shape design, uncertainty quantification, and goal oriented adaptive mesh refinement [14], [15].

The above ability of solution-based mesh adaptation would be utilized in the present work by coupling SU2 with another open-source mesh adaptation package (PyAMG) for and anisotropic adaptive mesh refinement. In the recent release of SU2, it contains a solver called NEMO for non-equilibrium models and high Mach number. To summarize, the SU2 suite has the following capabilities:

- Solves compressible and incompressible RANS, Navier-Stokes, and Euler equations.
- Solves thermochemistry and high Mach number flow using SU2 NEMO
- Adjoint-based design using unstructured meshes and high-fidelity analysis capability.
- Other partial differential equation solver for electrodynamics, thermochemical non-equilibrium, linear elasticity, wave equation and heat equation,
- Convergence acceleration (multi-grid, preconditioning, etc.).
- Goal-oriented mesh adaptations.
- Parallelization with MPI.
- Python scripts for automation.

1.5 Outline

The outline of the present thesis is classified as follows:

Chapter 1 contains the introduction and literature review on atmospheric reentry, computational fluid dynamics, and introduction to the CFD solver.

Chapter 2 gives the mathematical formulation of the governing equations. The compressible Navier-Stokes's equations, and the compressible Euler equations are presented in detailed. The mathematical formulation of Spalart-Allmaras one-equation turbulence model is given and other numerical methods used are explained.

Chapter 3 gives the overview of unstructured mesh generation techniques and their advantages. Furthermore, the metric-based framework for anisotropic mesh generation used by pyAMG which is based on solving a Riemannian metric space rather than the classical Euclidean space. The advantages and challenges of such techniques are highlighted and the difference between goal-oriented and solution-based mesh adaptations are discussed.

In chapter 4, the validation of hypersonic flow over a unit cylinder at Mach 6 is presented. The results are validated with results from other numerical methods which includes shock fitting technique and space-time conservation element solution element (CESE) methods.

Chapter 5 described the background of the Apollo AS-202 reentry capsule, flight data instrumentation, aerodynamic reconstruction modelling of geometry in CAD and meshing for the capsule surface and the computational domain while chapter 6 gives the results of the simulation of flow around the AS-202 reentry capsule and validation with experimental data.

Chapter 7 gives the conclusion, recommendation, and future work.

2. GOVERNING EQUATIONS

2.1 Compressible Navier-Stokes Equation

The governing equation for the flow analysis is the Navier Stokes equations. The differential form of Navier Stokes can be represented as follows:

$$
\begin{aligned}
&\frac{\partial}{\partial t}\begin{bmatrix}\rho\\ \rho u\\ \rho uv\\ \rho w\\ E\end{bmatrix}+\frac{\partial}{\partial x}\begin{bmatrix}\rho\\ \rho u^2+p\\ \rho uv\\ \rho uw\\ (E+p)u\end{bmatrix}+\frac{\partial}{\partial y}\begin{bmatrix}\rho\\ \rho uv\\ \rho v^2+p\\ \rho vw\\ (E+p)v\end{bmatrix}+\frac{\partial}{\partial x}\begin{bmatrix}\rho\\ \rho uw\\ \rho vw\\ \rho w^2+p\\ (E+p)w\end{bmatrix}\\
&=\frac{\partial}{\partial x}\begin{bmatrix}0\\ \tau_{xx}\\ \tau_{yx}\\ \tau_{zx}\\ u\tau_{xx}+v\tau_{xy}+w\tau_{xz}-qx\end{bmatrix}\\
&+\frac{\partial}{\partial y}\begin{bmatrix}0\\ \tau_{xy}\\ \tau_{yy}\\ \tau_{zy}\\ u\tau_{yx}+v\tau_{yy}+w\tau_{yz}-qy\end{bmatrix}\\
&+\frac{\partial}{\partial z}\begin{bmatrix}0\\ \tau_{xz}\\ \tau_{yz}\\ \tau_{zz}\\ u\tau_{zx}+v\tau_{zy}+w\tau_{zz}-qz\end{bmatrix}
\end{aligned}
\tag{2.1}
$$

$$E=\rho e++\rho\frac{1}{2}(u^2+v^2+w^2);\qquad e=c_vT \tag{2.2}$$

$$P=\rho RT;\quad p=(\gamma-1)\left[E-\frac{1}{2}\rho(u^2+v^2+w^2)\right] \tag{2.3}$$

In order to write the Navier-Stokes's equation in a simpler form, some vectors are introduced for simplification.

The state vector is denoted by $\boldsymbol{Q}$. For each node in the domain, this vector is written as:

$$\boldsymbol{Q}=\begin{bmatrix}\rho\\ \rho u\\ \rho uv\\ \rho w\\ E\end{bmatrix} \tag{2.4}$$

The inviscid vector flux in the system;

$$\boldsymbol{F_i} = \begin{bmatrix} \rho \\ \rho u^2 + p \\ \rho uv \\ \rho uw \\ (E+p)u \end{bmatrix} \boldsymbol{i} + \begin{bmatrix} \rho \\ \rho uv \\ \rho v^2 + p \\ \rho vw \\ (E+p)v \end{bmatrix} \boldsymbol{j} + \begin{bmatrix} \rho \\ \rho uw \\ \rho vw \\ \rho w^2 + p \\ (E+p)w \end{bmatrix} \boldsymbol{k} \tag{2.5}$$

The next to formulate, is the viscous flux due to viscous forces. And this can be written as

$$\begin{aligned} \boldsymbol{F_v} = {} & \begin{bmatrix} 0 \\ \tau_{xx} \\ \tau_{yx} \\ \tau_{zx} \\ u\tau_{xx} + v\tau_{xy} + w\tau_{xz} - qx \end{bmatrix} \boldsymbol{i} + \begin{bmatrix} 0 \\ \tau_{xy} \\ \tau_{yy} \\ \tau_{zy} \\ u\tau_{yx} + v\tau_{yy} + w\tau_{yz} - qy \end{bmatrix} \boldsymbol{j} \\ & + \begin{bmatrix} 0 \\ \tau_{xz} \\ \tau_{yz} \\ \tau_{zz} \\ u\tau_{zx} + v\tau_{zy} + w\tau_{zz} - qz \end{bmatrix} \boldsymbol{k} \end{aligned} \tag{2.6}$$

In Euler equation the viscous interaction term (equation 2.6) is ignored. The shear stress terms are given in non-dimensional term

$$\begin{aligned} \tau_{xx} &= \frac{M_\infty}{Re_\infty}\left[2\mu * \frac{\partial u}{\partial x} + \lambda * \left(\frac{\partial u}{\partial x} + \frac{\partial v}{\partial y} + \frac{\partial w}{\partial z}\right)\right] \\ \tau_{xx} &= \frac{M_\infty}{Re_\infty}\left[2\mu * \frac{\partial v}{\partial y} + \lambda * \left(\frac{\partial u}{\partial x} + \frac{\partial v}{\partial y} + \frac{\partial w}{\partial z}\right)\right] \\ \tau_{xx} &= \frac{M_\infty}{Re_\infty}\left[2\mu * \frac{\partial w}{\partial z} + \lambda * \left(\frac{\partial u}{\partial x} + \frac{\partial v}{\partial y} + \frac{\partial w}{\partial z}\right)\right] \end{aligned} \tag{2.7}$$

$$\begin{aligned} \tau_{xy} = \tau_{yx} &= \frac{M_\infty}{Re_\infty}\mu * \left[\frac{\partial u}{\partial x} + \frac{\partial v}{\partial y}\right] \\ \tau_{xz} = \tau_{zx} &= \frac{M_\infty}{Re_\infty}\mu * \left[\frac{\partial u}{\partial z} + \frac{\partial w}{\partial x}\right] \\ \tau_{xy} = \tau_{yx} &= \frac{M_\infty}{Re_\infty}\mu * \left[\frac{\partial u}{\partial z} + \frac{\partial w}{\partial y}\right] \end{aligned} \tag{2.8}$$

The bulk viscosity λ is a property of fluid and is defined as:

$$\lambda + \frac{2}{3}\mu = 0 \tag{2.9}$$

Reentry flow field is associated with high temperature, and viscosity is a function of temperature. To accurately compute the value of viscosity at high temperature Sutherland's law is used and is written as;

$$\mu = \mu_{ref}\left(\frac{T}{T_{ref}}\right)^{\frac{3}{2}}\frac{T_{ref} + S}{T + S} \tag{2.10}$$

With the above definitions we can write the compressible Navier stokes equation in a vector form.

$$\frac{\partial \boldsymbol{Q}}{\partial t} + \nabla \cdot \boldsymbol{F}_i - \nabla . \boldsymbol{F}_v = 0 \tag{2.11}$$

$$\frac{\partial \boldsymbol{Q}}{\partial t} + \nabla \cdot \boldsymbol{F}_i = \nabla . \boldsymbol{F}_v \tag{2.12}$$

$$\iiint \frac{\partial \boldsymbol{Q}}{\partial t} dxdydz + \iiint \nabla \cdot (\boldsymbol{F}_i - \boldsymbol{F}_v)\, dxdydz \tag{2.13}$$

Applying the divergence theorem to (2.13)

$$\iiint_V \frac{\partial \boldsymbol{Q}}{\partial t} dV + \oiint_{\partial V} (\boldsymbol{F}_i - \boldsymbol{F}_v) \cdot d\boldsymbol{S} = 0 \tag{2.14}$$

Equation (2.14) is the strong integral form of the compressible Navier-Stokes's equation

2.2 Spatial Integration

In SU2 environment both finite volume and finite element discretization are available. However, in this thesis only finite volume discretization will be used. The solver stores data on the domain vertices with data structure that is edge-based on a dual grid. The midpoint of a given edge is the location where the viscous and convective fluxes are evaluated. The main difference between vertex-based and cell-centered discretization schemes can be summarized as follows; All the flow variables are primarily stored on the vertices of the computational domain in vertex-based schemes. This ensures that the stencil equation is in terms of the node information of the nearest neighbors. On the other hand, all flow primal variables are stored at the cell center of the elements in the computational domain. In this technique the discretization stencil usually involves the use of neighbors' element information. These two methods of discretization vertex-based and cell-centered) are applied on the same computational domain, it would result in a massively non identical discretization for non-simplicial elements in both 2-D and 3-D. A cell-centered scheme while has a constant size with simple stencils involves considerably large number of unknowns. On the other hand, the vertex-based scheme, has a large variable size stencils but with fewer number of unknowns. A major drawback in cell-centered discretization scheme is bulky overheads compared to vertex-based schemes on the same computational domain. This mainly due to the larger amount of unknowns associated with the cell-centered schemes [16]. The question of which discretization technique provides a more accurate solution on equivalent grid is still unanswered with high level of certainty. Thus, it is an active field of research to investigate the possibility than the bulky overheads are compensated by the increase in accuracy in the cell-centered schemes. This is especially important since intricate stencils are used in vertex-based schemes compared to cell-centered. Another specific advantage for using vertex-based approach in this thesis is due to the large aspect ratio of elements resulting from anisotropic refinement where cell centered approach usually fails under such conditions.

After integrating the governing equations over a control volume and applying the divergence theorem, a semi-discretized, integral form of the equation is obtained

$$\int_{\Omega_i} \frac{\partial \boldsymbol{Q}}{\partial t} d\Omega + \sum_{j \in N(i)} \left(\widetilde{\boldsymbol{F}}^{i}_{ij} + \widetilde{\boldsymbol{F}}^{\boldsymbol{v}}_{\boldsymbol{ij}} \right) \cdot \Delta \boldsymbol{S}_{\boldsymbol{ij}} = \int_{\Omega_i} \frac{\partial \boldsymbol{Q}}{\partial t} d\Omega + R_i(Q) = 0 \qquad (2.15)$$

Where $R_i(Q)$ is the numerical residual that represents the integration of all spatial terms for the control volume surrounding vertex *i*. $\widetilde{\boldsymbol{F}}^{\boldsymbol{i}}_{\boldsymbol{ij}}$ and $\widetilde{\boldsymbol{F}}^{\boldsymbol{v}}_{\boldsymbol{ij}}$ are the numerical approximation of the convective and viscous fluxes projected along the and edge respectively. $\Delta \boldsymbol{S}_{\boldsymbol{ij}}$ is the area of the face associated with the edge ij, Ω_i is the volume of the dual control volume and $N(i)$ is the set of neighboring vertices to vertex *i*.

2.3 Convective Flux Evaluation

The inviscid part of the Navier-Stokes's equation is called the convective term. Unlike the diffusion term which is the viscous part, the convective creates problems when it comes to numeric evaluation. The convective term can be evaluated using centered or upwind schemes in SU2. In this thesis however, two upwind schemes (Roe and AUSM) are used which will be described next. Upwind schemes can simply be sated as forward or backward derivation depending on the direction of flow information.

2.3.1 Roe flux scheme

The Roe scheme was first introduced by Roe in 1981[17]. The inviscid flux is given by;

$$\mathbf{F}(\mathbf{Q_L}, \mathbf{Q_R}) = \frac{1}{2}\left[\mathbf{F}(\mathbf{Q_L}) + \mathbf{F}(\mathbf{Q_L}) - \hat{T}\left|\hat{\Lambda}\right|\hat{T}^{-1}(\mathbf{Q_R} - \mathbf{Q_L})\right] \tag{2.16}$$

The eigenvalues are;

$$\hat{\Lambda} = \begin{bmatrix} \hat{\mathbf{U}}\cdot\mathbf{n} - a & 0 & 0 & 0 & 0 \\ 0 & \hat{\mathbf{U}}\cdot\mathbf{n} & 0 & 0 & 0 \\ 0 & 0 & \hat{\mathbf{U}}\cdot\mathbf{n} + a & 0 & 0 \\ 0 & 0 & 0 & \hat{\mathbf{U}}\cdot\mathbf{n} & 0 \\ 0 & 0 & 0 & 0 & \hat{\mathbf{U}}\cdot\mathbf{n} \end{bmatrix} \tag{2.17}$$

The right eigenvector

$$\hat{T} = \begin{bmatrix} 1 & 1 & 1 & 0 & 0 \\ u - cn_x & \mathrm{u} & u + cn_x & l_x & m_x \\ v - cn_y & v & v + cn_y & l_y & m_y \\ w - cn_z & w & w + cn_z & l_z & m_z \\ \mathbf{H} - \hat{\mathbf{U}}\cdot\mathbf{n}c & {\left|\hat{U}\right|^2}/{2} & \mathbf{H} + \hat{\mathbf{U}}\cdot\mathbf{n}c & \hat{\mathbf{U}}\cdot\mathbf{l} & \hat{\mathbf{U}}\cdot\mathbf{m} \end{bmatrix} \tag{2.18}$$

Finally, the transformed variables

$$\hat{T}^{-1}\Delta Q = \begin{bmatrix} \dfrac{\Delta p - \rho c \Delta U}{2c^2} \\ -\dfrac{\Delta p - c^2 \Delta \rho}{c^2} \\ \dfrac{\Delta p + \rho c \Delta U}{2c^2} \\ \rho\Delta\mathbf{U}\cdot\mathbf{l} \\ \rho\Delta\mathbf{U}\cdot\mathbf{m} \end{bmatrix} \tag{2.19}$$

The Roe averaged values are defined as

$$\hat{\rho} = \sqrt{\rho_L \rho_R} \tag{2.20}$$

$$\widehat{\mathbf{U}} = \frac{\sqrt{\rho_L}\mathbf{U}_L + \sqrt{\rho_R}\mathbf{U}_R}{\sqrt{\rho_L} + \sqrt{\rho_R}} \tag{2.21}$$

$$\widehat{H} = \frac{\sqrt{\rho_L}H_L + \sqrt{\rho_R}H_R}{\sqrt{\rho_L} + \sqrt{\rho_R}} \tag{2.22}$$

$$\hat{a} = \sqrt{(\gamma - 1)\left[\widehat{H} - 0.5\hat{u}^2\right]} \tag{2.23}$$

$$H = \frac{E + p}{\rho} \tag{2.24}$$

2.3.2 AUSM$^+$ -up scheme

The AUSM$^+$ -up for all speeds was proposed by Liou in [18].

$$M_{L/R} = \frac{n.U_{L/R}}{c_{1/2}} \tag{2.25}$$

Where $c_{1/2} = (C_L + C_R)/2$

$$\overline{M}^2 = \frac{|\mathbf{U}_L|^2 + |\mathbf{U}_L|^2}{2c_{1/2}^2} \tag{2.26}$$

$$M_0^2 = \min\left(1, \max\left(\overline{M}^2, M_\infty^2\right)\right) \tag{2.27}$$

$$f_a(M_0) = M_0(2 - M_0) \tag{2.28}$$

$$\rho_{1/2} = \frac{\rho_L + \rho_R}{2} \tag{2.29}$$

$$M_{1/2} = M_{(4)}^{+}(M_L) + M_{(4)}^{+}(M_R) - \frac{K_p}{f_a}\max(1 - \sigma\overline{M}^2, 0)\frac{p_L - p_R}{\rho_{1/2}c_{1/2}^2} \tag{2.30}$$

Where;

$$M^{\pm}_{(4)}(M) = \begin{cases} \frac{1}{2}(M \pm |M| & if\ |M| \geq 1 \\ \pm\frac{1}{4}(M \pm 1)^2 + \left(1 + 16\beta\frac{1}{4}(M \pm 1)^2\right) & otherwise \end{cases} \tag{2.31}$$

And $\rho_{1/2} = \frac{\rho_L + \rho_R}{2}$, $K_p = 0.25, and\ \sigma = 1$ then the max flux

$$m_{1/2} = \begin{cases} c_{1/2}\, M_{1/2}\ \rho_L & if\ M_{1/2} > 0 \\ c_{1/2}\, M_{1/2}\ \rho_R & otherwise \end{cases} \tag{2.32}$$

The pressure fluxes

$$p_{1/2} = P^{+}_{(5)}(M_L)p_L + P^{-}_{(5)}(M_R)p_R - K_a P^{+}_{(5)}(M)P^{-}_{(5)}(M_R)(\rho_L + \rho_R)(f_a c^2_{\frac{1}{2}})\ (M_R - M_L) \tag{2.33}$$

And

$$P^{\pm}_{(5)}(M) = \begin{cases} \frac{1}{2M}(M + |M| \\ \pm\frac{1}{4}(M \pm 1)^2\left[(\pm 2 - M) + 16\sigma M\frac{1}{4}(M \mp 1\,)^2\right] \end{cases} \tag{2.34}$$

Using the parameters;

$$\alpha = \frac{3}{16}(-4 + 5f_a^2) \qquad \beta = \frac{1}{8} \qquad K_a = 0.75 \tag{2.35}$$

The whole flux becomes

$$n \cdot F = m_{\frac{1}{2}}\begin{bmatrix} 1 \\ u \\ v \\ w \\ H \end{bmatrix}_a + \begin{bmatrix} 0 \\ p_{1/2}nx \\ p_{1/2}ny \\ p_{1/2}nz \\ 0 \end{bmatrix} \tag{2.36}$$

Where the local enthalpy is given by

$$H = \frac{E + p}{\rho} \tag{2.37}$$

The formulation for the two flux splitting methods used in this thesis is given above. The second order reconstruction for the upwind methods is done employing MUSCL method [19]. In order to preserve the monotonicity in the solution, a slope limiter is used. The slope limiter was used throughout the simulations in this project is the Venkatakrishnan detailed in [20]. The slope limiter limits the gradient during high-order reconstruction.

In order to evaluate the viscous fluxes with a finite volume method for both the mean flow and turbulence model, flow quantities and their first derivatives are required at the faces of the dual control volumes. The spatial gradients of the flow variables are calculated in a pre-processing step at all vertices using Green-Gauss [21] and then averaged to obtain these gradients at the cell faces when computing viscous fluxes along the edges.

2.4 Time Integration

Now that the fluxes evaluation is fully described, let us turn our attention to into techniques for time integration of the governing differential equations presented at equation (2.16) which can be written as

$$\frac{d}{dt}(|\Omega_i|\mathbf{Q}_i + \mathbf{R}_i(\mathbf{Q})) = 0 \tag{2.38}$$

Where $|\Omega_i| = \int_{\Omega_i(t)} d\Omega$. With the assumption of static mesh, where there is no dynamic deformation of the control volume during the time integration. By discretizing the time derivative term, one obtains a fully-discrete finite volume form of the governing equations. For particularly stiff problems, implicit methods can be used to improve convergence due to their increased numerical stability. Here, we use the backward Euler scheme, where the residual is evaluated using the solution state at the new time level U^{n+1}. Applying to equation (2.39) we obtained

$$|\Omega_i|\frac{\Delta\mathbf{Q}}{\Delta t} = -\mathbf{R}_i(\mathbf{Q}^{n+1}) \tag{2.39}$$

where time level n corresponds to the known solution in its current state, while time level *n + 1* represents the new solution state that is being sought after advancing one time step Δt where $\Delta t = t^{n+1} - t^n$ and $\Delta Q_i = Q_i^{n+1} - Q_i^n$. However, the residuals at time level *n + 1* are now a function of the unknown solution state Q^{n+1} and cannot be directly computed. Therefore, a first-order linearization about time level *n* is performed:

$$\left(\frac{|\Omega_\mathrm{i}|}{\Delta \mathrm{t}_i^\mathrm{n}}\delta_{ij} + \frac{\partial(\mathbf{Q}^n)}{\partial\mathbf{Q}_j}\right)\cdot\Delta\mathbf{Q}_j^n = -R(\mathbf{Q}^n) \tag{2.40}$$

where if a flux $\tilde{\mathbf{F}}_{ij}^{i}$ has a stencil of points {i, j}, then contributions are made to the Jacobian at four points.

$$\frac{\partial R}{\partial Q} := \frac{\partial R}{\partial Q} + \begin{bmatrix} \ddots & & & & \\ & \frac{\partial \tilde{\mathbf{F}}_{ij}}{\partial Q_i} & \cdots & \frac{\partial \tilde{\mathbf{F}}_{ij}}{\partial Q_i} & \\ & \vdots & \ddots & & \\ & -\frac{\partial \tilde{\mathbf{F}}_{ij}}{\partial Q_i} & \cdots & -\frac{\partial \tilde{\mathbf{F}}_{ij}}{\partial Q_i} & \\ & & & & \ddots \end{bmatrix} \tag{2.41}$$

Implicit methods enable the use of higher CFL conditions than with explicit methods, which translate to the specific values of Δt that are used to relax the problem. The resulting linear systems are typically solved using a preconditioned Generalized Minimal Residual (FGMRES) method [22].

2.5 Fluid Model

Ideal assumption is used as the fluid model for all simulation in this thesis. A specific gas constant R, and γ to denoted the ration of the specific heat with an approximate value of 1.4. Using this assumption, the pressure in given as:

$$p = (\gamma - 1)\left[E - \frac{1}{2}\rho(u^2 + v^2 + w^2)\right] \tag{2.42}$$

With the same assumption of ideal gas, the temperature can be obtained from the expression:

$$T = \frac{p}{\rho R} \tag{2.43}$$

Next thing to address is the thermal conductivity. One approach is to assume a constant conductivity throughout. A more accurate formulation is based on constant Prandtl's number Pr. Using this assumption, the conductivity becomes a function of viscosity according the relation:

$$\kappa = \frac{\mu c_p}{Pr} \tag{2.44}$$

There are other fluids model within the SU2 like standard air and other non-ideal fluid model. These are more advanced models and sometimes exhibit instability. These fluid models are not discussed as the ideal gas assumption would be used through the thesis.

The flow can be either laminar or turbulent. In the case of the former, the dynamic viscosity is denoted by μ_d. This dynamic viscosity can either be assumed to be constant or follows the Sutherland's law as a lone function of temperature. In the same manner the dynamic Prandtl's number is given as Pr_d. When the flow is turbulent; the closure problem requires addition equation. Hence, the Reynolds-averaged Navier-Stokes (RANS) equations is solved numerically. There is a standard approach to turbulence modeling based on Boussinesq hypothesis. Simply stated, the effect of turbulence is manifested as perturbations in viscosity. In turbulence modelling, the viscosity is split turbulent and dynamic component denoted by μ_t and μ_d respectively. Thus, the final viscosity is taken as the superposition of these viscosities and is represented as:

$$\mu = \mu_d + \mu_t \tag{2.45}$$

In the same manner, the thermal conductivity term in the energy equation is represented by first introducing a turbulent Prandtl number Pr_t follows by a superposition as well which is presented as:

$$\kappa = \frac{\mu_d c_p}{Pr_d} + \frac{\mu_t c_p}{Pr_t} \tag{2.46}$$

The turbulent viscosity is obtained from a suitable turbulence model that depends on the flow state and a set of new variables. Here, the scalar variable $\hat{v}$ is obtained from a one-equation turbulence model. The Spallart-Allmaras (SA) model is one of the most common and widely used turbulence models for the analysis and design of engineering/aerospace applications in it is used in this thesis, the formulation is described below [23].

2.6 Spalart-Allmaras (SA) Model

The one equation model in a non-conservative form is described by the following equations.

$$\begin{aligned}\frac{\partial \hat{v}}{dt} + u_j \frac{\partial \hat{v}}{\partial x_j} = c_{b1}(1 - f_{t2}) S\hat{v} - \left[c_{w1} f_w - \frac{C_{b1}}{k^2} f_{t2}\right]\left(\frac{\hat{v}}{d}\right)^2 \\ + \frac{1}{\sigma}\left[\frac{\partial}{\partial x_j}\left((v + \hat{v}) + \frac{\partial \hat{v}}{\partial x_j}\right) + c_{b2} \frac{\partial \hat{v}}{\partial x_i} \frac{\partial \hat{v}}{\partial x_i}\right]\end{aligned} \tag{2.47}$$

In vector form, equation (2.44) can be written in vector form as

$$R(\boldsymbol{Q}, v) = \frac{\partial \hat{v}}{dt} + \nabla \cdot \boldsymbol{F}_i - \nabla . \boldsymbol{F}_v - \boldsymbol{S} = 0, \quad in\, \Omega, \;\; t > 0 \tag{2.48}$$

Where the inviscid, viscous and source terms are given by;

$$\mathbf{F}_i = \vec{V}\hat{\boldsymbol{v}}, \qquad \mathbf{F}_v = -\frac{v + \hat{v}}{\sigma}\, \boldsymbol{\nabla}\hat{\boldsymbol{v}},$$
$$\boldsymbol{S} = c_{b1}(1 - f_{t2})S\hat{v} - \left[c_{w1}f_w - \frac{C_{b1}}{k^2}f_{t2}\right]\left(\frac{\hat{v}}{d}\right)^2 \tag{2.49}$$

The turbulent eddy viscosity can be computed as

$$\mu_t = \rho\hat{v}f_{v1} \;\;,\;\; \chi = \frac{\hat{v}}{v} \;\;,\;\; f_{v1} = \frac{\chi^3}{\chi^3 + C_{v1}^3} \;, v = \frac{\mu_{dyn}}{\rho} \tag{2.50}$$

Where:

$$S = \Omega + \frac{v}{\kappa^2 d^2} f_{v2} \tag{2.51}$$

$$\Omega = \sqrt{2W_{ij}W_{ij}} \tag{2.52}$$

$$f_{v2} = 1 - \frac{\chi}{1 + \chi f_{v1}} \tag{2.53}$$

$$f_w = g\left[\frac{1 + c_{w3}^6}{g^6 + c_{w3}^6}\right]^{\frac{1}{6}} \tag{2.54}$$

$$g = r + c_{w2}(r^6 - r) \tag{2.55}$$

$$r = min\left[\frac{\hat{v}}{S\kappa^2 d^2}, 10\right]^{\frac{1}{6}} \tag{2.56}$$

$$f_{t2} = c_{t3\mathrm{exp}}\,\exp\,(-\mathrm{c_{t4}}\chi^2) \tag{2.57}$$

$$W_{ij} = \frac{1}{2}\left(\frac{\partial u_i}{\partial x_j} - \frac{\partial u_j}{\partial x_i}\right) \tag{2.58}$$

The boundary conditions are:

$$\hat{v}_{wall} = 0 \qquad \hat{v}_{farfield} = 3v_\infty \, : \, to \, : \, 5v_\infty \tag{2.59}$$

The constants are:

$$c_{b1} = 0.1355 \quad \sigma = \frac{2}{3} \quad c_{b2} = 0.622 \quad \kappa = 0.41 \tag{2.60}$$

$$c_{w2} = 0.3 \quad c_{w3} = 2 \quad c_{v1} = 7.1 \quad c_{t3} = 1.2 \quad c_{t4} = 0.5 \tag{2.61}$$

$$c_{w1} = \frac{c_{b1}}{\kappa^2} + \frac{1 + c_{b2}}{\sigma} \tag{2.62}$$

3. ANISOTROPIC MESH ADAPTATION

3.1 Background

In general, meshes can be divided into two categories based on how their nodes and cells or elements are arranged. The two major categories of computational grid are structured and unstructured meshes. In structured grid, the nodes are aligned and placed regularly in a systematic way using similar elements. While unstructured grid makes use of irregularly placed points with varying shape of the elements. Recently, unstructured meshes have become very popular due to their flexibility in allowing varying elements shape and irregularly placed points to precisely approximate the computational domain. Unstructured meshes mostly uses triangular elements in 2-D and tetrahedral in 3-D, but sometimes may use a combination of other elements like quad, hexagonal and prism. Besides providing a great flexibility in meshing complex domain, unstructured meshes also enables mesh adaptations. Since the initially points are irregularly placed, they allow points to be deleted, added, or moved by solution-based or goal-oriented mesh adaptations. The local connectivity matrix is updated to enhance the solution accuracy. A major objective of mesh adaptations is obtaining the optimal point distribution in a computational grid that would produce the minimum magnitude of the error in a given numerical simulation. The goal of this chapter is providing overview of the anisotropic mesh technique, and the solution algorithm used by pyAMG at Inaria. This mesh adaption software incorporated with SU2 are used for obtaining solution in this thesis.

3.2 Anisotropy Mesh Generation

Anisotropy is ubiquitous in nature, that is most physical phenomenon like flow of air, formation of cloud, supersonic shockwaves, electromagnetism all exhibit anisotropy which refers to having a privileged direction in the system [24]. One of the biggest challenges in the field of mesh adaptation is achieving a high degree of anisotropy since the natural axis is always in the direction that favors anisotropy [25]. The simplest way in mesh adaptation techniques is the used of isotropy mesh adaptation. Numerous examples of such simple mesh adaptation techniques are discussed in the literature [28, 29]. While this approach gives a remarkable enhancement over the use of a fixed mesh, they are inadequate fit for solving problems that exhibit high anisotropy like shockwaves or boundary layers where there is a high order of magnitude variation in the mesh size requirements in different direction [28].

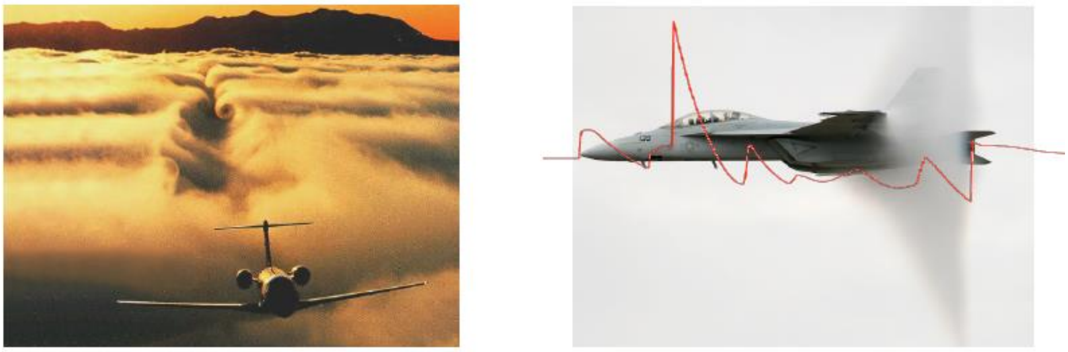

Figure 3.1 : Natural phenomenon with a strong anisotropy.

There are essentially three categories of unstructured mesh generation as follows:

3.2.1 Delaunay triangulation technique

This is based on the Delaunay criterion sometimes referred to as the “empty sphere” property which states that any node must not be contained within the circumsphere of any simplicial elements within the mesh [29]. By definition, a circumsphere is a sphere that passes through all the four vertices of a tetrahedron. This formed the basis of the Delaunay algorithm in [30]. Delaunay technique is the most used unstructured mesh generation for tringles elements in two dimension and tetrahedral in three dimensions.[31]. Figure 3.2 below gives representation of this technique.

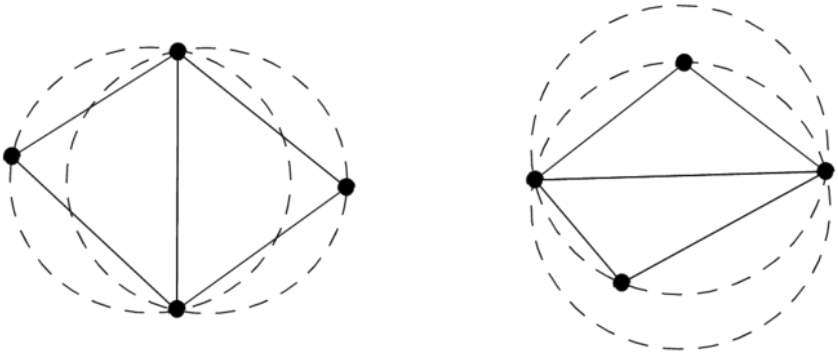

Figure 3.2 : Example of Delaunay criterion (left) and its violation (right).

In Delaunay triangulation technique, to insert a new point into the triangulation, all the existing triangles whose points are contained in the newly created points most be deleted. A new triangulation is then formed by joining the new point to all boundary vertices of the cavity created by the previous removal of intersected triangles [16]. It should be noted that Delaunay criterion is not an algorithm for mesh generation, it merely provides a set of rules in which existing points in space can be connected. Considering this, one must come with a way of generating node location for the given geometry. The most practiced method involves first meshing the boundary of the geometry which will serve as the initial nodes set. Delaunay criterion is the applied on the boundary nodes for triangulation. Nodes are added incrementally in that manner into the existing mesh. Sometimes it is necessary to redefine the tetrahedral or triangles locally in order to maintain the Delaunay criterion. Algorithm that uses Delaunay criterion differs from another based on the selected approach for defining where to locate the interior nodes. Many of such algorithm and software can be found in literature [34-37].

3.2.2 Advancing front technique

This is another commonly used unstructured mesh generation technique developed by Rainald Lohner [38, 39] at George Mason University and S. H. Lo [40, 41] at the University of Hong Kong. In this technique, tetrahedral are generated on an active front or advancing front. The tetrahedral are constructed gradually inward from the triangulated surface. For a 2-D grid, the generation initialized by discretizing the geometry boundaries and transforming them into set of edges. These set of edges serves as the initial font which would be advanced out into the field. An edge is selected as the base and a new triangle is created by joining this with two ends with either an existing point or a newly created one. The current font could then be removed as it becomes obscured by the new triangle. In the same manner, the remaining two edges of the newly created triangle are either deleted, removed from the font, or assigned to the font. This entirely depends on their visibility as shown in Figure 3.3.

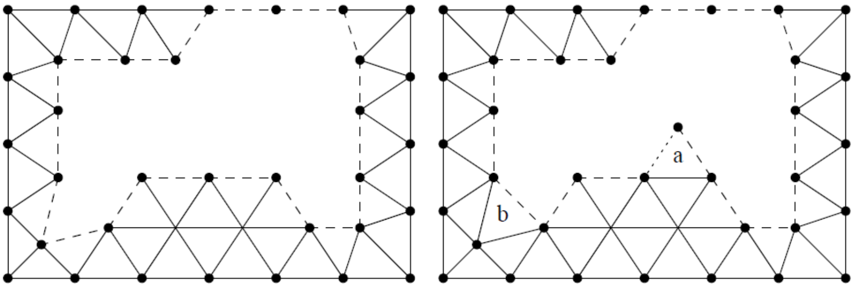

Figure 3.3 : Generation of new triangle in advancing front [16].

For the three-dimensional mesh, a surface 2D mesh is first generated on the surface boundary of the domain. Tetrahedral are used in 3-D and these are generated by as follows, a surface 2-D mesh is first generated on the boundary surface of the corresponding domain. This becomes the initial advancing font which is then translated into physical space by placing new points as the front to form the tetrahedral. In contrast to 2-D the intersection checks required involves triangular front faces in supposed to edges. Advancing front is highly efficient and generally produced higher quality triangulations across the flow field. However, sometimes difficulty arises in regions where the fronts must be combined together.

3.2.3 Octree/Quadtree

This is a technique that was first introduced by Mark Shepard group at Rensselaer in the 1980s [42,43]. The technique utilizes space subdivision is recursive manner to achieve the required resolution. An octree or quadtree is generated with the vertices forming the grid points. Either triangular or tetrahedral elements are formed by dividing the obtained octant or quadrant for 2-D and 3-D. It is noteworthy to emphasize that the octree or quadtree elements that are in intersection with the surface boundary and the vertices at the boundary is required to be positioned to coincide with the boundary. This approach is considerably easy and low-cos results in efficient and high-quality mesh in the domain's interior regions. The major disadvantage of this technique is that in has a great tendency of producing irregular elements distribution in vicinity of the boundary region.

3.3 pyAMG Mesh Adaptation

The suite uses a metric based adaptation technique which was first presented in the earlier works [42]–[44]. By using this technique, any given uniform unstructured mesh can be converted to anisotropic mesh by solving the distance in Riemannian space rather than the more classical approach of Euclidian metric space. If we let Ω to represent the tensor filed metric, by definition it is a Riemannian space which could be represented by $(M(x))x \in \Omega$, where $M(x)$ is a positive definite symmetric matrix with a dimension of 3 x3. The discrete field $Mi = M(xi)$ can be defined by taking the field at each xi vertex of the mesh H of the metric tensor filed Ω. Let the number of vertices in H be donated by N, then the linear discrete matric field can be denoted by $(Mi)i=1...N$. Since $M(x)$ and Mi are both positive definite and symmetrical, using orthonormal frame they can be diagonalized in such a way that:

$$M(x) = R(x)\Lambda(x)R(x) \text{ and } M_i = R_i \Lambda_i R_i \tag{3.1}$$

Where $\Lambda(x)$ and $\Lambda_i(x)$ consist of only positive eigenvalues R and R_i which are diagonal and at the same time orthonormal matrices. It should be noted that set of points varying the implicit equation

$$x^t M_i x = 1 \tag{3.2}$$

Represented an inimitable ellipsoid. The ellipsoid is referred to as a unit-ball of M_i and is used in geometric representation of M_i . Two of the basic procedures in mesh generation are the calculation of length and volume. The length of an edge

$e = [x_i, x_j]$ and the volume of an element K are to be evaluated continuously in $(M(x))x \in \Omega$ by:

$$l_M(e) = \int_0^1 \sqrt{e^t M(x_i + e^t)e}\, dt \text{ and } |K_M| = \int \sqrt{\det\left(M(x)\right)}\, dx \tag{3.4}$$

$$|K_M| \approx \sqrt{det\left(\frac{1}{4}\sum_{i=4}^{4} M_i\right)}\, |K| \text{ and } l_M(e) \approx \sqrt{e^t M_i}\, \frac{r-1}{rln(r)} \tag{3.5}$$

Where |K| is the Euclidian volume of K and r length ration. The framework is shown in figure 3.4

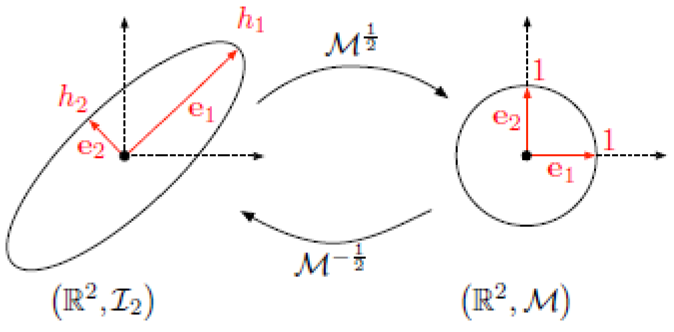

Figure 3.4 : Metric based framework.

The goal of any adaptive mesh generation is to produce a qualitative mesh with reference to a given metric filed. Hence, a quality control function is needed to. Based on the metric field, a quality function is defined as:

$$Q_M(K) = \frac{3^{\frac{1}{3}}}{36} \frac{\sum_{i=1}^{6} l_M^2(e_i)}{|K|_M^{\frac{2}{3}}} \in [1, \infty] \qquad (3.6)$$

The mesh generation procedures can be highlighted as follows:

- Given a metric field, produce a qualitative unit mesh with respect to it
- Preform the necessary local mesh operations
- Perform standard mesh operation like edge collapse, swaps, point insertion, deletion, etc.

In pyAMG: all these operations are embedded in a cavity-based operator.

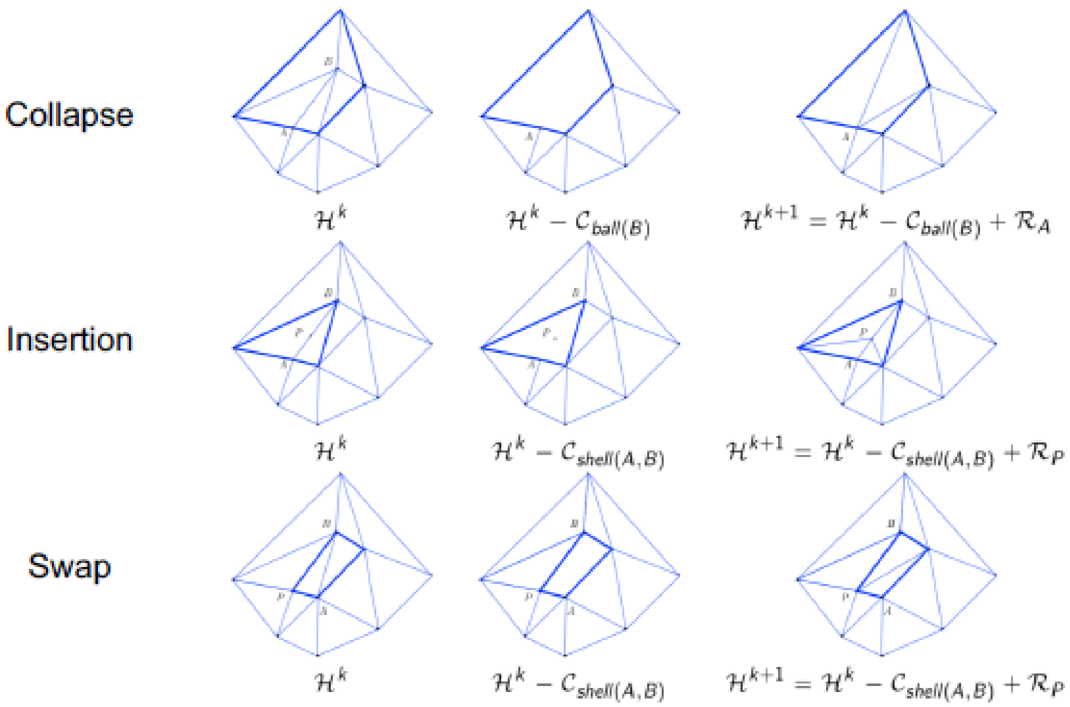

Figure 3.5 : pyAMG mesh operations [45].

The objective in employing mesh adaptation to solving computational dynamics problems improve accuracy and computational time. Mesh adaptation procedure depends on two essential operations which are edge collapse and edge break. Combing these two operations with a quality control function is sufficient enough generate high quality mesh. Figure 3.6 shows the work flow of the simulation in SU2 and the solution-based adaptations by calling the pyAMG library. The process is automated and controlled by a python script as an interface.

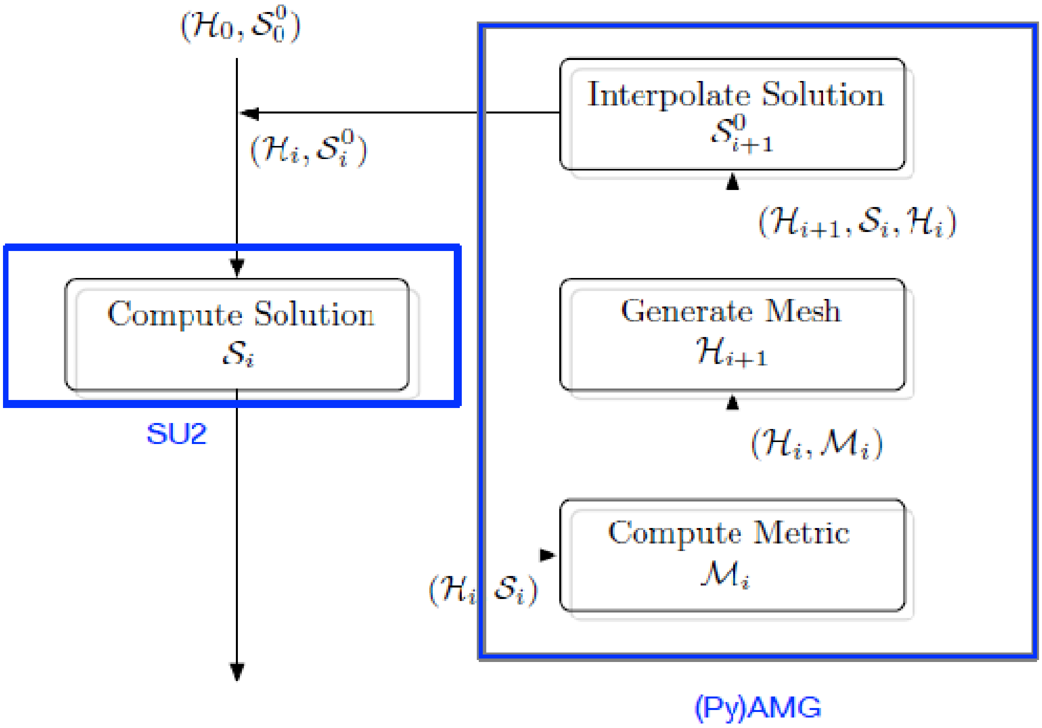

Figure 3.6 : pyAMG mesh adaptation algorithm.

There are two approaches to mesh adaptation; solution-based adaptation and goal-oriented mesh adaptation. The goal-oriented mesh adaption is derived by an error estimation function of the quantity of interest (QoI). The quantity of interest could be drag of an aircraft fuselage or wing. The other approach is a solution-based mesh adaption, and it is used in the current study. This approach is derived by the metric field generated from a given solution of the governing equation. In pyAMG there are options to choose a sensor (fluid property) with respect to which the metric field would be generated. The sensor for the current study is the Mach number after a modification to the default setting. On solid wall, a Mach 1 was used rather than zero. This high gradient leads the refinement of the boundary layer. Otherwise, the boundary layer mesh where the Mach gradients are weak such as separation points may be lost.

4. HYPERSONIC FLOW OVER A CYLINDER

4.1 Background

In this chapter, the validation of the solver in predicting hypersonic flows is presented. Obtaining accurate results of hypersonic or supersonic flows using unstructured meshes while maintaining numerical stability is a difficult task in computational fluid dynamics. Despite years of progress in numerical computation of bow shocks using structured meshes and upwind scheme, there are records depicting the infamous carbuncle problem in which numerical stability connected with the stagnation region behind shockwaves causes the shockwave region to be significantly unstable [55–57]. This numerical instability problem related to bow shock is even more serious when finite volume discretization is operated in unstructured computational domain [55,56].

One of the most popular way of validating a solver's capability in accurately predicting shock region is by comparing the solution to a shock fitting results. Euler equation is solved in the shock fitting approach on discretized computational domain that is in front of the body but behind the shockwave. The purpose of this technique is to ensure that the problems associated with numerical instability and accuracy dependency do not significantly affect the results in capturing the precise location of the shockwave, [49]. In this thesis, a flow at Mach 6 over a cylinder is chosen as a reference to study the accuracy of the SU2 in predicting inviscid hypersonic flow. A shock fitting code based on the work of Salas and Atkins [50] is used as a the baseline solution benchmarking the accuracy level.

4.2 Simulation Description

The first validation problem in this case is the well-known problem of hypersonic inviscid flow over a cylinder. The hypersonic flow over a cylinder is chosen as the first test case due the fact that the problem is not overly complicated while the solution is non-trivial and has been used as a research study case by others due to its simplicity and interesting physical flow features. An O-type computation domain is a used with a far-field radius of 50D and the cylinder located at the center of the domain, where D is the diameter of the cylinder which is one unit for this study. The reason for the expansion of the domain is to capture accurately the flow conditions with no interactional effect of the boundary condition. The initial mesh contains 26,192 unstructured triangular elements and 13,336 points. The mesh is finer near the surface of the cylinder to accurately resolve the boundary layer for initial solution which would be used for the anisotropic mesh adaptation. The far-field boundary conditions imposed at the outer circumference of the O-grid and the Euler-wall (slip) boundary condition is applied on the surface of the cylinder. The simulation is normalized with freestream velocity equals Mach number for simplicity as our interest is accurately capturing the shock region. Roe, and AUSM, fluxes are all tested to compare their accuracy for the hypersonic flow. A constant Courant-Friedrichs-Lewy number (CFL) of 20 is used for the simulations, The angle of attack is zero, the flow Mach number is 6, and the fluid medium is assumed to be perfect gas. Green-Gauss theorem is used for gradient computation. For the time integration, Euler implicit method is used for the for numerical integration, FGMRES is used for solving the linear system with ILU preconditioner. The convergence criterion for the linear solver is 1.0 x 10^{-10} based on the residual of the continuity equation.

4.3 Simulation Results.

The inviscid Euler equation is solved around a unit cylinder. Figure 4.1 give the comparison of the solution using SU2 in present study in comparison to shock-fitting by [50] and solution obtained using a space-time conservation element solution element (CESE) method by [49]. The comparison has shown good agreement between these methods and SU2 solver used in present study.

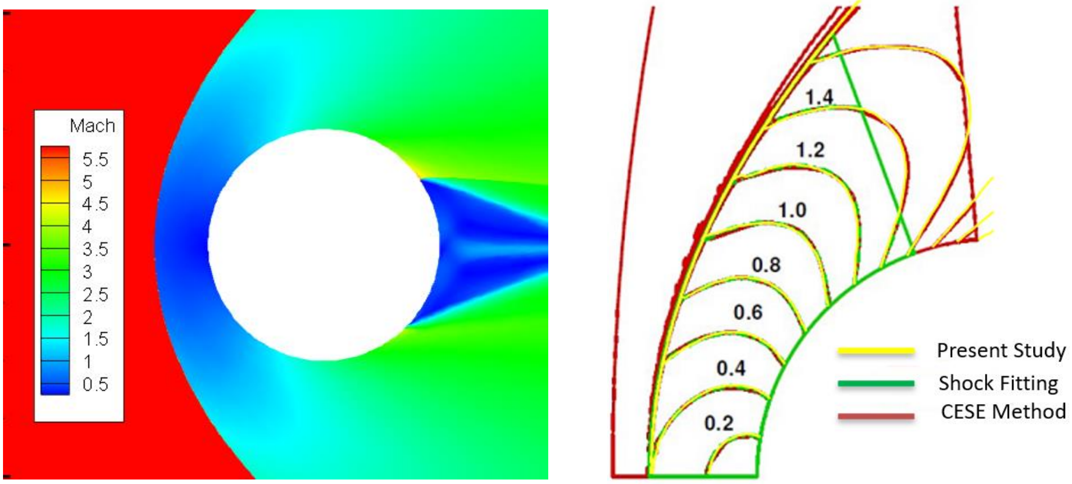

Figure 4.1 : Comparison Mach number contour level obtained in present study vs Shock-fitting and CESE Methods for flow over a cylinder.

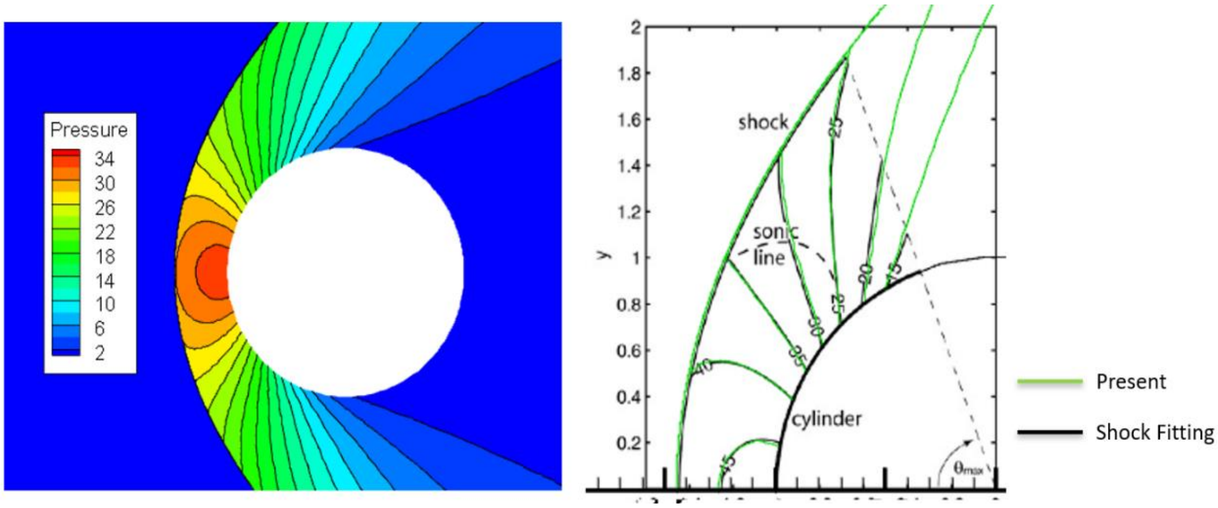

Figure 4.2 : Comparison of Mach number contour level obtained in present study **vs** Shock-fitting method for flow over a unit cylinder at Mach 6.

The comparison of pressure contour level obtained using SU2 in present study and shock-fitting results are shown in Figure 4.2. The Validation of the accuracy of SU2 in capturing the true shock location for flow around a blunt body is demonstrated in these Figures.

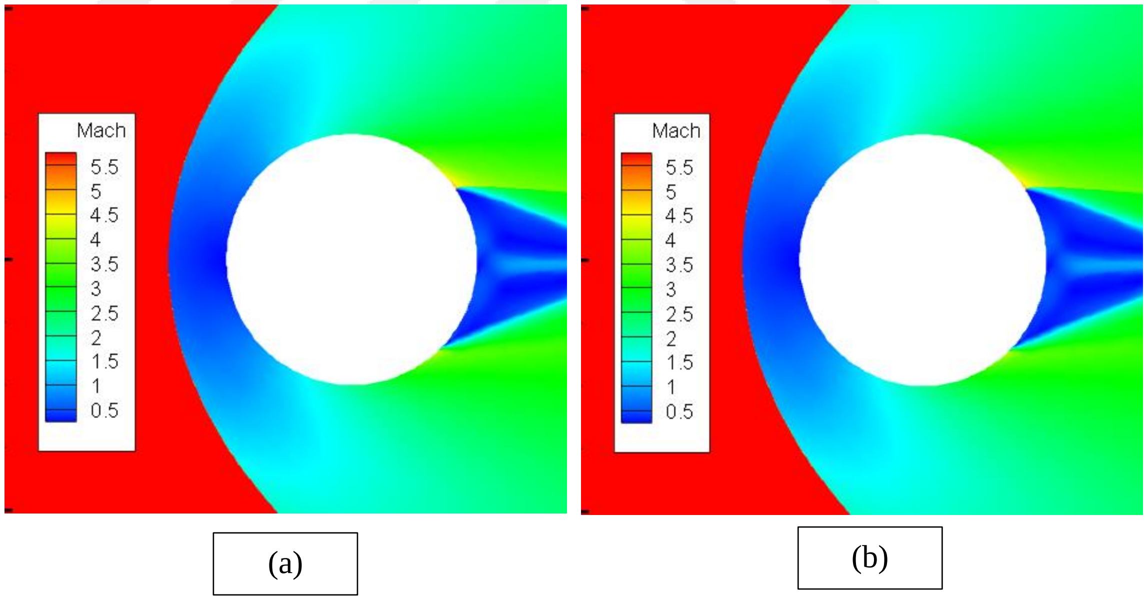

(a)

(b)

Figure 4.3 : Roe (a) and AUSM (b) Mach number contours Comparison.

To compare the results and stability of the two convective flux computation methods, Roa and ASUM are both used to solve the inviscid flow over the cylinder. The two methods give similar results as can be seen in Figure 4.3.

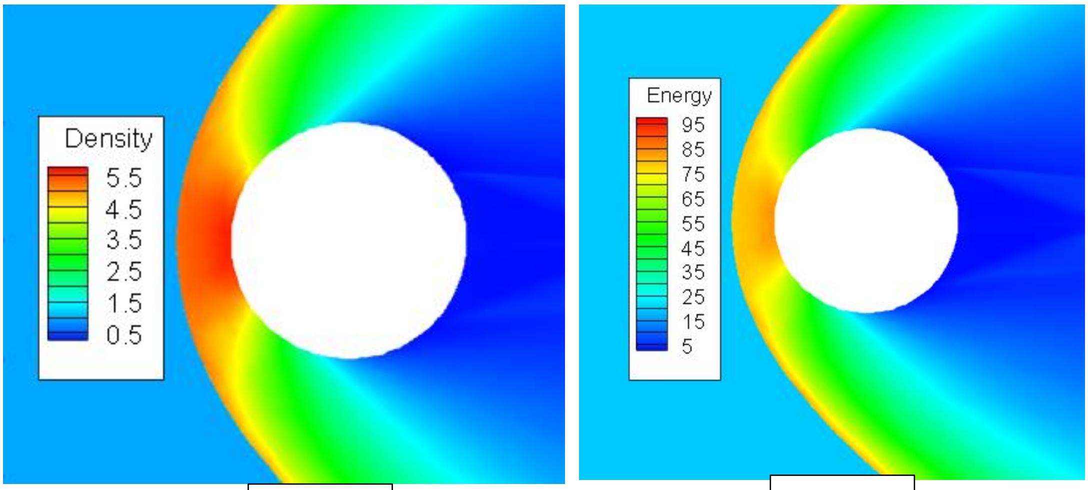

(a) (b)

Figure 4.4 : Density (a) and Energy (b) contours flow around a cylinder at Mach 6.

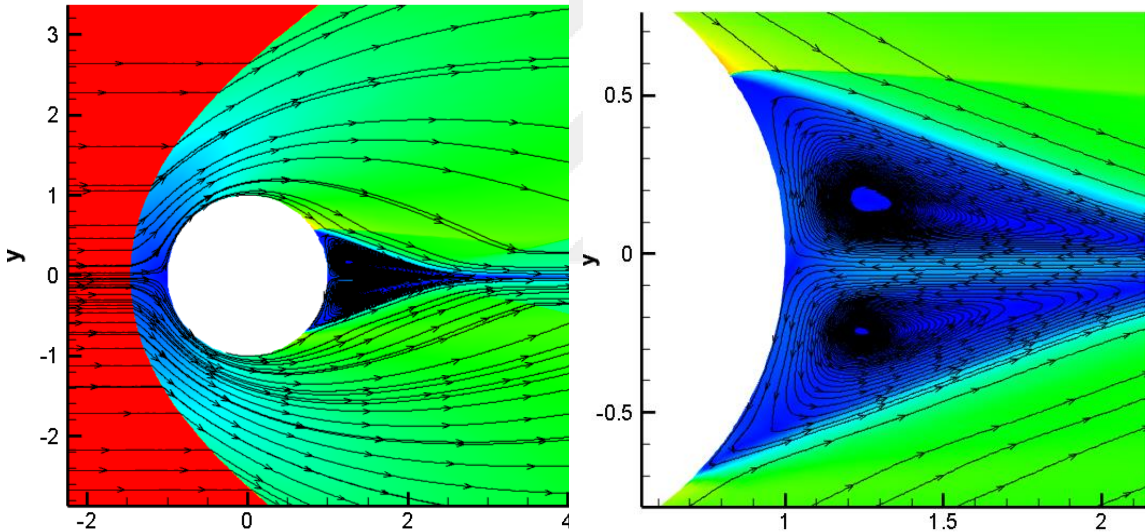

(a) (b)

Figure 4.5 : Streamlines (a) and the magnified view of circulation region (b) behind the capsule for inviscid flow around a unit cylinder at Mach 6.

The density and energy level contours are shown in Figure 4.4. It is important to note that the simulation has been normalized for simplicity and the values in the Figure are thus the normalized level. Figure 4.5 shows the nature of the streamlines for inviscid flow over a unit cylinder at Mach 6. There is a circulation region behind the cylinder as can be seen in Figure 4.5 (b).

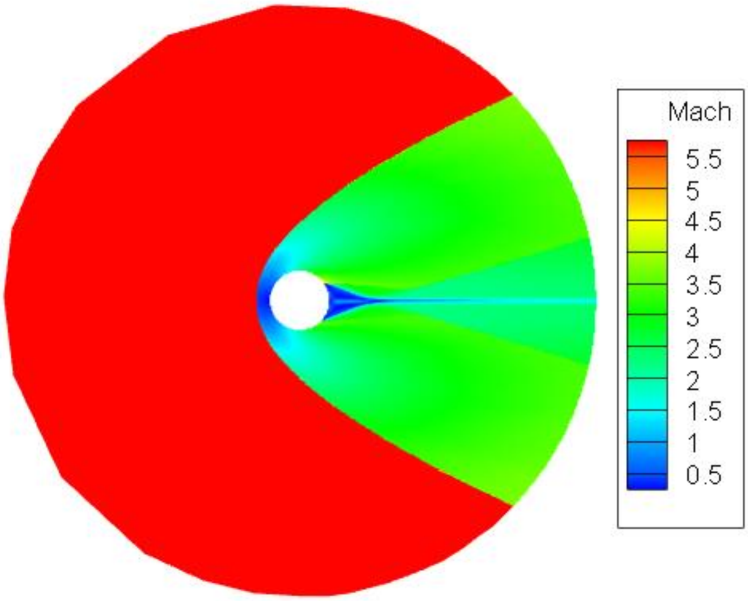

Figure 4.6 : Full domain with Mach number contours for flow over a cylinder.

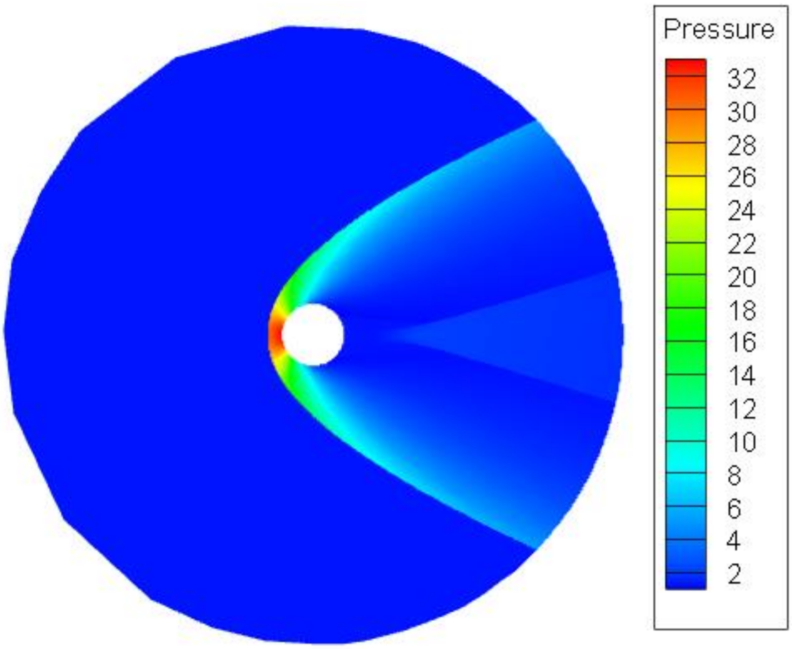

Figure 4.7 : Full domain with pressure contours for flow over a cylinder at Mach 6.

The full computation for the inviscid flow over a unit cylinder is shown in Figure 4.6 and 4.7. The computation domain is a circle with the cylinder at its center. The advantage of having a significantly extended domain is that the large far field boundary allows the simulation to fully develop without interference.

4.3.1 Mesh adaptation study

The simulation results for inviscid perfect gas flow over a cylinder at Mach 6 described in the previous section is obtained by solving the compressible Euler equation of successive refined domain. The mesh adaptation software pyAMG is coupled with the CFD solver SU2 which allows the solution-based mesh adaptation. The sensor function for the adaptation is based on the Mach number. The minimum and maximum length of edge allowed were 1.0 x 10^{-8} and 100 units respectively. The record of the number of vertices and triangular elements at each iteration level is given in Table 4.1.

Table 4.1 : Anisotropic mesh adaptation summary for flow over cylinder.

Refinement Level	Number of vertices	Number of Elements
Initial mesh	4,378	7,494
Iteration 1	11,354	22,355
Iteration 2	18,240	33,721
Iteration 3	25,445	50,400
Iteration 4	30,566	60,608
Iteration 5	44,521	85,257
Final Refined	49,682	95,376

The use of mesh adaption has significantly improved the solution of the inviscid perfect gas flow over a cylinder at Mach 6. The number of points at each iteration is shown in table 4.1. The computational domain is a c circle with the 2D cylinder at the center. Looking at the table, the number of points increases after each iteration. The points distribution changes by every iteration. Figure 4.8 Shows the solution and the points distribution around the unit cylinder. We can see the meshes became finer new the shock region and coarser as we move towards the boundary. Figure 4.8 also compares the mesh and corresponding solution at three different level of the mesh adaptation. The initial mesh has a uniformly distributed points, but the points distribution is changed at every iteration to form an anisotropic triangular element.

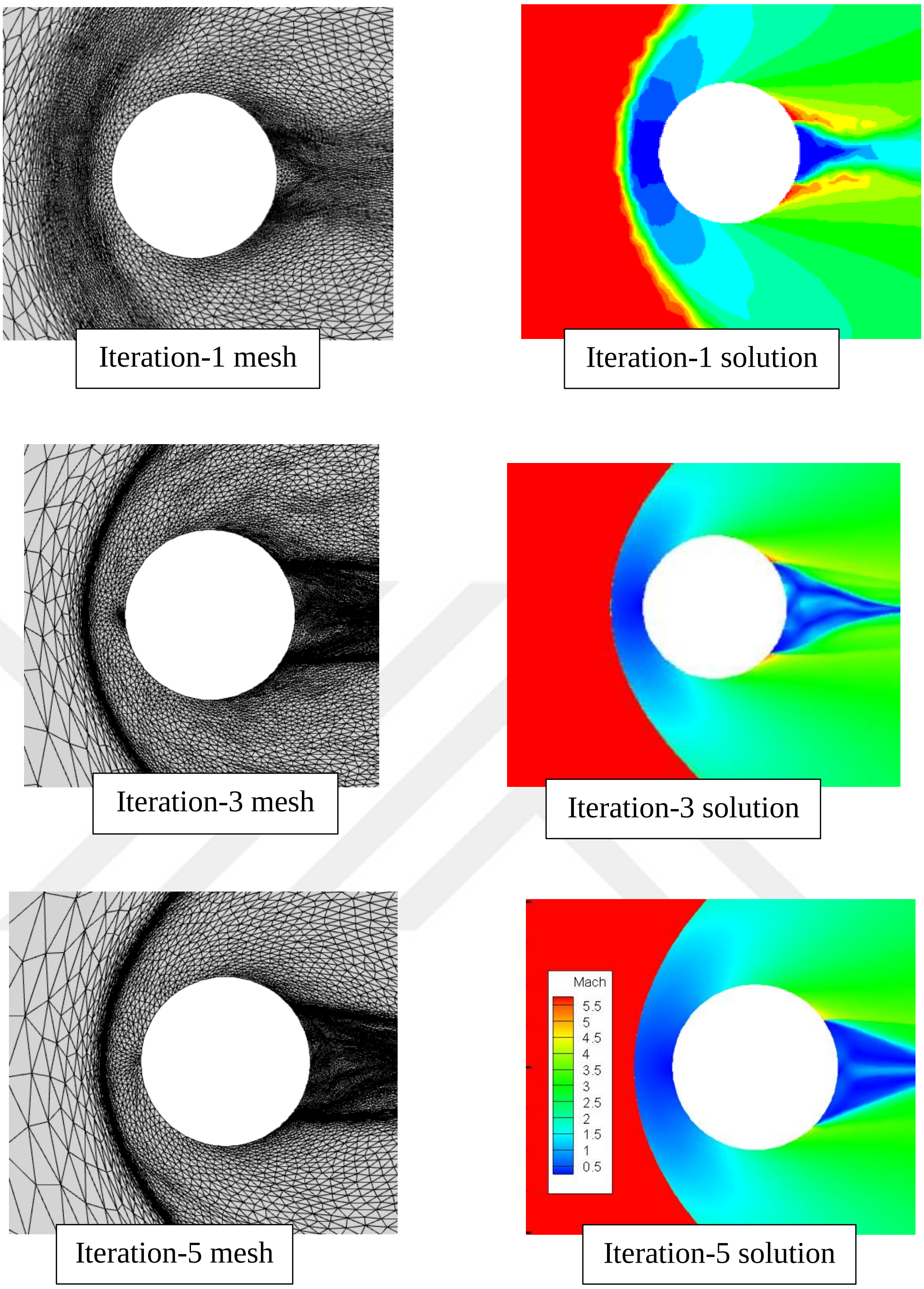
Iteration-1 mesh

Iteration-1 solution

Iteration-3 mesh

Iteration-3 solution

Iteration-5 mesh

Iteration-5 solution

Figure 4.8 : Refined meshes and corresponding Mach contour at different iteration level for inviscid flow over a cylinder at Mach 6.

The use of mesh adaption has significantly improved the solution of the inviscid perfect gas flow over a cylinder at Mach 6.

5. THE APOLLO REETRY CAPSULE

5.1 Background

Apollo AS-202 first successful flight was recorded on 25th August 1966. It was the first space flight to include navigation and guidance system. It was the success of the AS-202 mission that allowed the continuation Apollo program which resulted to the first manned Saturn IB and the Block I space vehicle orbital flight, AS-204. The Apollo capsule reentered the atmosphere at an approximate speed of 8,690 m/s. A skip reentry maneuver was performed by the reentry capsule by descending to an altitude of 67km and then lifting its way back to an approximate altitude of 81km. This particular maneuver was necessary to shed off some speed. After shedding a speed of 1,300m/s it then proceeds to descend, deploying its main parachute at an altitude of 7,250m. The capsule splashed down 380km away from the targeted landing location. As a result and approximate 8.5 hours had elapsed before the USS aircraft carrier could reach the location of the capsule [60,61]. Experimental analysis of the aerodynamic performance of the space capsule is detailed by [4]. While wind tunnel is generally considered as the undisputed tool for obtaining the necessary aerodynamic data to predict the performance and the motion in a spacecraft, it is highly expensive and utilizing computational fluid dynamics in simulating reentry conditions would provide reliable and economical supplement. The goal of this thesis is demonstrating how computational fluid dynamics simulation compared to experimental data in predicting the aerodynamic characteristics of Apollo AS-202 reentry capsule.

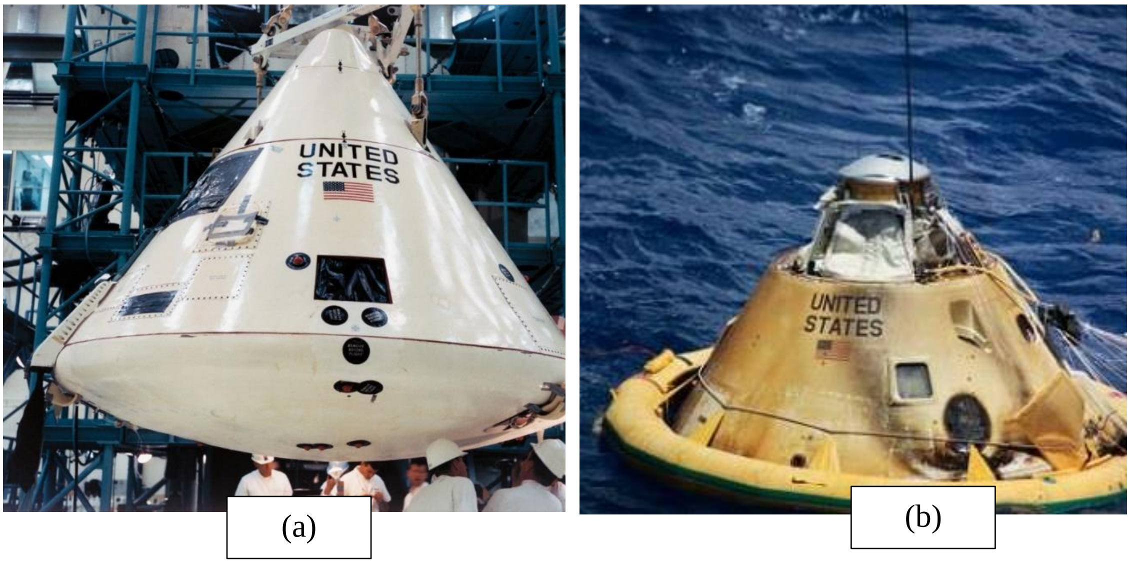

(a)

(b)

Figure 5.1 : Apollo AS-202 reentry capsule before flight (a) and after flight (b).

5.2 Flight Data Instrumentation

The flight data used for the validation of the flow characteristics of the Apollo AS-202 is recorded during the Apollo program. A total of twelve calorimeters and pressure transducers were placed on the forebody of the reentry capsule. Ten of the pressure transducers produced usable data, while none of the calorimeters produced any viable data [53]. On the afterbody of the command module, 23 calorimeters were placed. 19 of these functioned properly and produced reliable data. The precise location of the placed calorimeters on the afterbody of the AS-202 mission is shown in Figure 5.3. The coordinates of these location based on the defined coordinated system from Figure 5.3 is given on Table 5.1. A seen the picture, the angle θ is the circumferential orientation. With the assumption of zero sideslip, $\theta = 90^o$ lies along windward centerline which corresponds to the positive **z** axis. The distance from nose to the capsule apex is denoted by **x.** The leeward centerline corresponds to a circumferential angle $\theta = 270$. Figure 5.2 gives the detail information the calorimeters that recorded viable information/data during reentry phase.

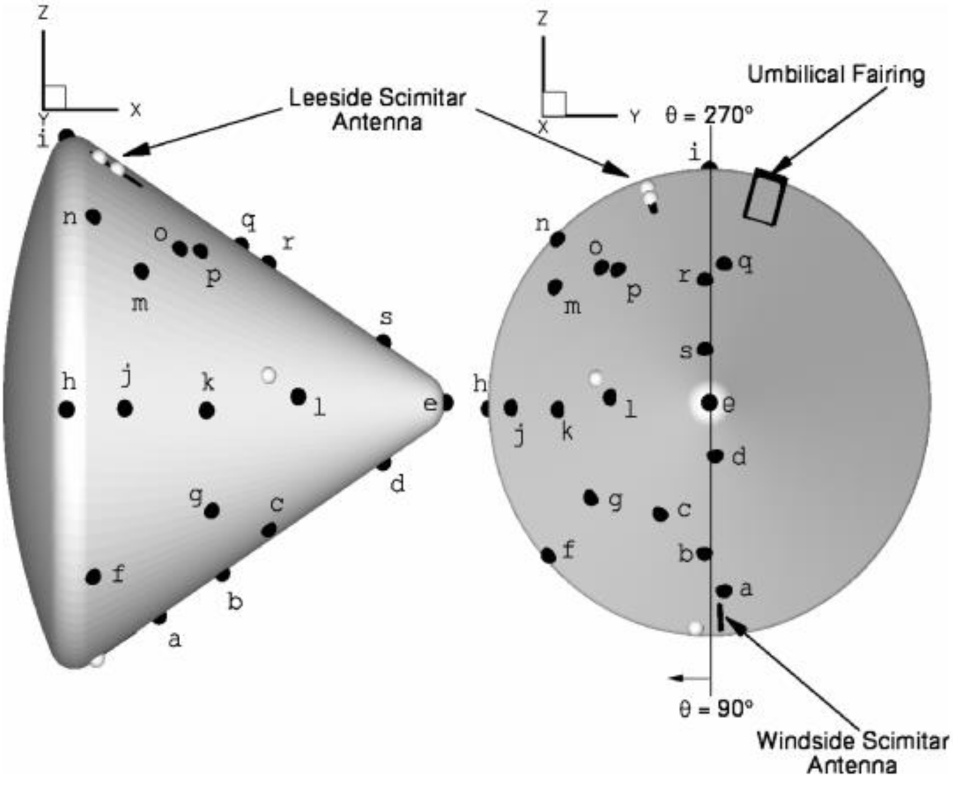

Figure 5.2 : Location of calorimeters on AS-202 CM afterbody. [54].

Table 5.1 : Afterbody calorimeters location for AS-202 CM [54].

$ID,^a$	$X,^b\ cm$	$\theta,^b\ deg$	Range W/cm^2
----	72.6	93.7	0-114
a	120.8	85.3	0-57
b	169.8	92.0	0-57
c	205.6	115.0	0-57
d	294.8	83.4	0-57
e	343.1	Apex	0-28
f	69.5	138.0	0-28
g	161.5	142.8	0-28
h	54.5	178.5	0-28
i	54.5	270.0	0-11.4
j	94.1	178.6	0-28
k	157.6	177.5	0-28
l	228.8	182.9	0-28
m	106.8	215.3	0-11.4
n	69.5	225.5	0-11.4
----	205.6	191.3	0-28
o	136.6	229.8	0-11.4
p	152.6	234.0	0-28
q	184.3	276.4	0-28
r	205.6	267.8	0-28
s	294.8	265.0	0-28
-----	74.1	253.0	0-28
------	88.0	253.0	0-57

5.3 Aerodynamic and Trajectory Reconstruction

Apollo AS-202 was the first space probe to include an onboard inertial measurement unit (IMU). This instrument permitted accurate reconstruction of trajectory points. The reconstruction of the atmospheric properties is based on sounding rocket technique [51]. The entry phase speeds, and flight regime were very developed and sufficient to span multiple flow regime. The flow properties spanned laminar, turbulent, non-equilibrium, reacting, nonreacting, minimal material response to strong pyrolysis injection. This range of conditions enabled a parametric investigation of the effects of turbulent transition and pyrolysis gas injection on turbulent heating levels [55]. Apollo capsule reentered the atmosphere at an approximate speed of 8.3km/s after 43900s from launch time. The flight path was narrow approximately -3.53^o and the effective reentry angle of attack was 18^o. As mentioned earlier AS-202 was the first Apollo probe to include an active guidance system. For this reason, a roll reversal or skip reentry was planned at 67km above sea level between 4410 to 4480s to align the capsule in a lift-up position and permit a lofting phase performance at the reentry flight. As observed from Figure 5.3 the skip phase was done after a local minimum altitude of was attained 4520s after launch time. The skip maneuvers lasted until 4690s when a local maximum was attained. The capsule continued to descent after a second roll reversal. The skipping maneuvers provided in two different heating pulses. However, as noticed from Figure 5.3, the nominal angle of attack was maintained with a tolerance of ±0.5°. However, the angle of attack gradual began to increase after 4900s, an approximate 20° was reached 5000s post launch. The space vehicle was not designed to exhibit any sideslip angle at the reentry phase but based on flight aerodynamics recorded, there was an indication that an approximately constant sideslip angle of about 2.5 ± 0.5 deg was present [51].

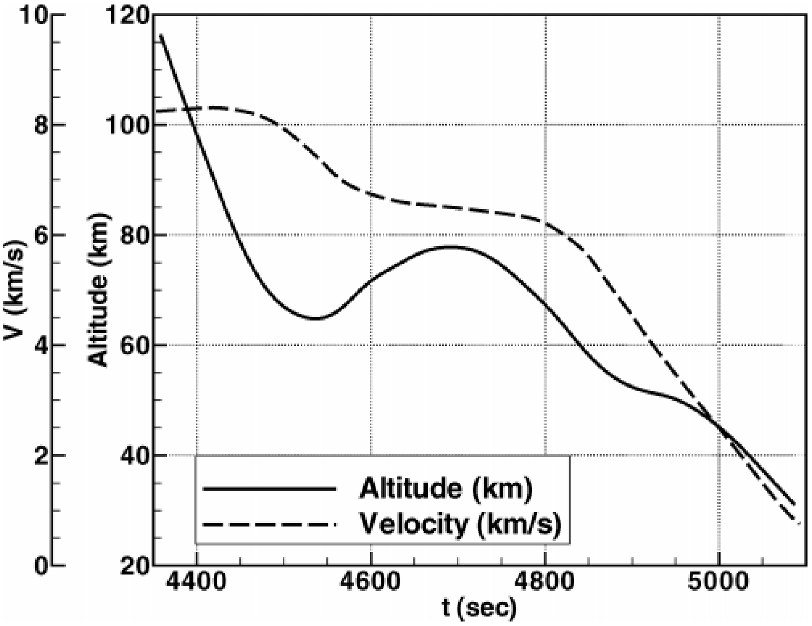

Figure 5.3 : Velocity and altitude as function of time from launch for AS-202 [54].

5.4 Geometric Modelling

The schematic of the command module is shown in Figure 5.4. The space capsule is designed with a blunt body to reduce the effects of tremendous aerodynamic heating. The designated reentry angle of attack is 25° with an offset center of gravity. The spherical section of the Apollo capsule has a curvature radius of 4.694*m*. The shoulder radius is ten percent of the body radius and has a value of 0.196. The afterbody has a conical section that makes a 33° with respect to a horizontal tangent at the shoulder. The aft of the capsule is blunted as well with a radius of 0.231*m*. The capsule has a maximum diameter of 3.912 and the axial dimension with TPS material included is 3.431*m* [54]. The capsule modelled in CAD is shown below.

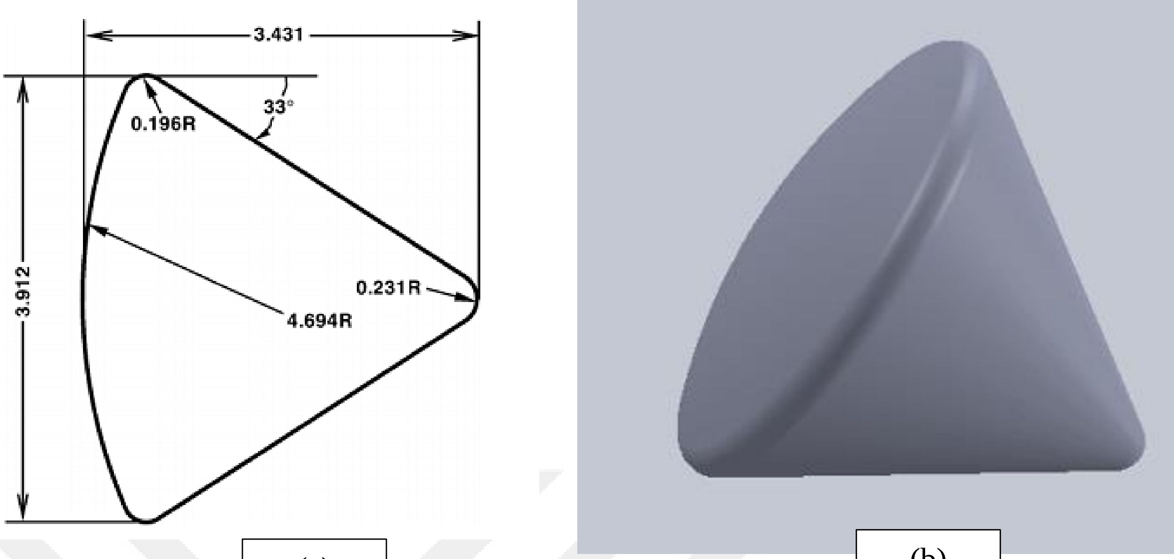

(a)

(b)

Figure 5.4 : Apollo AS-202 Capsule schematic (a) and the CAD module (b).

5.5 Meshing

In section 4.1 the advantages of unstructured meshes was explained. Their points are irregularly placed, and this allow the shape of the elements to vary and for the geometry to be meshed with ease. Besides the ease of mesh generation using unstructured techniques, it also gives a room for solution-based mesh adaptation. Due to these proprieties, and the anisotropy nature of the flow region around a reentry capsule, an unstructured mesh is used for both 2D and 3D simulations. For the two-dimensional simulation, the computational domain is a circle with the capsule at its center. The radius of the circle is about 100*D*, where *D* is the maximum diameter of the Apollo AS-202 capsule. The domain is extended to capture accurately the flow conditions with no interactional effect of the boundary condition. The initial mesh is a circular with 26,192 unstructured triangular elements and 13,336 points. The mesh is refined near the surface of the capsule to accurately resolve the boundary layer for initial solution which would be used for the anisotropic mesh adaptation. The far-field boundary conditions imposed at the circumference of the circle and the no-slip slip boundary condition is applied on the surface of the capsule.

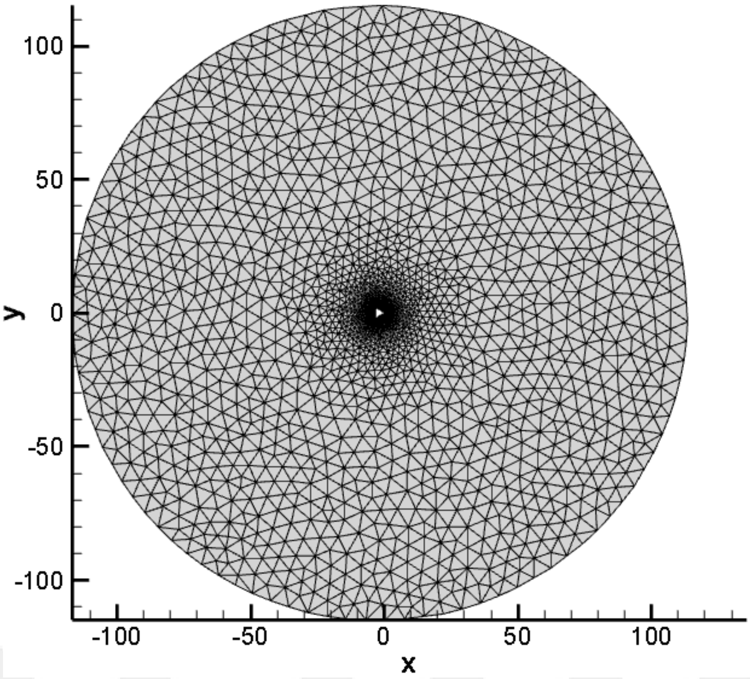

Figure 5.5 : Computational domain for 2-D simulation**.**

For the 3-D mesh, the computational domain is a sphere with a radius of 50*R* and the reentry capsule at the center. The initial mesh has boundary layer with *y*+ of 1 and 61 full anisotropic tetrahedral boundary layers generated using pointwise. The initial mesh has 554,321 points and 3,304,780 tetrahedral cells. Figure 5.6 shows the domain for the three-dimensional simulation.

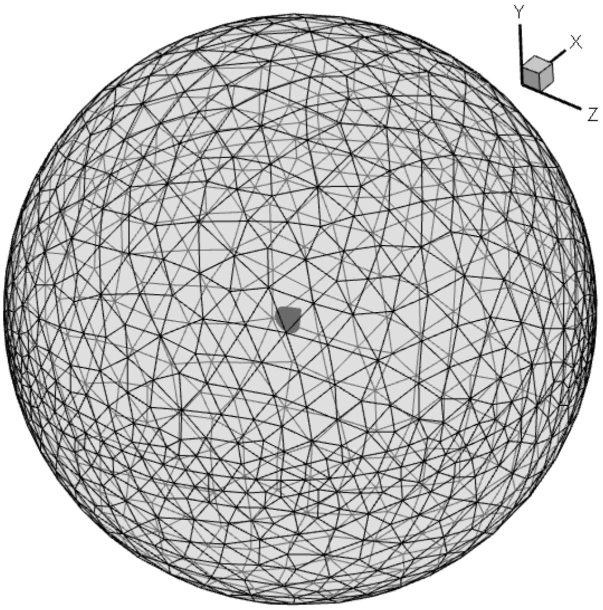

Figure 5.6 : Computational domain for **3**-D simulation**.**

6. SIMULATION OF FLOW AROUND APOLLO REENTRY CAPSULE

6.1 Background

Aerodynamic characteristic of a blunt capsule is important in terms of planning trajectory points and thermal protection system. Aerodynamic performance is evaluated in terms of lift to drag ratio (L/D) and trim angle of attack. The preflight wind tunnel testing of the Apollo AS-202 reentry capsule established a constant aerodynamics coefficients and trim angle of attack above Mach 10 [56]. However, this prediction did not correlate with the flight recorded data where a significant variation in trim angle of attack and decrease in lift to drag ratio. Several experiments were performed to understand these anomalies and inconsistency of the data. A postflight wind tunnel testing was done to resolve the problem[4]. The goal of this chapter is to use computational fluid dynamics to simulate the flow conditions and compare the results with experimental data from the postflight analysis.

6.2 Apollo Entry Aerodynamics

The motion of aerial vehicle is characterized by its propulsive forces, inertial forces, the forces of gravity, and the aerodynamic forces. The Aerodynamic forces are particularly important by the fact that the space capsule is designed to employ low lift to drag ratio (L/D) for a controlled into the atmosphere [4]. Wind tunnels are regarded as on the of most powerfully tools in simulating the aerodynamics data needed to fully understand the behavior of the space vehicles. A series of wind tunnel test were conducted between the period of December 1966 to May 1967 by the ARO inc. contract operator of Arnold engineering Development Center (AEDC), AFSC, Arnold Air force station, Tennessee. The test was an exclusive wind tunnel analysis of the Apollo AS-202 capsule to resolve the anomalies of the preflight data and the post flight data [4]. As explained earlier, wind tunnel testing of hypersonic flows is expensive and difficult. CFD is an economical option to investigate these flows. However, there is a great need to validate the CFD codes and solution methodology with available experimental data. The purpose of the present study is stimulating these wind tunnel conditions with a CFD solver (SU2) and compare the results to access the accuracy of the solver in predicting the aerodynamic characteristics of the space capsule in terms of lift to drag ratio (L/D).

6.3 Geometry Information of Experimental Models

The wind tunnel testing uses a number of constructed models. The model size based on heatshield diameter ranges from 0.0155*m* to 0.2035*m*. For Tunnels A, B, C and L, the actual vehicle as flown is simulated in model construction. The geometry details of the model used in the wind tunnel are given in the Figure 6.1.

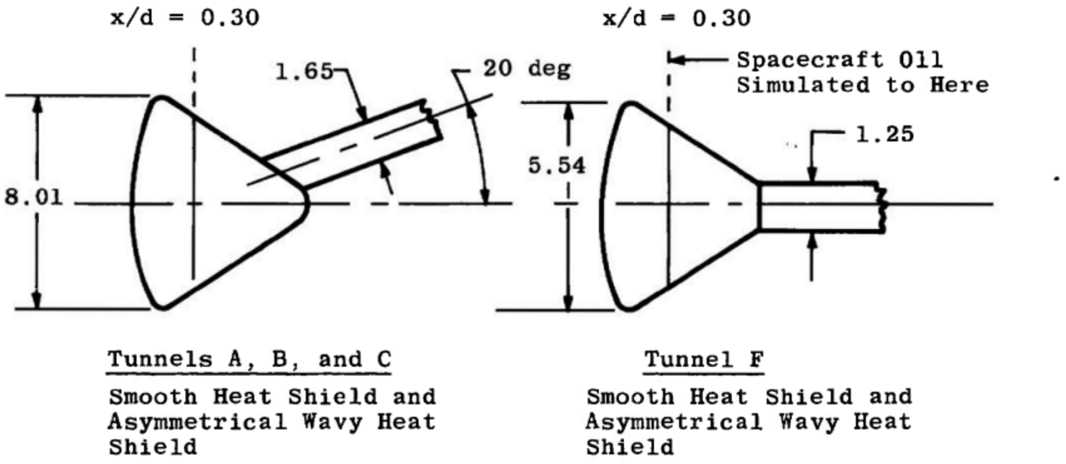

Figure 6.1 : Constructed model used in tunnels A, B, and C**.**

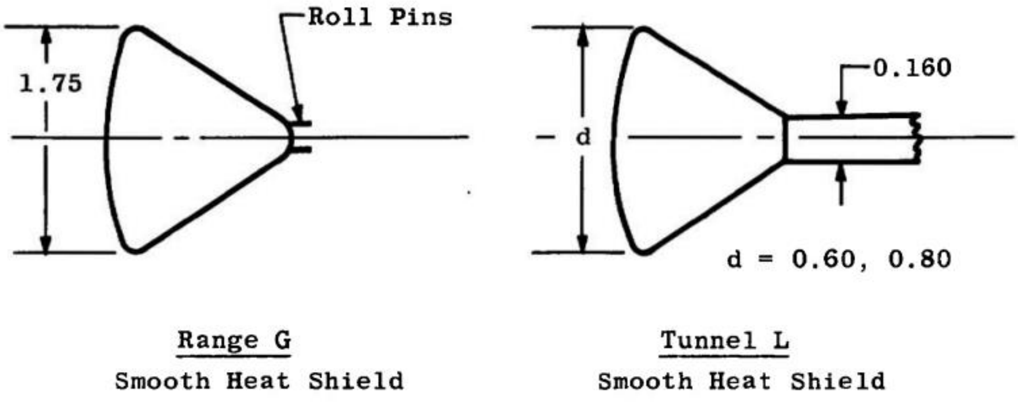

Figure 6.2 : Constructed model used in tunnels G and L

In is important to note that these shapes are based on Apollo AS-202 before the atmospheric reentry. The shape changes due the massive aerodynamic heating were not simulated.

Table 6.1 : The selected freestream conditions for numerical simulations.

Simulation ID	Temperature (K)	Mach number	Freestream Reynolds number based on capsule diameter
A	310	3	1.67×10^7
B	730	8	6.96×10^6
C	1270	12	1.43×10^7
L	1660	10.15	4.48×10^5

The freestream conditions for simulation defined in Table 6.1 is with respect wind tunnel conditions to be used for verification. The Simulation ID in table correspond to the with tunnel identity in [4].

6.4 Computational Simulation of Selected Wind Tunnels

The physical case description of the 3D simulation is as flows; Compressible Navier-Stokes's equation is solved with Spalart-Allmaras model of turbulence. The simulation is normalized with freestream velocity equals Mach number for simplicity as our interest is accurately capturing the shock regions and other physical phenomenon and at the same compute the non-dimensional lift and drag coefficients. Roe, and AUSM, fluxes are tested to compare their accuracy for the hypersonic flow. A constant Courant-Friedrichs-Lewy number (CFL) of 1 is used for the simulations. It is observed that the simulation diverged for a high CFL number. The simulation is for various angle of attacks, Mach and Reynold's number and the fluid medium is assumed to be perfect gas. Green-Gauss theorem is used for gradient computation. For the time integration, Euler implicit method is used for the numerical integration, FGMRES is used for solving the linear system with ILU preconditioner. The convergence criterion for the linear solver is 1.0×10^{-10} based on the residual of the continuity equation.

6.5 CFD Simulation of Tunnel (A) Freestream Conditions

The goal of these chapter is to obtain the result of the CFD simulations and compare with the experimental data from Apollo wind tunnel program conducted in Tunnel A at period of 18 May 1967. The data of the test at this tunnel was necessary to better investigate and study the Mach number effect on the capsule aerodynamics. The simulation conditions for the tunnel testing are defined on Table 6.1. The chosen freestream Mach number for the computational simulation is Mach 3, the Reynolds number based on the capsule diameter is 1.67 x 10^7. The fluid model is ideal gas, and the governing equations were Reynolds averaged Navier-Stokes equation with Spallart-Allmaras (SA) turbulence model. The computational domain was a spere with the capsule at the center and the far-field at about 25 times the capsule maximum diameter. This is to ensure the result is not affected by a tight boundary (far-field) and the flow is allowed to develop fully. Figure 6.3 and 6.4 shows the comparison of aerodynamic lift and drag force coefficients compared between the simulation and the experiments.

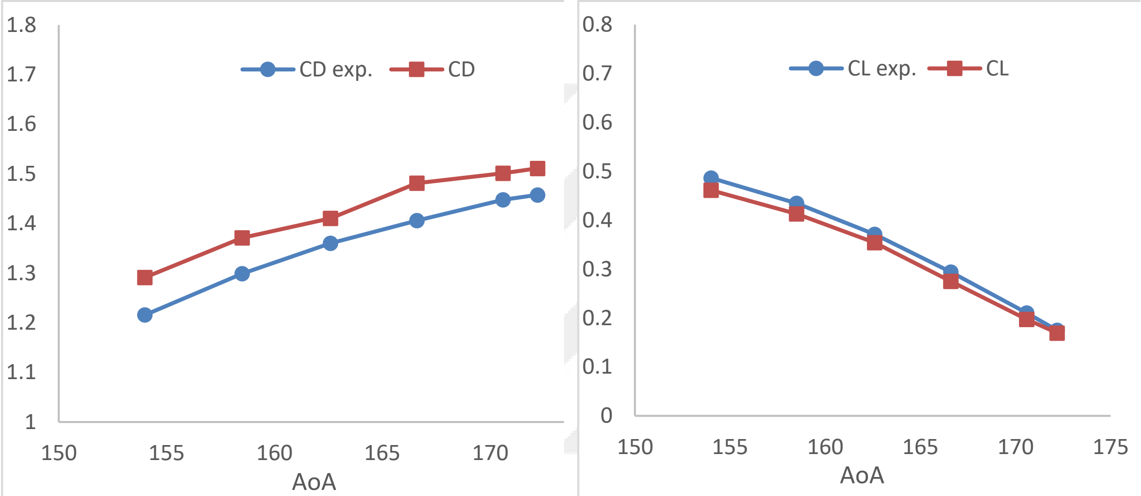

(a)

(b)

Figure 6.3 : Comparison of lift (CL) and drag (CD) force coefficient of Apollo reentry capsule at Mach = 2.98 in present simulation vs experimental data.

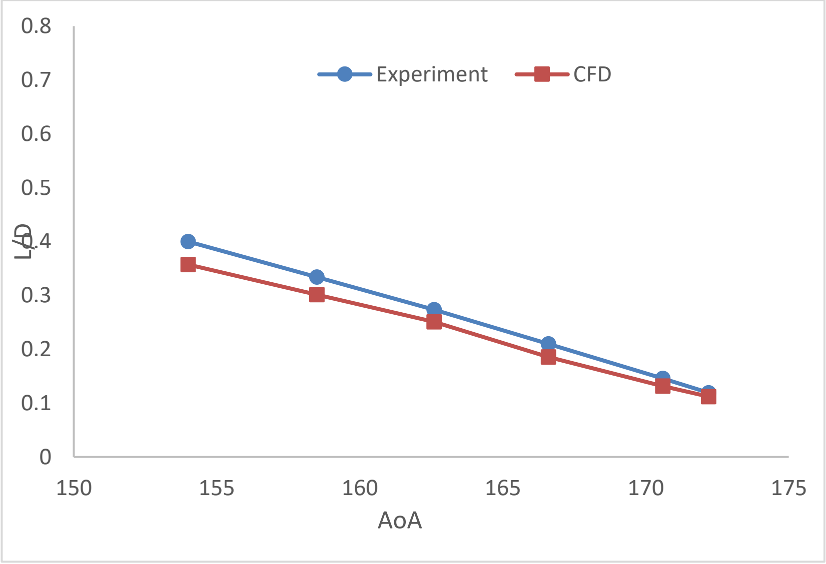

Figure 6.4 : Comparison of Aerodynamic efficiency (L/D) of Apollo reentry capsule at Mach = 2.98 in present simulation vs experimental data.

Table 6.2 : Aerodynamic coefficients of Apollo reentry capsule at Mach = 2.98.

Angle of Attack	CD experiment	CL experiment	CL/CD experiment	CD simulation	CL simulation	CL/CD simulation
154	1.215777	0.486498	0.400154	1.2914	0.4614	0.35728667
158.5	1.299199	0.434384	0.334347	1.3712	0.4132	0.30134189
162.6	1.360314	0.370965	0.272705	1.4105	0.3541	0.25104573
166.6	1.40606	0.294365	0.209355	1.4812	0.2751	0.18572779
170.6	1.448092	0.210335	0.14525	1.5014	0.1971	0.13127747
172.2	1.45777	0.174759	0.119881	1.5112	0.16938	0.11208311

The results (Table 6.2) showed a fair agreement between current study and the experimental data. The simulation is normalized in SU2 with the freestream velocity equals Mach number within the SU2 environment. The refence length for Reynolds number is the capsule diameter. The flow field contour in the simulation at various angle of attack is shown in Figure 6.5 to Figure 6.9 and are explained.

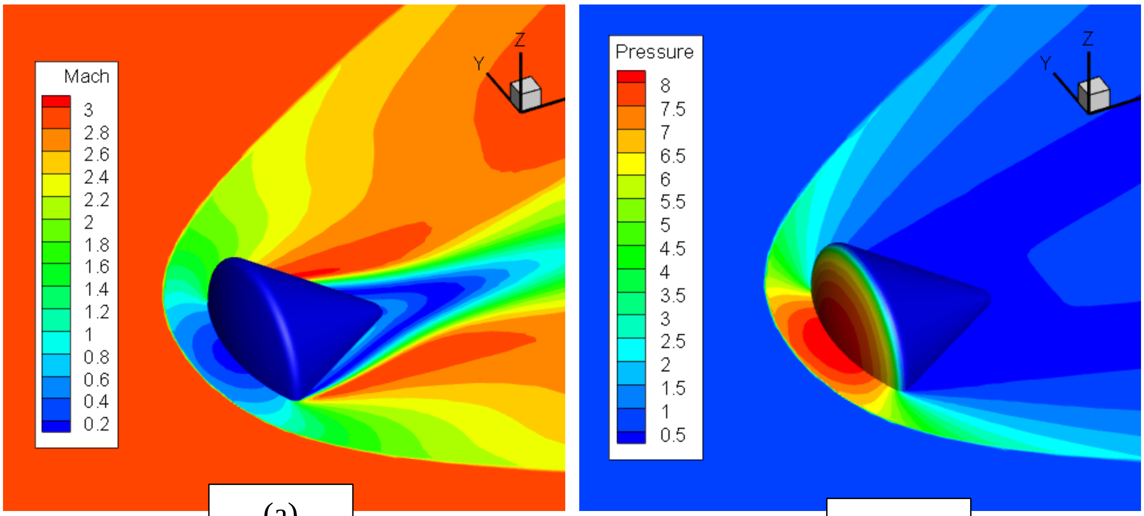

(a)

(b)

Figure 6.5 : The Mach number (a) and pressure (b) contour distributions around Apollo AS-202 reentry capsule at Mach = 2.98, angle of flow = 0°.

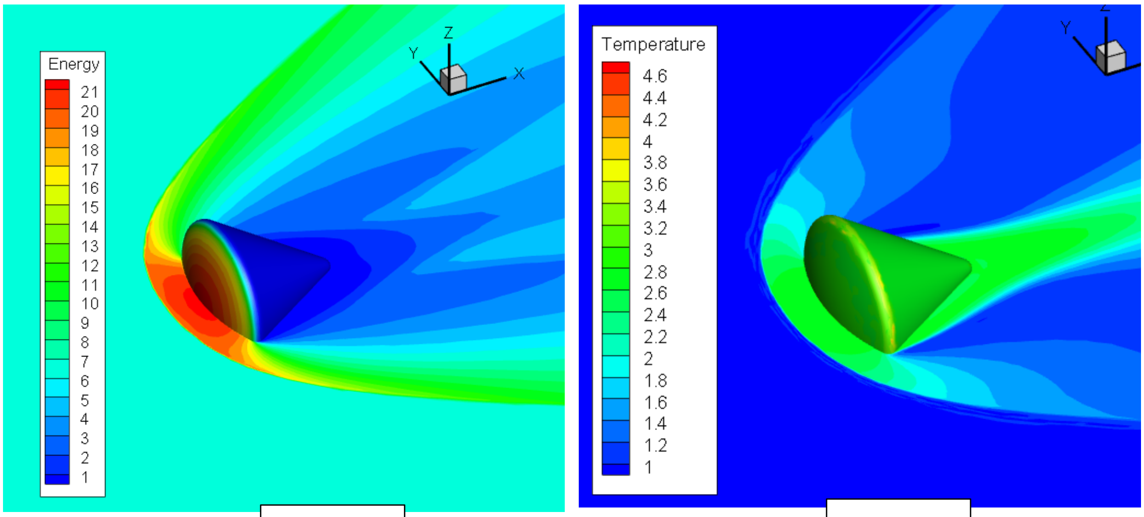

(a) (b)

Figure 6.6 : The energy (a) and temperature (b) contour distributions around Apollo AS-202 reentry capsule at Mach = 2.98, angle of flow = 0^o.

The Results in Figure 6.5 and 6.6 are normalized based on freestream velocity equals Mach number and the pressure is 1/gamma, (the ration of specific heat). The fluid model is assumed to be perfect gas, and hence the temperature contour shown in Figure 6.6 is an estimate based on the ideal gas assumption. The contour plot is as expected based the physical nature of the flow. However, for a more accurate prediction of the temperature contour chemical reaction and thermal non-equilibrium need to be taken in to account. In present study only non-reacting Reynold's averaged Navier-Stoke's equation with the Spalart-Allmaras one-equation turbulence model was solved. Figure 6.7 to 6.9 show the result of simulation for conditions at lower angle of attacks.

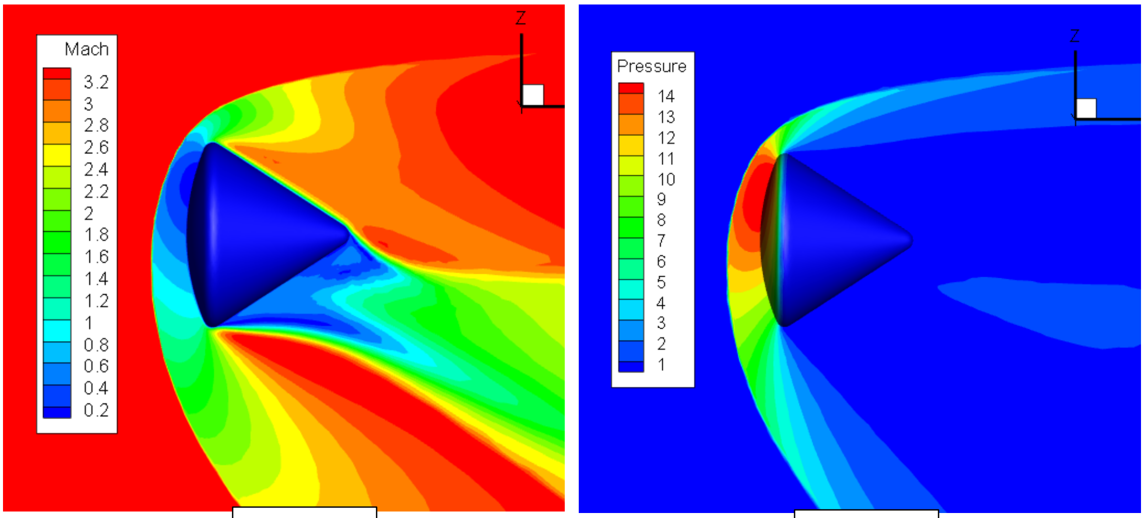

(a) (b)

Figure 6.7 : The Mach number (a) and pressure contour (b) distributions around Apollo AS-202 reentry capsule at Mach = 2.98, Angle of flow = -20^o.

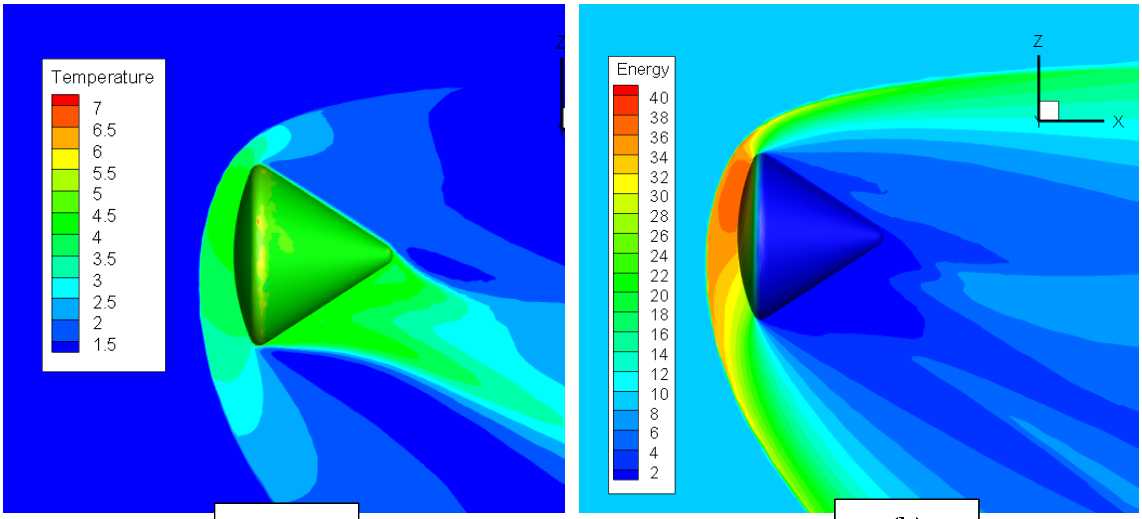

(a) (b)

Figure 6.8 : The Temperature (a) and Energy (b) contour distributions around Apollo AS-202 reentry capsule at Mach = 2.98, angle of flow = -20^o.

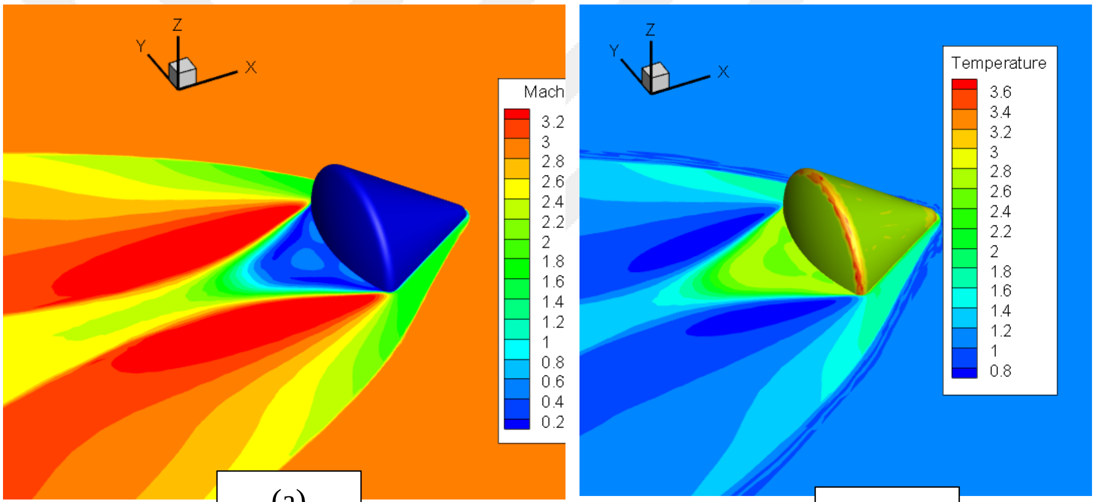

(a) (b)

Figure 6.9 : The Mach (a) and temperature(b) contour distributions around Apollo AS-202 reentry capsule at Mach = 2.98, angle of flow = -170^o.

The contour plot shown in Figure 6.7 to Figure 6.10 shows the nature of the flow field around Apollo AS-202 reentry capsule where the values in the figures are normalized.

6.6 CFD Simulation of Tunnel (B) Freestream Conditions

The conditions to be studied next are the freestream conditions for the experimental conducted in tunnel B. The goal is the show how CFD can be used as a complement to the established but expensive wind tunnel testing. Hence, to that end various freestream conditions need to be tested. The experiment in tunnel was designed to investigate the viscous effect of the capsule was done in tunnel B on January 17 1967. This is experiment is taken as reference for the validation of present study. The simulation Reynolds number is for this study is 6.96x10^{6} and the free stream Mach number is 8.0. The aerodynamic force coefficients were calculated for angle of attack rage of 0 to 170. The comparison of the aerodynamic forces between the experiment and CFD simulation is shown in Figure 6.10. The importance of these simulation is to understand the viscous effect on aerodynamic force coefficients.

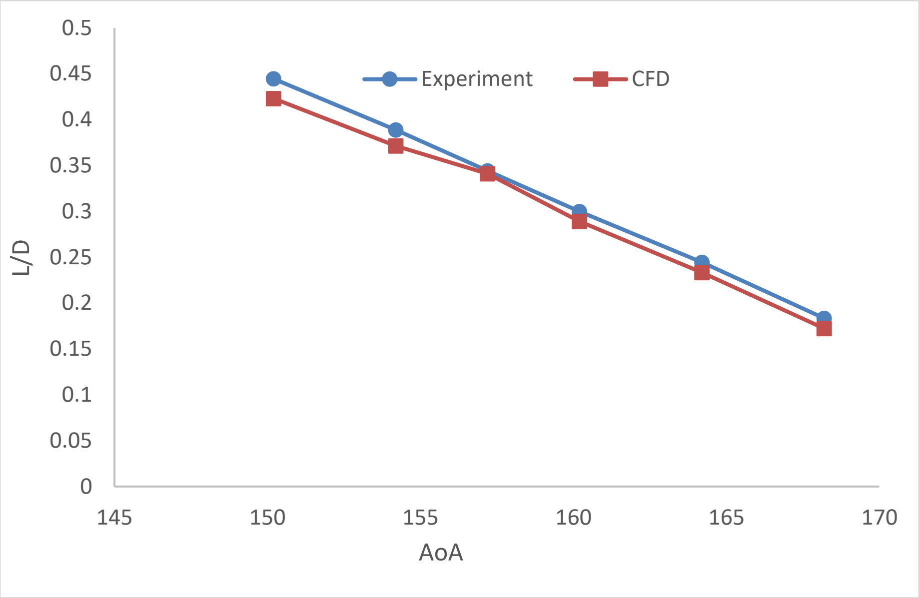

Figure 6.10: Comparison of Aerodynamic efficiency (L/D) of Apollo reentry capsule at Mach = 8.0 in present simulation vs experimental data.

Table 6.3 : Aerodynamic coefficients of Apollo reentry capsule at Mach = 8.0

AoA	Experiment (CL/CD)	CFD (CL/CD)
150.2	0.4445	0.4231
154.2	0.3888	0.3712
157.2	0.344	0.341
160.2	0.3	0.2891
164.2	0.2443	0.2333
168.2	0.1834	0.1723

The simulation was initiated to solve RANS with SA model around the Apollo AS-202 reentry capsule at Mach number of 8.0 and Reynolds number of 6.96x10^{6} based on true model maximum diameter of 3.912*m*. The CFD aerodynamic performance coefficient agrees with the experimental data nicely as seen in Figure 6.10 and Table 6.2. The validation comparison was done for a varying angle of attack between 150 to 170. The convergence of the simulation depends on the quality of the initial mesh. The mesh is refined especially new the boundary layer with tetrahedral anisotropic elements using pointwise, and the pointwise calculate at their website to calculate of y+. The nature of the flow field contour is shown in Figure 6.12 to Figure 14.

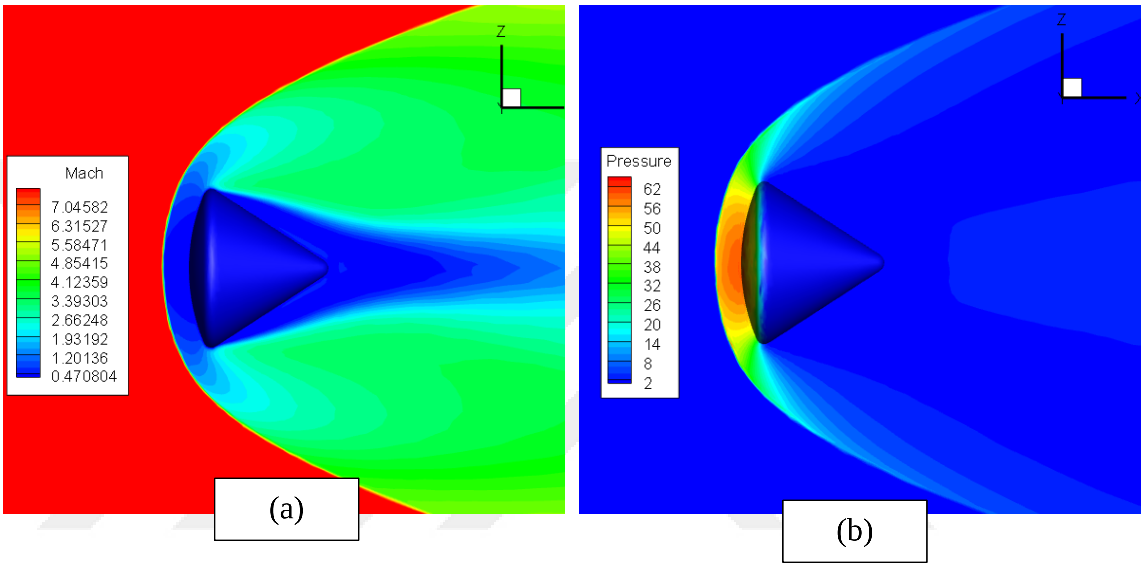

(a)

(b)

Figure 6.11 : The Mach number(a) and pressure(b) contour distributions around Apollo AS-202 reentry capsule at Mach = 8.0, Angle of flow = 0°.

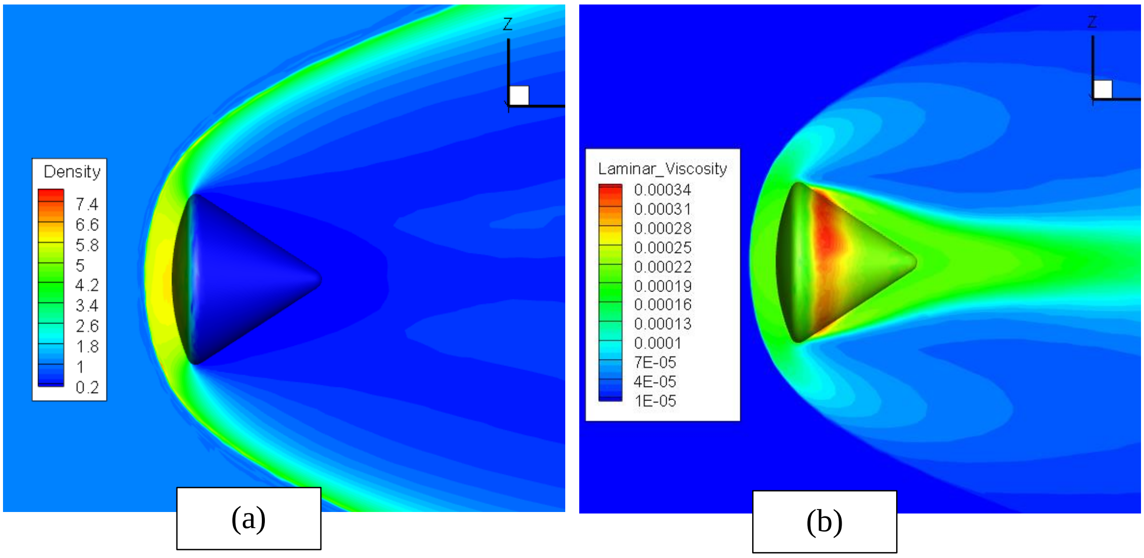

(a)

(b)

Figure 6.12 : The density (a) and laminar viscosity (b) distributions around Apollo AS-202 reentry capsule at Mach = 8.0, angle of flow = 0**°.**

The flow field obtained in these simulations also agrees with the physics of the as it well further analyzed in the next section. As the contour plot distribution in Figure

6.11 and 6.11 is done by taken a volume slice in the pitch plane (*y*-plane). Both AUSM and Roe methods of convective flux evaluations were tested. The results were similar. The graphs in Figure 6.13 and 6.14 are the contour plot at Mach 8.0 and angle of attack equals to zero obtained using ROE convective flux methods.

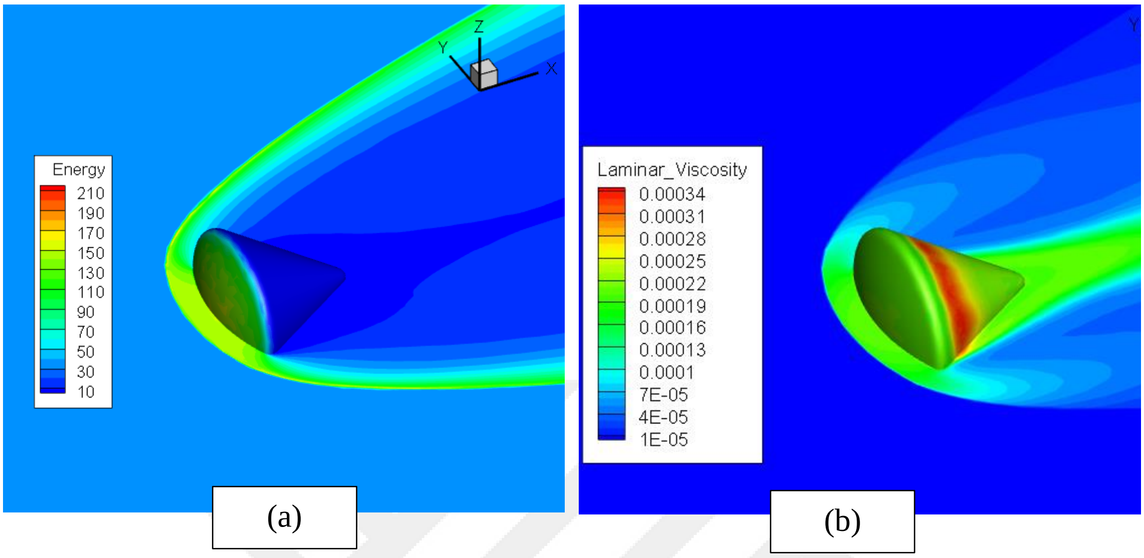

Figure 6.13 : Energy (a) and laminar viscosity (b) contour distributions Around Apollo AS-202 Reentry capsule at Mach = 8.0, Angle of flow = 0**º.**

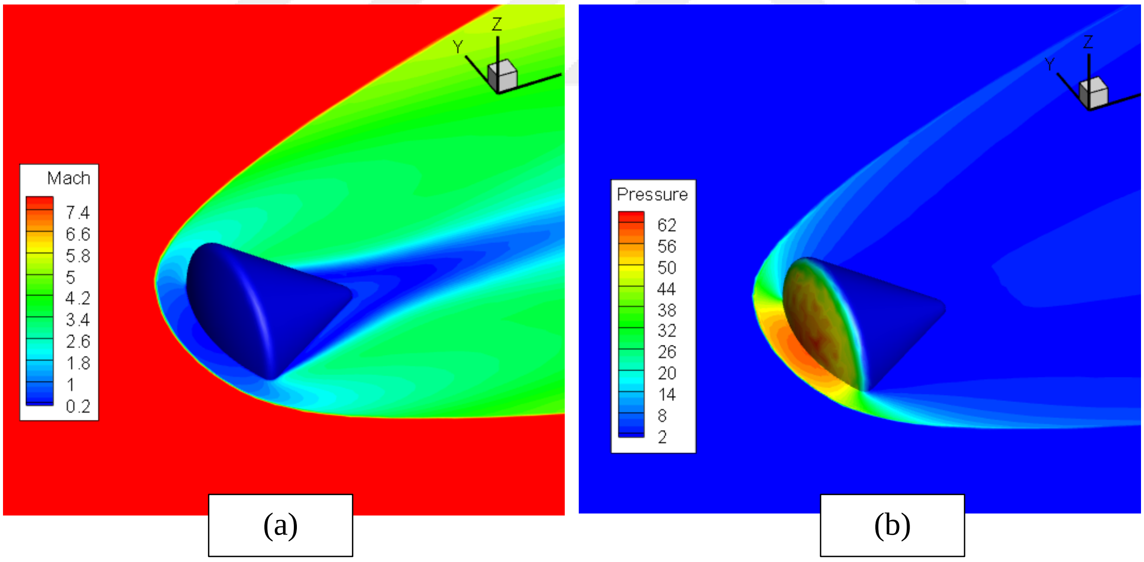

Figure 6.14 : The Mach number (a) and pressure (b) contour distributions Around Apollo AS-202 Reentry capsule at Mach = 8.0, Angle of flow = 0**º.**

For the results in Figure 6.13 and 6.14, a slice is taken in the *z*-plane and AUSM flux method was used for the same condition of Mach, Reynolds, number and flow angle. The CFD simulation for the conditions in tunnel B was a bit challenging as the Mach number is higher than in various simulation. The weighted least square method for convective flux evaluation kept diverging, by reducing the CFL to value of 2 and changing to convective flux evaluation to Green-Gauss, better results were obtained.

6.7 CFD Simulation of Tunnel (C) Freestream Conditions

The next simulation for the CFD validation to compare the results based on the freestream conditions in Tunnel C. The simulation in the original experiment is similar to the test in Tunnel A, but at higher Mach number of 12.0. The experiment in tunnel was designed to investigate the viscous effect on the capsule was done in May 26, 1967. This is experiment is taken as reference for the validation of present study. The simulation Reynolds number is for this study is $1.43x10^7$ and the free stream Mach number is 12.0. The aerodynamic force coefficients were calculated at various angle of attacks, with the experiment values taken as reference. The comparison of the aerodynamic forces between the experiment and CFD simulation is shown in Figure 6.15 and Table 6.2. These data are needed in order the established fully the effect of Mach number on aerodynamic force and moment coefficient of the reentry capsule.

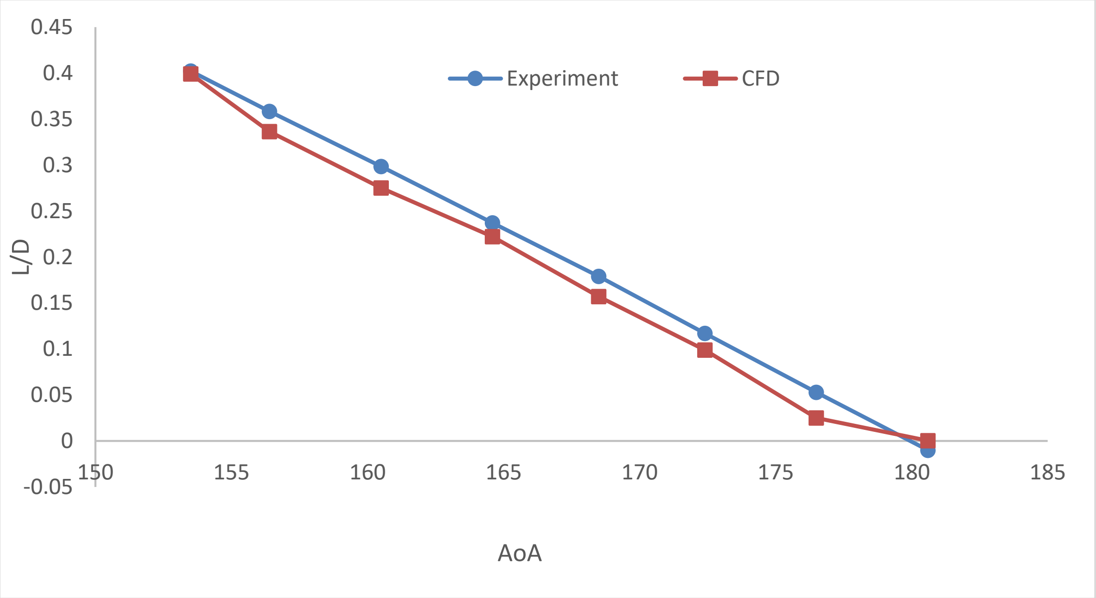

Figure 6.15: Comparison of Aerodynamic efficiency (L/D) of Apollo Reentry Capsule at Mach = 12.0 in present simulation vs experimental data.

The comparison of the aerodynamic coefficient in present study and the experimental (Figure 6.15 and Table 6.4) shown a fair agreement of these values. The high Mach for this simulation makes it challenging to obtained good results. However, after effort was made to create good initial mesh, low CFL of 1 and Green-Gauss method for convective flux, good results were obtained

Table 6.4 : Aerodynamic coefficients of Apollo reentry capsule at Mach = 12.0

AoA	Experiment (CL/CD)	CFD (CL/CD)
153.5	0.4022	0.3991
156.4	0.3584	0.33641
160.5	0.2986	0.27512
164.6	0.2371	0.2221
168.5	0.179	0.1569
172.4	0.1169	0.09895
176.5	0.0528	0.025
180.6	-0.01	0.0003

The simulation at this condition has the highest Mach number simulated in the thesis. The simulation Mach number is 12.0. The flow field is completely hypersonic, and there will be chemical reaction playing a vital role. However, as stated earlier no reaction is considered in the thesis and all simulation are based on ideal gas assumption. The simulation was challenging as the SU2 kept diverging on the basis on the solution contained on physical points in the upwind solutions. After many efforts, and improving the quality of the mesh to capture the initial condition before adaptation, good results were obtained. However, the temperature dependent parameters would not be accurate quite accurate due to ideal gas assumption. As it can be seen from the validation (Figure 6.15), the flow physics remained unchanged. It is worth to mention that in the experiment by the ARO inc. contract operator of Arnold engineering Development Center (AEDC), which was taken as reference, real gas was not simulated and the experiment agrees nicely with the Apollo full-scale flight data were real gas was the fluid model. The authors B. J. Griffith and D. E. Boylan, concluded that real gas effect is in significant on the force and stability coefficient up to 27,000 ft/s (8,230 m/s) [4].

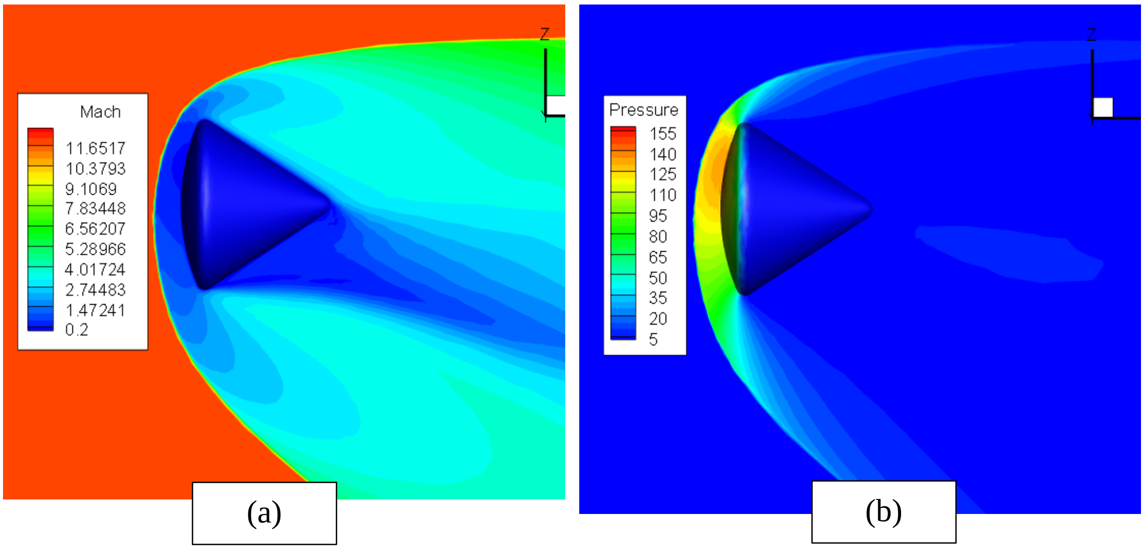

(a) (b)

Figure 6.16 : The Mach (a) and pressure (b) contour distributions Around Apollo AS-202 Reentry capsule at Mach = 12.0, Angle of flow = -15º.

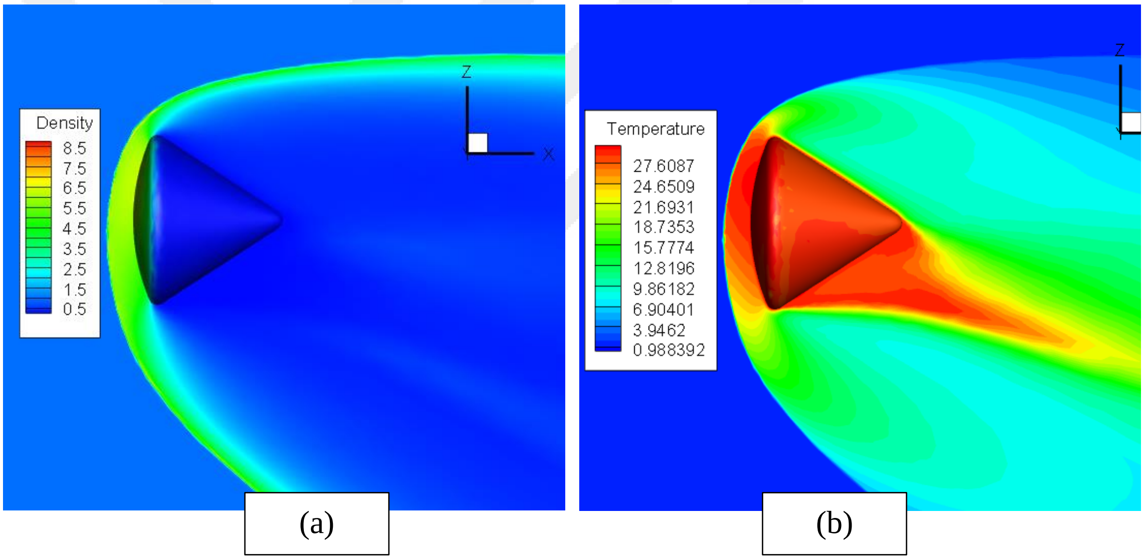

(a) (b)

Figure 6.17 : The Density (a) and Temperature (b) distributions Around Apollo AS-202 Reentry capsule at Mach = 12.0, Angle of flow = -15º.

The contour plot shown in Figure 6.16 and Figure 6.17 shows the nature of the flow field around Apollo AS-202 reentry capsule. The values in the Figures are normalized, the temperature is not as expected due to the fact the no chemical reaction was taken into account during the simulation or any thermal no equilibrium. However, the nature of the flow field agrees with the physics of the problem.

6.8 CFD Simulation of Tunnel (L) Freestream Conditions

The investigation of viscous effect at high simulated altitude was carried out in wind tunnel L between the period of 5th December 1996 to January 9th 1967. This is test of interest and is taken as the final reference for the computational simulation validation. Due to time factor, only a single angle of attack of 155 is simulated using CFD. The simulation Reynolds number is for this case is 4.48×10^5 based on the full-scale model diameter and the free stream Mach number is 10.15.

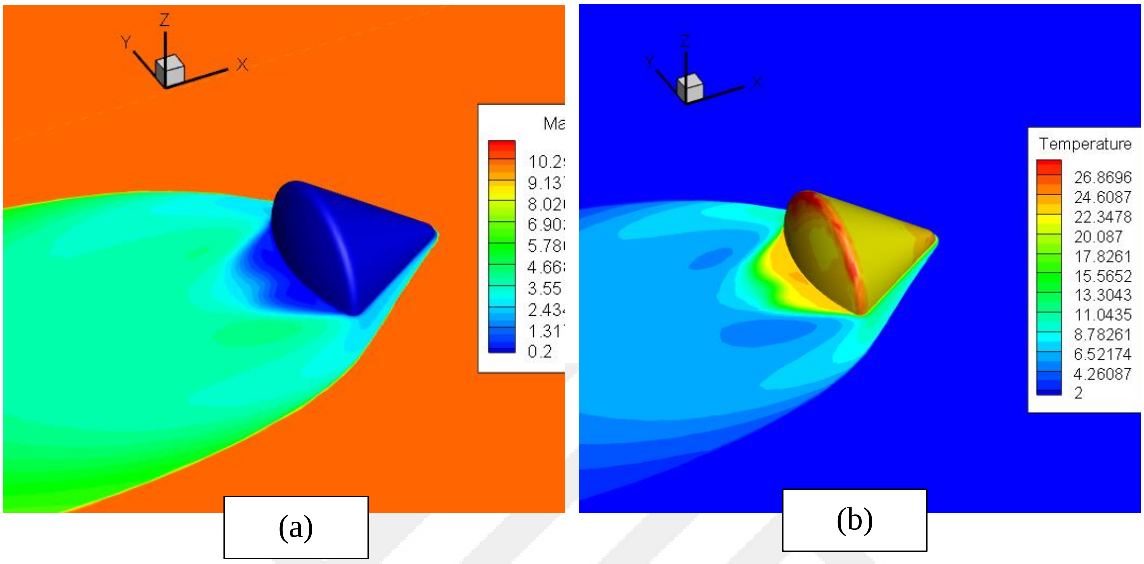

(a)

(b)

Figure 6.18 : The Mach (a) and Temperature (b)contour distributions Around Apollo AS-202 Reentry capsule at Mach = 10.15, Angle of flow = -155°.

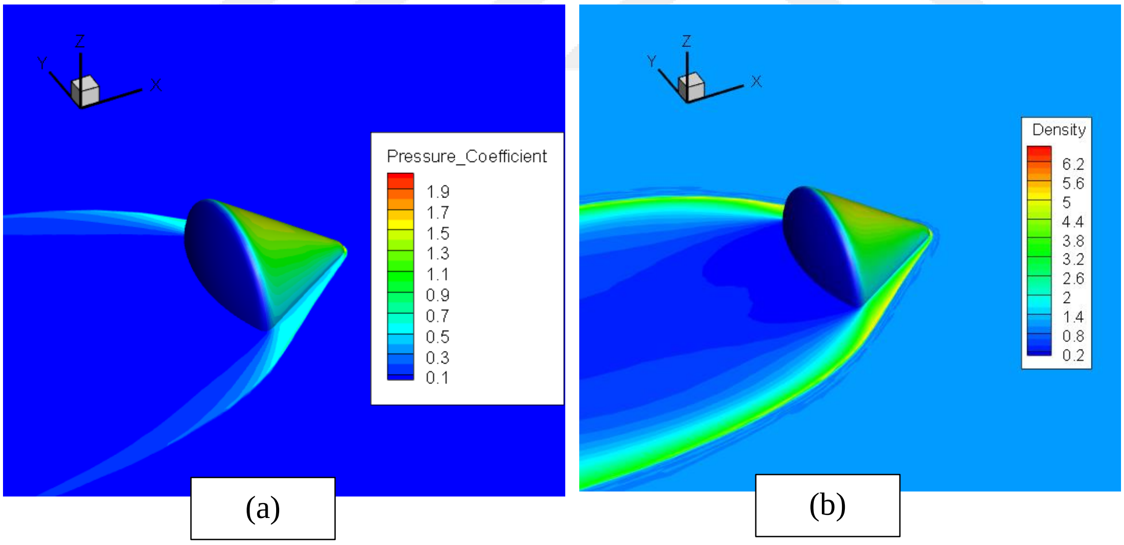

(a)

(b)

Figure 6.19 : Pressure coefficient (a) density (b) contour distributions Around Apollo AS-202 Reentry capsule at = 10.15, Angle of flow = -155**°.**

The contour plot shown in Figure 6.18 and Figure 6.19 shows the nature of the flow field around Apollo AS-202 reentry capsule. Physical Description of Flow Field Around Apollo Reentry Capsule is explained as follows;

At the reentry phase, a strong detached shockwave is observed in front of the reentry capsule. The region afterward the shockwave, a shock layer characterized with high enthalpy and temperature is observed once again, resulting in a severe heating environment around the capsule. The characteristics of the flow filed around reentry capsule include earth’s orbital re-entry speed nearly twenty-five Mach number, temperature of the flow typically high to the extent where the covalent chemical bonds of the air and diatomic molecules are broken. The broken molecules particles produced electrically charged plasma around the space vehicles, reentry occurs at many kilometers above sea level and thus the air density is very low. A bow shock formed ahead of the vehicle slows down the hypersonic flow. In re-entry phase, the thermal loads play a major part [5]. As capsules fly from subsonic Mach < 1, to hypersonic flow remarkable physical changes take place in the flow: a shock wave is generated by the surface of the object and physical properties are altered instantly across the shock because of intense compressibility. This is different from those of subsonic and supersonic regions, in a hypersonic regime, nondimensional variables such as lift, drag and pressure coefficient, and flow field structure become Mach number independent. This is the idea behind the Mach number independence hypothesis for hypersonic flow [6]. Figure 6.20 shows a typical flow field where the windward free shear layer can be seen to curve around and reattach on the conical frustum.

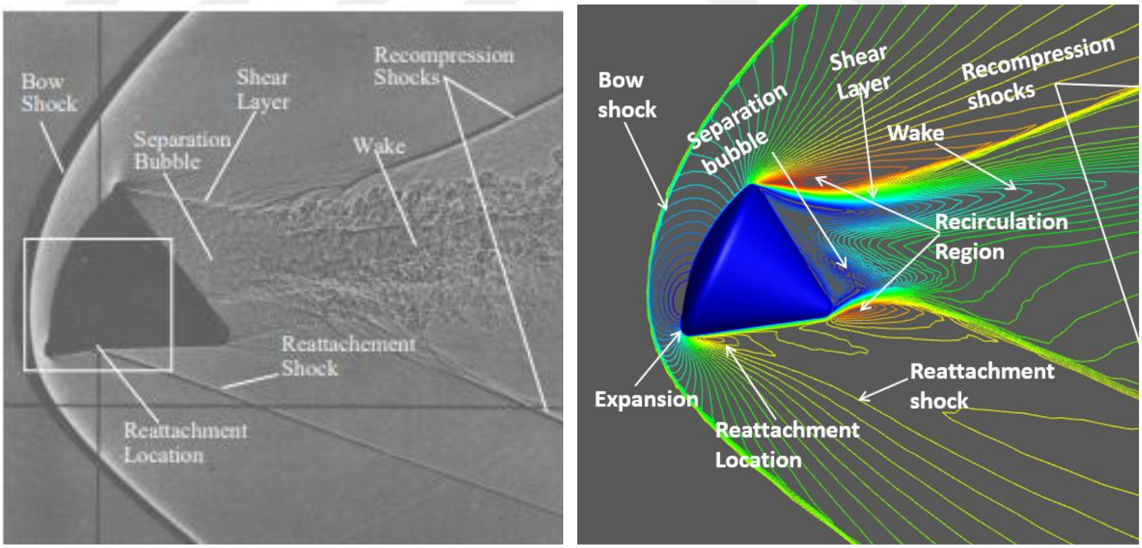

(a)

(b)

Figure 6.20 : Experimental shadowgraph (a) depicting salient features in the flow around an Apollo- shaped body at Mach 2.2 and angle of attack of 25 deg [57] vs the Mach contour (b) obtained using CFD at the same Mach 2.2 and angle of attack of 25 deg in the present thesis study.

Reentry flow field is typically characterized by circulating bubbles and a lot of vortices. At angle of attack that is non zero the bubbles are typically asymmetric and mostly observed in the leeward region of the reentry capsule. The separation occurs at the start of the capsule and the quickly reattached long the body. Figure 6.20 shows a typical flow field where the windward free shear layer can be seen to curve around and reattach on the conical frustum. A reattachment shock is generated at this location. The attached flow subsequently separates at the base. On the leeward side, the flow separates at the shoulder to form the large recirculation region. The comparison of these flow phenomenon is done between experimental shadowgraph Figure 6.21(a) and present study CFD simulation Figure 6.21(b) to demonstrate the accuracy of the simulation in predicting the nature of the known flow field.

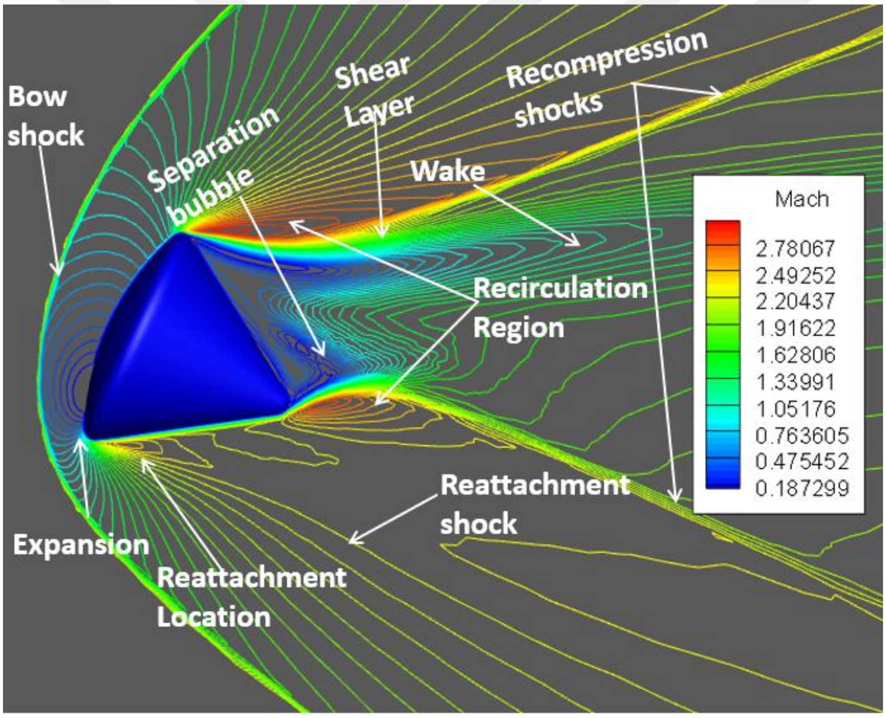

Figure 6.21 : Magnified Mach contour plot distribution depicting some salient features in the flow around an Apollo AS-202 reentry capsule.

The governing equation solved was turbulent Navier stokes equation with Roe flux splitting. The CFL equals one as the for are more robust simulation. Afterbody flow separation and reattachment is usually characterized with stagnation which comes with intensive local pressure and temperature and heat transfer. For these reasons the absolute magnitude and the exact location of the flow separation and reattachment is of importance for the afterbody heatshield and thermal protection design the magnified view of the typical flow field obtained in present study is shown in Figure 6.22. A study by [58] showed that there is a negligible difference in the flow field between reacting flow simulation and the non-reacting flow simulation. It is inferred that this may be due to flow expansion around the shoulder, which cools the gas and reduces vibrational excitation effects drastically. Thus, the effect of high-temperature phenomena on the flow field at the chosen freestream conditions is negligible.

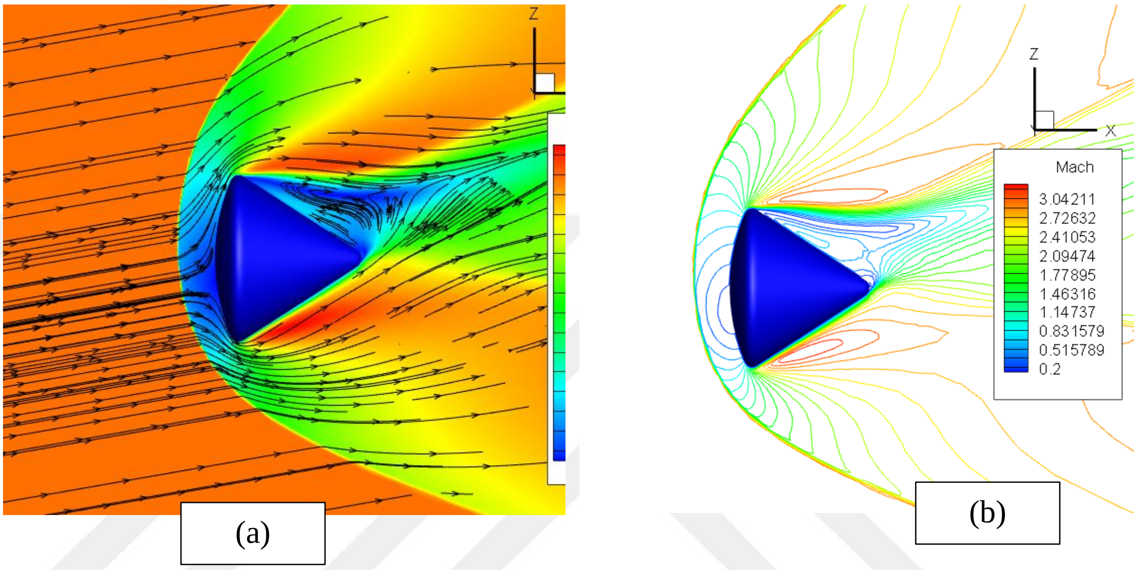

(a)

(b)

Figure 6.22 : The Streamlines (a) and Mach lines (b) distributions around Apollo AS-202 Reentry capsule at Mach = 2.98, Angle of flow = 10**º.**

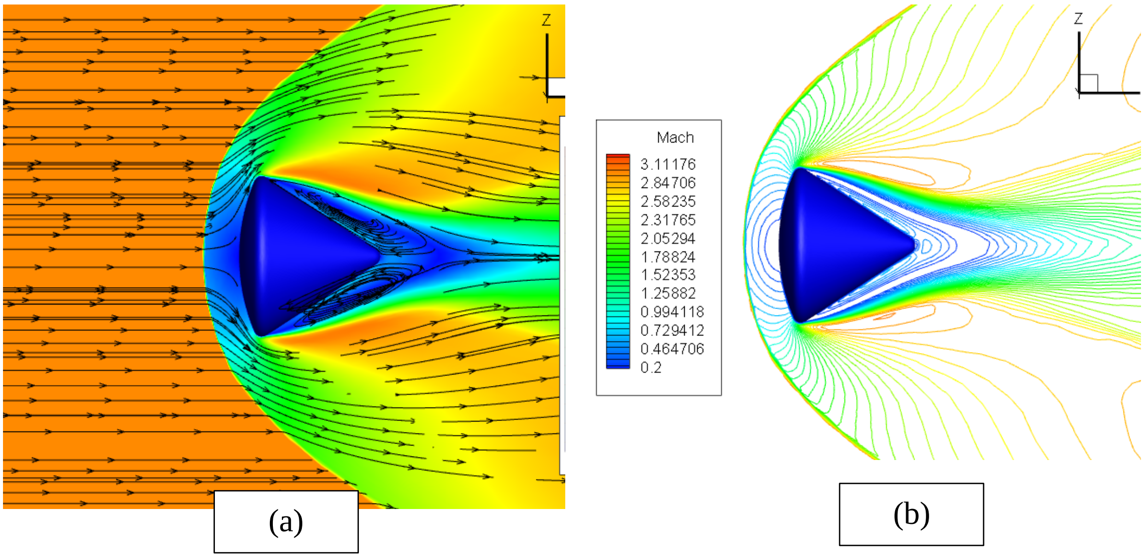

(a)

(b)

Figure 6.23 : The Streamlines (a) and Mach lines distributions (b) around Apollo AS-202 Reentry capsule at Mach = 2.98, Angle of flow = 0º.

The streamlines patterns are important to see the nature of the flow path around the capsule. Figure 6.22(a) shows the streamlines at 10º angle of attack and Figure 6.22(b) shows the Mach line distribution at the same conditions. In comparison, Figure 6.23 (a) shows the streamlines at 0^o angle of attack and the Figure 6.23(b) shows the corresponding Mach lines distribution at the same condition of Mach and Reynolds number. The effect of angle of attack on the nature of the flow field can be seen.

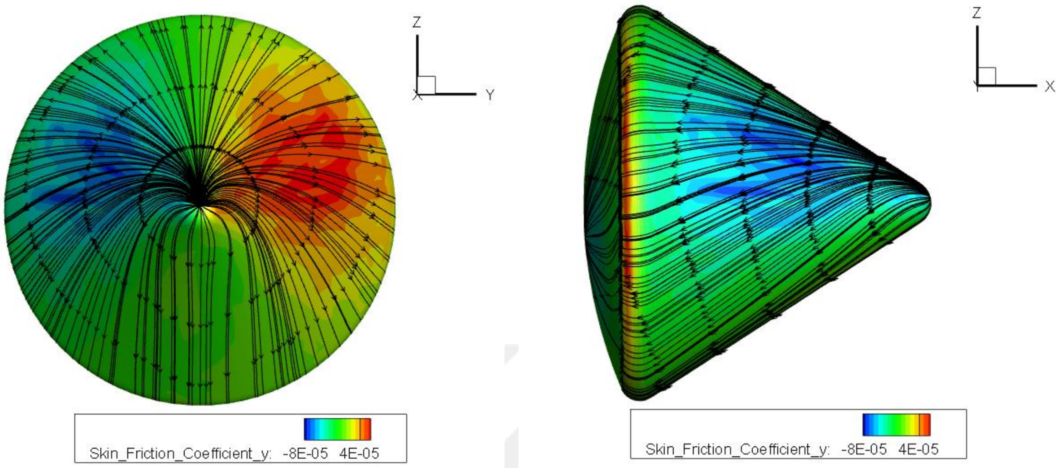

Figure 6.24 : The Streamlines distribution and surface skin friction around Apollo AS-202 Reentry capsule at Mach = 2.98, Angle of flow = -170^o.

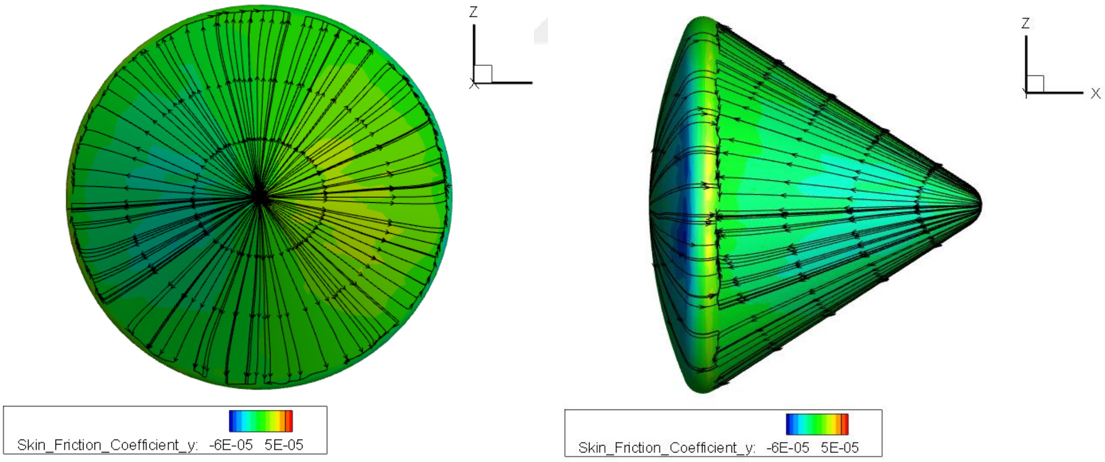

Figure 6.25 : The Streamlines distribution and surface skin friction around Apollo AS-202 Reentry capsule at Mach = 2.98, Angle of flow = 0^o.

The streamlines patterns are important to see the nature of the flow path around the capsule. Figure 6.24 shows the streamlines on the body of capsule at -170^o angle of attack. In comparison, Figure 6.25 shows the streamlines at 0^o angle of attack and the. The effect of angle of attack on the nature of the flow field can be seen.

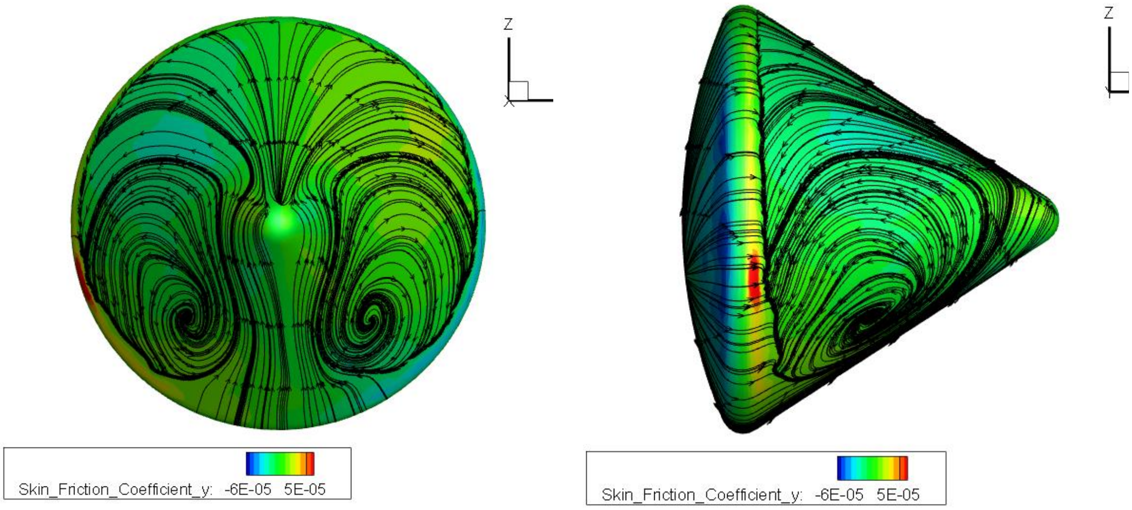

Figure 6.26 : The Streamlines distribution and surface skin friction around Apollo AS-202 Reentry capsule at Mach = 2.98, Angle of flow = 10^{o}**.**

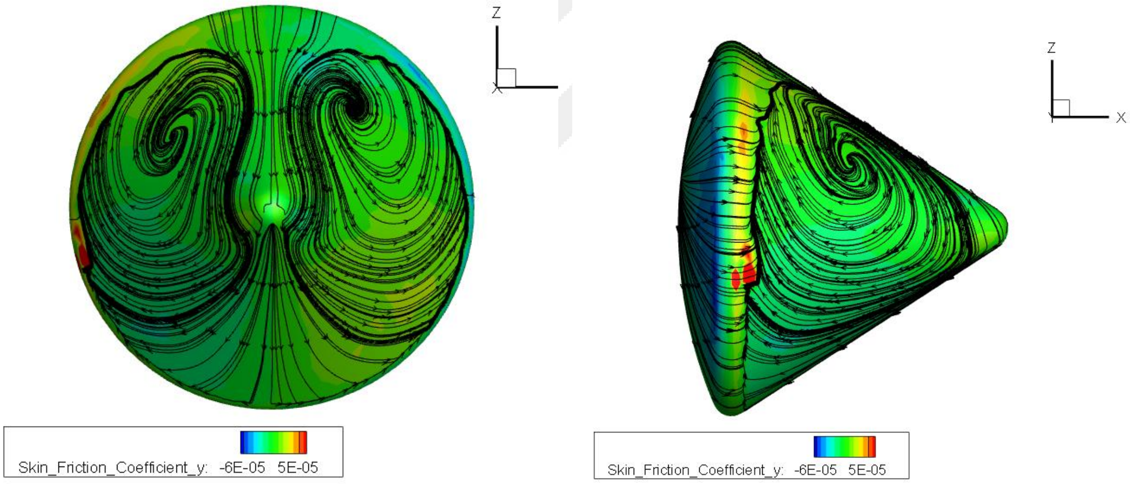

Figure 6.27 : The Streamlines distribution and surface skin friction around Apollo AS-202 Reentry capsule at Mach = 2.98, Angle of flow = -10^{0}.

The streamlines patterns are important to see the nature of the flow path around the capsule. Figure 6.26 shows the streamlines on the body of capsule at 10^{o} angle of attack. In comparison, Figure 6.27 shows the streamlines at -10^{o} angle of attack and the. The effect of angle of attack on the nature of the flow field can be seen.

6.9 Surface Pressure Validation

The final validation for the study of flow field around Apollo AS-202 reentry capsule is to compare in a pointwise manner, the normalized pressure along the nose upper half of the body in the pitch plane. Figure 6.28 shows the comparison of the normalized pressure obtained by solving the governing Navier stokes equation at Mach number of 10.18 and Reynold's number of 1.1 x 10^6. The angle of attack for the simulation is 0^o. The experimental data for the comparison was obtained from the Apollo wind tunnel experiment [59].

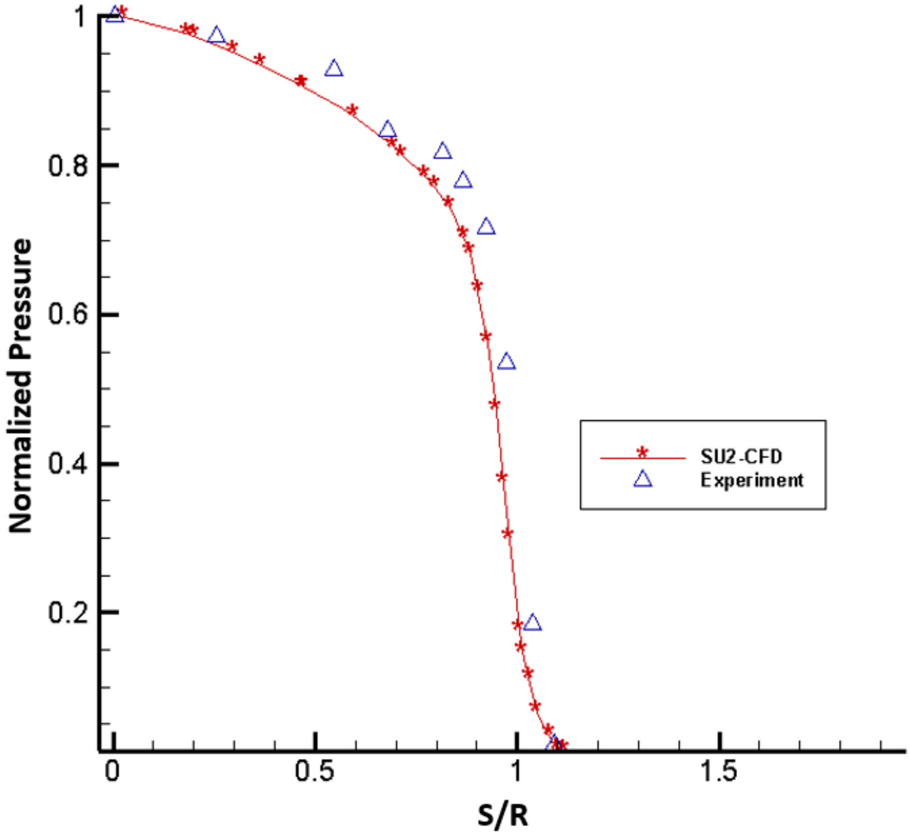

Figure 6.28 : Normalized pressure along upper half body nose of Apollo As-202 reentry capsule in present study vs experimental for Mach = 10.18.

The comparison in Figure 6.28 has shown a fair agreement between the computational results obtained using SU2 in present analysis and the experimental results from [59]. The *S* in the diagram represents the distance along surface from geometric center of spherical heat shield and *R* is maximum body radius of the capsule, 3.912m for full-scale command module.

6.10 Mesh Adaptation

Flow solutions were computed by solving Navier-Stokes’s equation with Spalart-allmaras turbulence model. For all the simulation described in this thesis, mesh adaptation is used to improve the accuracy in capturing some salient flow features which is important. The goal of this mesh adaptation is to accurately capture the shocks around the apollo reentry capsule, by creating anisotropic mesh elements along the shocks' directions of anisotropy. The sensor for the current study is the Mach number after a modification to the default setting. On solid wall, we use Mach 1 rather than zero. This high gradient leads the refinement of the boundary layer. Otherwise, we may lose boundary layer mesh where the Mach gradients are week such as separation points. The mesh adaptation software pyAMG is coupled with the CFD solver SU2 which allows the solution-based mesh adaptation. The sensor function for the adaptation is based on the Mach number. The minimum and maximum length of edge allowed were 1.0x10^{-8} and 100 units respectively. The record of the number of vertices and elements at each iteration level is given in table 6.1.

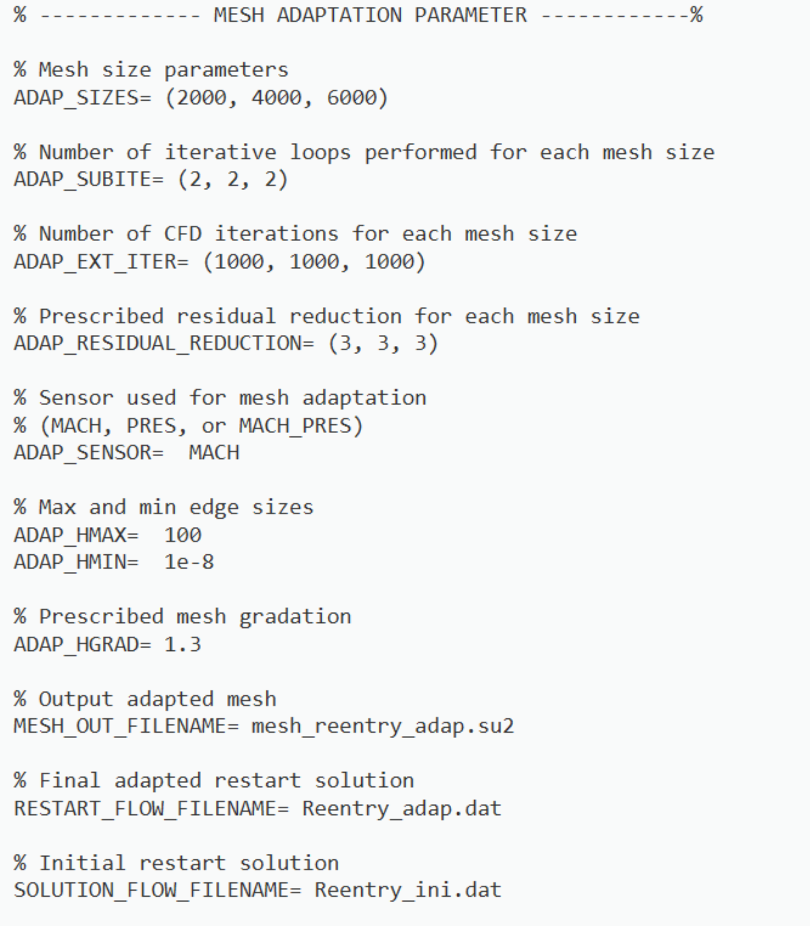

```
% ------------- MESH ADAPTATION PARAMETER ------------%

% Mesh size parameters
ADAP_SIZES= (2000, 4000, 6000)

% Number of iterative loops performed for each mesh size
ADAP_SUBITE= (2, 2, 2)

% Number of CFD iterations for each mesh size
ADAP_EXT_ITER= (1000, 1000, 1000)

% Prescribed residual reduction for each mesh size
ADAP_RESIDUAL_REDUCTION= (3, 3, 3)

% Sensor used for mesh adaptation
% (MACH, PRES, or MACH_PRES)
ADAP_SENSOR=  MACH

% Max and min edge sizes
ADAP_HMAX=  100
ADAP_HMIN=  1e-8

% Prescribed mesh gradation
ADAP_HGRAD= 1.3

% Output adapted mesh
MESH_OUT_FILENAME= mesh_reentry_adap.su2

% Final adapted restart solution
RESTART_FLOW_FILENAME= Reentry_adap.dat

% Initial restart solution
SOLUTION_FLOW_FILENAME= Reentry_ini.dat
```

Figure 6.29 : Configuration file for the mesh adaptation of pyAMG+SU2

Table 6.5 : Anisotropic mesh adaptation summary for flow Apollo reentry capsule.

Refinement Level	Number of vertices	Number of Elements	Number of surfaces elements
Mach = 2.98, AoA = 154			
Initial mesh	101,233	589,055	4,218
Iteration 1	209,213	682,542	4,866
Iteration 2	309,213	782,542	5,126
Iteration 3	511,758	951,333	6,243
Iteration 4	930,983	2,189,292	7,012
Iteration 5	1,301,845	3,199,430	8,185
Mach = 2.2, AoA = 25			
Initial mesh	102,233	519,055	4,318
Iteration 1	209,213	682,542	4,926
Iteration 2	309,213	782,542	5,326
Iteration 3	533,754	941,233	6,146
Iteration 4	930,983	2,301,362	7,431
Iteration 5	1,291,123	3,211,410	8,985
Mach = 8.0, AoA = 150			
Initial mesh	123,234	548,548	4,218
Iteration 1	217,242	672,842	5,066
Iteration 2	311,214	792,452	5,886
Iteration 3	527,658	952,237	6,244
Iteration 4	940,983	2,189,292	8,012
Iteration 5	1,301,845	3,517,420	9,005
Mach = 10.15, AoA = 155			
Initial mesh	101,233	589,055	4,218
Iteration 1	208214	672,531	4,723
Iteration 2	307,414	772,541	5,186
Iteration 3	508,758	951,333	6,243
Iteration 4	927,823	2,169,292	7,012
Iteration 5	1,311,845	3,192,430	8,881
Mach = 12 AoA = 160			
Initial mesh	101,233	589,055	4,218
Iteration 1	209,213	682,542	4,866
Iteration 2	309,213	782,542	5,126
Iteration 3	511,758	951,333	6,243
Iteration 4	930,983	2,189,292	7,012
Iteration 5	1,302,885	3,179,420	8,184

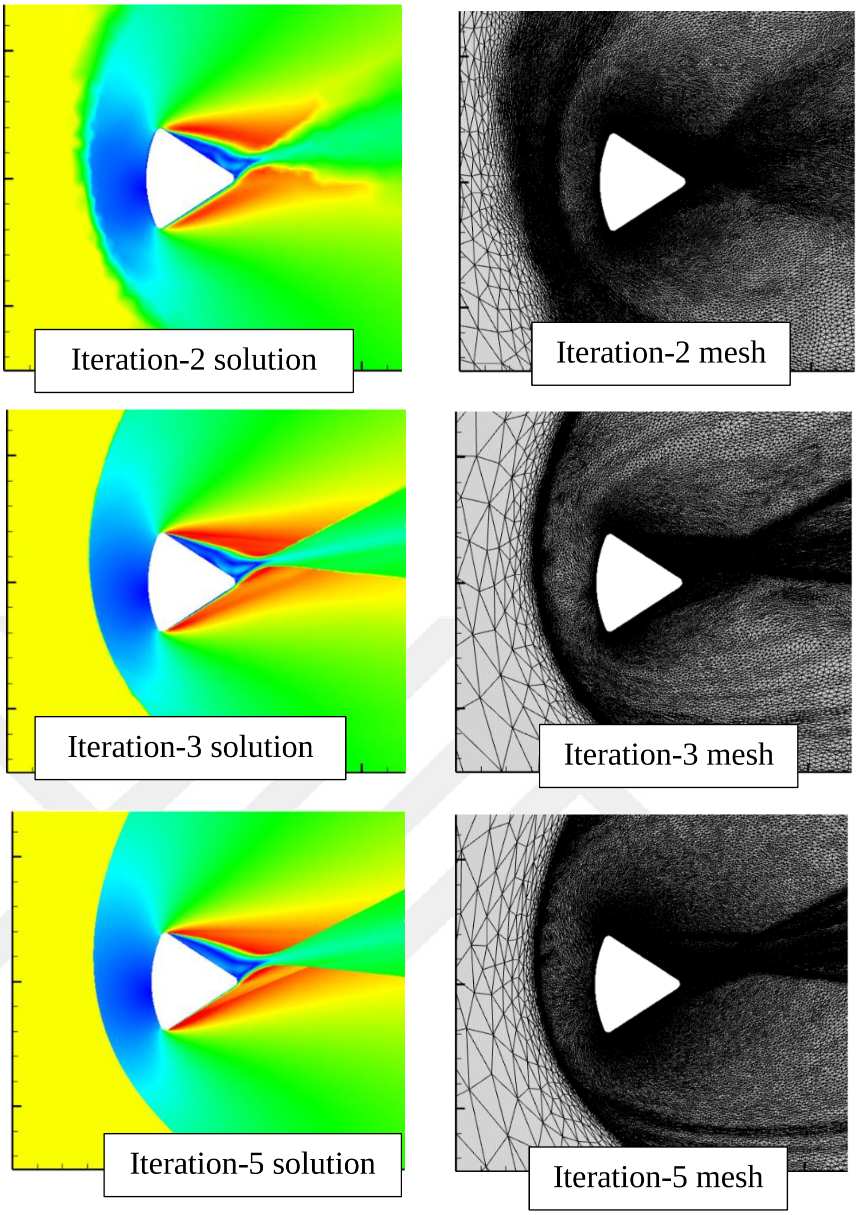

Figure 6.30: Solution and adapted meshes flow over Apollo-AS-202 reentry capsule.

Figure 6.31 shows each adapted mesh for the 10◦ angle of attack case. The symmetry plane Mach number contour distribution and the corresponding adapted mesh is shown. The mesh in the vicinity of the bow shock has been significantly enriched, especially in the direction normal to the shock. There is also significant adaptation downstream of the body, where flow does not appreciably affect the forces and moments on the body. The adapted mesh is much finer in the shoulder region, in order to resolve the expansion around the shoulder. Using the mesh adaptation has significantly improve the accuracy of the solutions.

6.11 Grid Convergence

The computed aerodynamics CD, CL, are shown in Figure 6.31 and Figure 6.32, plotted against $N^{-2/3}$ where N is the number of nodes in the mesh. This assumes that the characteristic length of the mesh, h, varies with the inverse of the cube root of the number of nodes, $h \approx N^{-1/3}$. The discretization scheme is also assumed to be second order, so that computed outputs vary linearly with h^2. The axis is such that the finest meshes are on the left side. The abrupt change in the force coefficient between the initial mesh and the first adapted mesh results from the dramatic change in the distribution of points between the initial and first adapted mesh.

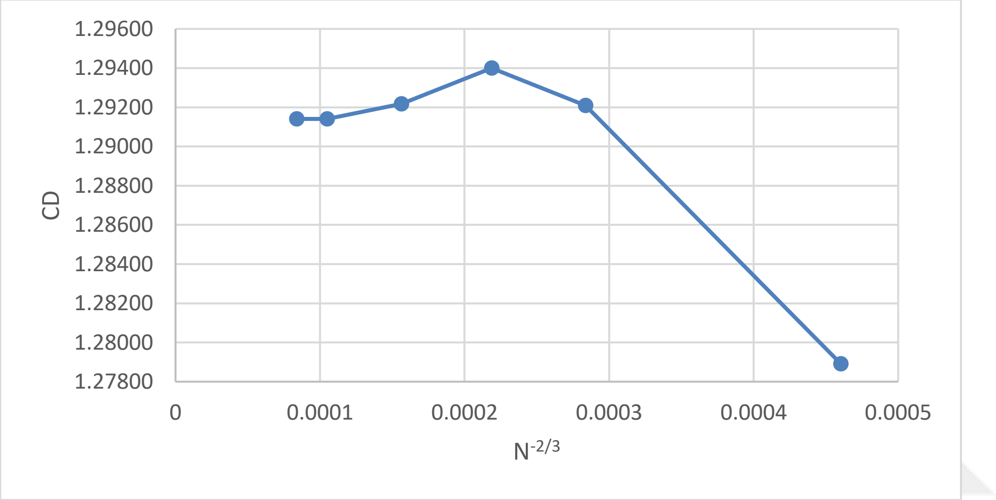

Figure 6.31: Grid convergence of drag coefficient flow over Apollo-AS-202 reentry capsule at Mach 2.98 and angle of attack 154.

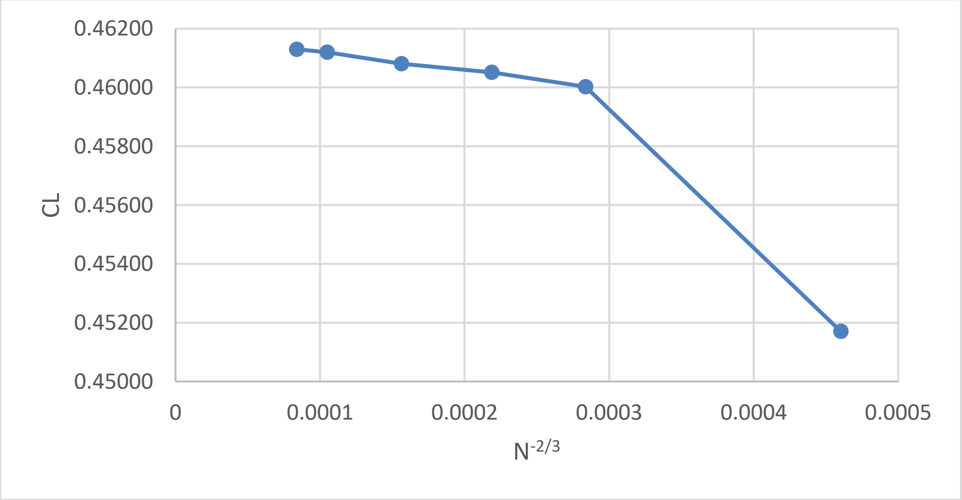

Figure 6.32: Grid convergence of lift coefficient flow over Apollo-AS-202 reentry capsule at Mach 2.98 and angle of attack 154.

7. CONCLUSION AND RECOMMENDATIONS

A detailed analysis of flow around Apollo AS-202 reentry capsule has been carried out using SU2 coupled with solution-based anisotropic mesh adaptation library (pyAMG). The governing equations were compressible Navier-Stokes equation with Spallart Allmaras (SA) one-equation turbulence model. The fluid model was assumed to be ideal gas, and the parameters of interest were the aerodynamic force coefficients, surface pressure and flow field characteristics. The comparison of the hypersonic flow over a cylinder has shown a good agreement between the present study using SU2 and other numerical methods like shock-fitting and CESE. The study has also shown a fairly good agreement of the aerodynamic coefficients of Apollo AS-202 Reentry capsule obtained using CFD in present study and the 1968 wind tunnel experiments. The shadowgraph comparison has demonstrated the ability of CFD to capture salient flow features in the flow around an Apollo- shaped body at Mach 2.2 and angle of attack of 25 deg as predicted from wind tunnel experiments and the normalized surface pressure comparison has agreed with the experimental data as well. Using the anisotropic mesh adaptation has significantly improve the accuracy of the solutions. For future analysis, thermal non-equilibrium, chemical reactions and aerothermodynamics analysis need to be taken into account (SU2-NEMO) to fully understand the effect of these flow properties in the accuracy of the solution.

REFERENCES

[1] **S. Rathnavel, K. Balaji, K. V. Sankaran, and N. S. Raja,** “Investigation of computational Flow field and Aerothermodynamics over a Re-entry crew module using SU2,” p. 3.

[2] **D. R. N. Mathews,** “Hypersonic Flow Analysis on An Atmospheric Re-Entry Module,” vol. 3, no. 5, p. 11, 2015.

[3] **J. Muylaert *et al.*,** “Aerothermodynamic Analysis of Space- Vehicle Phenomena,” p. 11, 2001.

[4] **B. J. Griffith and D. E. Boylan**, “Postflight Apollo command module aerodynamic simulation tests.,” *Journal of Spacecraft and Rockets*, vol. 5, no. 7, pp. 843–848, 1968.

[5] **K. Sinha and S. Reddy,** “Hypersonic Turbulent Reacting Flow Simulation of Fire II Re-entry Vehicle,” in *45th AIAA aerospace sciences meeting and exhibit*, 2007, p. 805.

[6] **J. D. Anderson,** “Fundamentals of Aerodynamics,” p. 1131, 2009.

[7] **Huaibao Zhang,** “High Temperature Flow Solver for Aerothermodynamics Problems.,” Phd Thesis, University of Kentucky, 2015.

[8] **J. R. Finkbeiner, P. H. Dunlap, B. M. Steinetz, and C. C. Daniels,** “Review of Seal Designs on the Apollo Spacecraft,” *Journal of Spacecraft and Rockets*, vol. 45, no. 5, pp. 900–910, Sep. 2008, doi: 10.2514/1.27188.

[9] “**NASA – Spacecraft Design**". Archived from the original on July 9, 2009. Retrieved January 7, 2013”.

[10] **Anderson, J. D.***:* Hypersonic and High Temperature Gas Dynamics, 2nd ed. American Institute of Aeronautics and Astronautics, Reston, Virginia, 2006.

[11] **Jenkins, Dennis R.** (2007). Space Shuttle: The History of the National Space Transportation System. Voyageur Press. p. 524 pages. ISBN 0-9633974-5-1.”.

[12] **Allen, H. Julian, and Eggers, Alfred J., Jr.** ‘A Study of the Motion and Aerodynamic Heating of Ballistic Missiles Entering the Earth’s Atmosphere at High Supersonic Speeds.’ NACA Technical Report 1381, Forty-Fourth Annual Report of the NACA—1958. Washington, D.C.: 1959, 1125-1140.”

[13] **G. Chapline *et al.*,** “Thermal Protection Systems,” p. 18.

[14] **T. D. Economon, F. Palacios, S. R. Copeland, T. W. Lukaczyk, and J. J. Alonso,** “SU2: An Open-Source Suite for Multiphysics Simulation and Design,” *AIAA Journal*, vol. 54, no. 3, pp. 828–846, Mar. 2016, doi: 10.2514/1.J053813.

[15] **T. D. Economon *et al.*,** “Performance optimizations for scalable implicit RANS calculations with SU2,” *Computers & Fluids*, vol. 129, pp. 146–158, Apr. 2016, doi: 10.1016/j.compfluid.2016.02.003.

[16] **D. J. Mavriplis,** “Unstructured Grid Techniques,” *Annual Review of Fluid Mechanics*, vol. 29, no. 1, pp. 473–514, 1997, doi: 10.1146/annurev.fluid.29.1.473.

[17] **P. L. Roe,** “Approximate Riemann solvers, parameter vectors, and difference schemes,” *Journal of computational physics*, vol. 43, no. 2, pp. 357–372, 1981.

[18] **M.-S. Liou and C. J. Steffen Jr,** “A new flux splitting scheme,” *Journal of Computational physics*, vol. 107, no. 1, pp. 23–39, 1993.

[19] **B. Van Leer**, “Towards the ultimate conservative difference scheme. V. A second-order sequel to Godunov’s method,” *Journal of computational Physics*, vol. 32, no. 1, pp. 101–136, 1979.

[20] **V. Venkatakrishnan,** “On the accuracy of limiters and convergence to steady state solutions,” in *31st Aerospace Sciences Meeting*, 1993, p. 880.

[21] **J. Blazek,** *Computational fluid dynamics: principles and applications*. Butterworth-Heinemann, 2015.

[22] **Y. Saad and M. H. Schultz,** “GMRES: A generalized minimal residual algorithm for solving nonsymmetric linear systems,” *SIAM Journal on scientific and statistical computing*, vol. 7, no. 3, pp. 856–869, 1986.

[23] **E. Molina *et al.*,** “Hybrid rans/les calculations in su2,” in *23rd AIAA computational fluid dynamics conference*, 2017, p. 4284.

[24] **M. Rouxel-labbe,** “Anisotropic mesh generation G ´ en ´ eration de Maillages Anisotropes,” 2017.

[25] **A. Loseille,** “Metric-orthogonal Anisotropic Mesh Generation,” *Procedia Engineering*, vol. 82, pp. 403–415, 2014, doi: 10.1016/j.proeng.2014.10.400.

[26] **P. Cavallo and T. Baker,** “Efficient Delaunay-based solution adaptation for three-dimensional unstructured meshes,” in *38th Aerospace Sciences Meeting and Exhibit*, 2000, p. 809.

[27] **S. Z. Pirzadeh,** “A solution-adaptive unstructured grid method by grid subdivision and local remeshing,” *Journal of aircraft*, vol. 37, no. 5, pp. 818–824, 2000.

[28] **T. Michal and J. Krakos,** “Anisotropic Mesh Adaptation Through Edge Primitive Operations,” presented at the 50th AIAA Aerospace Sciences Meeting including the New Horizons Forum and Aerospace Exposition, Nashville, Tennessee, Jan. 2012. doi: 10.2514/6.2012-159.

[29] **S. Owen,** “A survey of unstructured mesh generation technology,” *7th International Meshing Roundtable*, no. October, p. 25, 1998, doi: 10.1.1.34.5079.

[30] **A. Bowyer,** “Computing dirichlet tessellations,” *The computer journal*, vol. 24, no. 2, pp. 162–166, 1981.

[31] **F. P. Preparata and M. I. Shamos,** *Computational geometry: an introduction*. Springer Science & Business Media, 2012.

[32] **T. J. Baker,** “Automatic mesh generation for complex three-dimensional regions using a constrained Delaunay triangulation,” *Engineering with Computers*, vol. 5, no. 3–4, pp. 161–175, 1989.

[33] **N. P. Weatherill and O. Hassan,** “Efficient three-dimensional Delaunay triangulation with automatic point creation and imposed boundary constraints,” *International Journal for Numerical Methods in Engineering*, vol. 37, no. 12, pp. 2005–2039, 1994.

[34] **D. F. Watson,** “Computing the n-dimensional Delaunay tessellation with application to Voronoi polytopes,” *The computer journal*, vol. 24, no. 2, pp. 167–172, 1981.

[35] **C. L. Lawson,** “Software for C1 surface interpolation,” in *Mathematical software*, Elsevier, 1977, pp. 161–194.

[36] **R. Lohner, P. Parikh, and C. Gumbert,** “Interactive generation of unstructured grids for three dimensional problems,” 1988.

[37] **R. Löhner,** “Progress in grid generation via the advancing front technique,” *Engineering with computers*, vol. 12, no. 3–4, pp. 186–210, 1996.

[38] **S. H. Lo,** “Volume discretization into tetrahedra—I. Verification and orientation of boundary surfaces,” *Computers & structures*, vol. 39, no. 5, pp. 493–500, 1991.

[39] **S. H. Lo,** “Volume discretization into tetrahedra—II. 3D triangulation by advancing front approach,” *Computers & Structures*, vol. 39, no. 5, pp. 501–511, 1991.

[40] **M. S. Shephard and M. K. Georges,** “Automatic three-dimensional mesh generation by the finite octree technique,” *International Journal for Numerical methods in engineering*, vol. 32, no. 4, pp. 709–749, 1991.

[41] **M. A. Yerry and M. S. Shephard,** “Automatic three-dimensional mesh generation by the modified-octree technique,” *International Journal for Numerical Methods in Engineering*, vol. 20, no. 11, pp. 1965–1990, 1984.

[42] **M. J. Castro-Díaz, F. Hecht, B. Mohammadi, and O. Pironneau,** “Anisotropic unstructured mesh adaption for flow simulations,” *International Journal for Numerical Methods in Fluids*, vol. 25, no. 4, pp. 475–491, 1997.

[43] **P. Frey,** “Yams a fully automatic adaptive isotropic surface remeshing procedure,” 2001.

[44] **F. Hecht,** “BAMG: bidimensional anisotropic mesh generator,” *User Guide. INRIA, Rocquencourt*, vol. 17, 1998.

[45] **F. Alauzet and A. Loseille,** “A decade of progress on anisotropic mesh adaptation for computational fluid dynamics,” *Computer-Aided Design*, vol. 72, pp. 13–39, Mar. 2016, doi: 10.1016/j.cad.2015.09.005.

[46] **P. Gnoffo and J. White,** “Computational aerothermodynamic simulation issues on unstructured grids,” in *37th AIAA Thermophysics Conference*, 2004, p. 2371.

[47] **C.-L. Chang,** "Time-accurate, unstructured-mesh Navier-Stokes computations with the space-time CESE method," 2006.

[48] **Y. Chauvat, J.-M. Moschetta, and J. Gressier,** "Shock wave numerical structure and the carbuncle phenomenon," *International Journal for Numerical Methods in Fluids*, vol. 47, no. 8–9, pp. 903–909, 2005.

[49] **C.-L. Chang,** "Three-Dimensional Navier-Stokes Calculations Using the Modified Space-Time CESE Method," presented at the 43rd AIAA/ASME/SAE/ASEE Joint Propulsion Conference & Exhibit, Cincinnati, OH, Jul. 2007. doi: 10.2514/6.2007-5818.

[50] **M. D. Salas and H. L. Atkins,** "On problems associated with grid convergence of functionals," *Computers & fluids*, vol. 38, no. 7, pp. 1445–1454, 2009.

[51] **E. R. Hillje,** *Entry Flight Aerodynamics from Apollo Mission AS-202*. National Aeronautics and Space Administration, 1967.

[52] **G. F. Hollozuay and J. S. Ceuter,** "Apollo Experience Report - Guidance A N D Control Systems:," p. 60.

[53] **D. B. B. Lee,** "Heat-transfer rate and pressure measurements obtained during Apollo orbital entries," Oct. 1970. Accessed: Jul. 06, 2020. [Online]. Available: https://ntrs.nasa.gov/search.jsp?R=19700031842

[54] **M. J. Wright, D. K. Prabhu, and E. R. Martinez,** "Analysis of Apollo Command Module Afterbody Heating Part I: AS-202," *Journal of Thermophysics and Heat Transfer*, vol. 20, no. 1, pp. 16–30, Jan. 2006, doi: 10.2514/1.15873.

[55] **M. J. Wright, J. L. Brown, K. Sinha, G. V. Candler, F. S. Milos, and D. K. Prabhu,** "Validation of Afterbody Aeroheating Predictions for Planetary Probes: Status and Future Work," p. 12.

[56] **R. S. Crowder and J. D. Moote,** "Apollo entry aerodynamics.," *Journal of Spacecraft and Rockets*, vol. 6, no. 3, pp. 302–307, 1969.

[57] **R. L. Kruse,** "Transition and flow reattachment behind an Apollo-like body at Mach numbers to 9," 1968.

[58] **K. Sinha and A. Dey**, "Simulation of flow separation and reattachment on a re-entry capsule afterbody frustum," in *48th AIAA aerospace sciences meeting including the new horizons forum and aerospace exposition*, 2010, p. 1561.

[59] **J. J. Bertin,** The Effect Of Protuberances, Cavities, And Angle Of Attack On The Wind-Tunnel Pressure And Heat-Transfer Distribution For The Apollo Command Module. National Aeronautics and Space Administration, 1966.

CURRICULUM VITAE

Name Surname : Badamasi BABAJI

Place and Date of Birth :

E-Mail :

EDUCATION :

- **B.Sc.** :